FLORIDA INTERNATIONAL UNIVERSITY

Miami, Florida

THE CORROSION INHIBITION BEHAVIOR OF THERMALLY AGED CHROMATE

CONVERSION COATING APPLIED TO AEROSPACE ALUMINUM 2219

A dissertation submitted in partial fulfillment of

the requirements for the degree of

DOCTOR OF PHILOSOPHY

in

MATERIAL SCIENCE AND ENGINEERING

by

Michelle Stephane Pierre

2021

TO: Dean John L. Volakis
      College of Engineering and Computing

This dissertation, written by Michelle Stephane Pierre, and entitled The Corrosion Inhibition Behavior of Thermally Aged Chromate Conversion Coating Applied to Aerospace Aluminum 2219, having been approved in respect to style and intellectual content, is referred to you for judgment.

We have read this dissertation and recommend that it be approved.

_____
Benjamin Boesl

_____
Kingsley Lau

_____
Chengxian Lin

_____
Eliza Montgomery

_____
Shekhar Bhansali, Co-Major Professor

_____
Norman Munroe, Co-Major Professor

Date of Defense: November 12, 2021

The dissertation of Michelle Stephane Pierre is approved.

_____
Dean John L. Volakis
College of Engineering and Computing

_____
Andrés G. Gil
Vice President for Research and Economic Development
and Dean of the University Graduate School

Florida International University, 2021

DEDICATION

All that I am, or ever hope to be, I owe to the sacrifices of my angel mother.

In loving memory of Camille Jean Mary

Je t'aime

Merci Bon Dieu je suis libre

ACKNOWLEDGMENTS

course a special thank you to our Mrs. Patricia "Pat" Brammer who had keys to all locked doors.

A special thank you to my family. There are no words that can be stringed together to express how grateful I am to you: my sisters, Luce Pierre and Stacey Bien-Aime, my nieces, Star Camille and Skye Pierre. When I was homeless you sheltered me, when my daughters were in need you fed them and took them in. When I was much too proud to ask, you outpoured your support to us both financially and emotionally. All I can say is <u>it did take a village. Merci.</u>

To my lovely daughters (Priscilla & Ava), though I missed milestones that I can never hope to get back, I pray this journey gave you hope. We created our own world-wind micro-environment and solidified our bonds. I thank you for the endless laughter, hugs, kisses, and most of all the chance to be your mother.

ABSTRACT OF THE DISSERTATION

THE CORROSION INHIBITION BEHAVIOR OF THERMALLY AGED CHROMATE

CONVERSION COATING APPLIED TO AEROSPACE ALUMINUM 2219

by

Michelle Stephane Pierre

Florida International University, 2021

Miami, Florida

Professor Norman Munroe, Co-Major Professor

Professor Shekhar Bhansali, Co-Major Professor

NASA Kennedy Space Center's technical standard for corrosion protection of space flight hardware provides guidance concerning temperature restrictions and exposure limits for processing unpainted chromate conversion coatings (CCC) for the Orion crew space vehicle as part of the Artemis program. The standard requires that all CCC treated flight hardware components be fully coated within seven days with a maximum storage time of seven days at ambient temperatures (much less time at higher temperatures). Currently, there is no literature nor qualified industry testing supporting the exposure limits set by the standard. The standard is quite restrictive to processing flight components. In some cases, a conversion coating will be used without an additional coating to provide more limited corrosion protection while the flight hardware undergoes many different, but controlled, processes that are time consuming. The protective coatings need to maintain their integrity throughout processing, so understanding the corrosion mechanisms associated with the materials and corrosion control limitations is vital for the health of the spacecraft. In this

study, CCC was applied to aerospace grade Aluminum 2219 samples that were aged for three months and then subsequently heat treated at 65°C and 129°C. This research focused on using surface-based characterization techniques to evaluate the corrosion resistance of the thermally aged CCC treated Al2219 panels via electrochemical analysis and exposure to standard salt-fog corrosion testing. Electrochemical studies monitored coating degradation with age at ambient laboratory conditions and at elevated temperatures. Surface chemistry techniques, XPS and SEM/EDS, were used to monitor progression of dehydration as samples aged and heat treated. The extent of pit density of the samples were evaluated based on age and heat treatment using three-dimensional optical profilometry. This study clarified some uncertainties regarding temperature and storage of CCC treated Al2219. Samples that were CCC treated and stored at ambient temperatures and samples that were heat treated to 65°C provided similar corrosion protection of Al2219 up to three months. The coatings that were heat treated to 129°C performed poorly despite age. It was evident that these samples underwent a gradual progression dehydration and loss of chromium hydroxides which provides a barrier of protection to the substrate.

TABLE OF CONTENTS

LIST OF TABLES

LIST OF FIGURES

xvii

LIST OF ACRONYMS

AFM	Atomic Force Microscopy
Al	Aluminum
ASTM	American Standards for Testing of Materials
C	Carbon
CCC	Chromate Conversion Coating
CE	counter electrode
Cl	Chlorine
CPC	Corrosion Preventative Compound
Cr	Chromium
Cu	Copper
EDS	Energy Dispersive X-ray Spectroscopy
EIS	electrochemical impedance spectroscopy
Fe	Iron
FTIR	Fourier transform infrared spectroscopy
ISO	International Organization for Standardization
LES	Launch Experiment Shop
mpy	mills per year --
Ni	Nickel
O	Oxygen
OP	optical profilometry

RE   reference electrode

SCE   saturated calomel electrode

SEM   Scanning Electron Microscopy

Ta   Tantalum

Ti   Titanium

WE   working electrode

XPS   X-ray Photoelectron Spectroscopy analysis

XPS   X-ray Photoelectron Spectroscopy

XRD   X-ray Diffractometry

LIST OF SYMBOLS AND ABBREVIATIONS

Symbol	DEFINITION	SI Units
T	Temperature	°C
θ_c	receding contact angle	degrees or °
θ_a	advancing contact angle	degrees or °
γ_{lv}	surface tension of water	mN/m
b_a	anodic Tafel slope	
b_c	cathodic Tafel slope	
C	capacitance of electrical circuit	$Ohms^{-1}$
C_{dl}	double layer capacitance	$Ohms^{-1}$
E	potential	mV
E_{CORR}	corrosion potential	Volts (V)
E_{OC}	open circuit potential	Volts (V)
F	force	mN or N
I	current	Amps (A)
I_{CORR}	corrosion current	Amps (A)
i	current density	$Amps/cm^2$ (A/cm^2)
i_{CORR}	corrosion current density	$Amps/cm^2$ (A/cm^2)
i_{PASS}	Passive current density	$Amps/cm^2$ (A/cm^2)
R	resistance of electrical circuit	Ohms
R_P	polarization resistance	$Ohms\ cm^2$
V	voltage	Volts (V)

CHAPTER 1

1.0 Introduction

For metallic alloys used in aerospace applications, it is important to use lightweight and durable materials to support the longevity of flight hardware. Advanced aluminum alloys have been favorable among the aerospace industry because of their high strength and high ductility in progressive heat treatments (1). More specifically, the aluminum alloy 2219-T87 has been widely used in aerospace applications because of its superior mechanical properties including strength-to-weight ratio, which result from the alloying elements such as copper, magnesium, and manganese. Aluminum alloy 2219-T87 is known for its characteristics of strength, fracture toughness, and resistance to stress corrosion cracking, which is attractive to aircraft producers (2). Aluminum alloys have a history of use for spacecraft and are currently being used on crew modules for the Artemis Program, known as Orion (Figure 1), and in commercial space applications.

Figure 1. Orion crew module for the Artemis I mission at NASA KSC (3).

Aluminum alloys are the major manufacturing material of structures and components in both the aircraft (military and commercial) and space flight arena due to its high specific strength and low densities. Aluminum has a wide passive state between pH range 4-9 that allows a thin oxide film to form across the surface and adheres bon strongly to the surface (4). This oxide layer is known to reform when damaged in most environments which gives it good corrosion resistant properties. Unfortunately, NASA Kennedy Space Center's (KSC) unique aggressive launch environment induces corrosion of this alloy. NASA KSC's launch site is a very humid, marine environment that is less than a mile from the Atlantic Ocean (5). Due to the high humidity and high salt environment, the 2XXX series aluminum alloy becomes susceptible to localized corrosion, such as pitting and crevice corrosion. This makes lengthy storage and processing times of flight hardware challenging. Consequently, the processing and maintenance of this material against degradation and corrosion is of prime importance to NASA in preserving space operations capabilities for space flight hardware.

Aluminum alloy 2219 is the most widely used aluminum alloy for structural components of manned flight vehicles. It has optimal mechanical strength, fracture toughness, resistance to general corrosion and stress corrosion cracking, it is also commercially available in many forms. Generally, corrosion resistance of Al2219 is improved through a solid solution treatment at a high temperature in order to incorporate and dissolve the more noble copper into aluminum. The copper element provides this alloy with its preferred mechanical strength. While rapid cooling is used to prevent the formation of large Al_2Cu

inclusions at the grain boundaries, this feature is quite common to this alloy. However, an excessive formation of this inclusion causes the surrounding aluminum matrix with copper depletion to be susceptible to corrosion attack. Al2219 is known to have poor corrosion resistance to marine environments such as what is found at NASA KSC (6).

In order to protect flight hardware, these alloys require additional protection during storage and processing which is usually completed through a chromate conversion coating process. Chromate conversion coating is a known thin film coating used to protect aluminum from corrosion and is well regarded as a pretreatment to enhance paint adhesion. Chromate conversion coating, chromium (VI) base treatment, is widely used to protect Al2219 hardware. According to NASA standard requirement for Corrosion Protection for Space Flight Hardware, NASA-STD-6012A (7):

> "Per MIL-DTL-5541F, paragraph 6.14: "Unpainted conversion coatings will commence losing corrosion resistance properties if exposed to temperatures of 60°C (140°F) or higher, during drying, subsequent fabrication, or service. As temperatures and exposure times increase, the corrosion protection of unpainted conversion coated parts decreases. The reduction is believed to result from the coating dehydrating and the resulting insolubility of the chromates within the coating."
>
> Chromate conversion coatings are partially hydrated coatings which will undergo dehydration. The 140°F limit should also be subject to an exposure time limit. Currently, there is no literature supporting exposure time limits. Guidance concerning elevated temperature exposure limits for unpainted conversion coatings is as follows:
>
> 1 minute at 60°C (140°F)
> 4 minutes at 54°C (130°F)
> 15 minutes at 49°C (120°F)
> 1 hour at 43°C (110°F)
> 3 hours at 38°C (100°F)
> 12 hours at 32°C (90°F
> 48 hours at 27°C (80°F)

168 hours at 21ºC (70°F)
Dewpoints also affect elevated temperature exposure time. Consider an example where conditions are very dry (low dew point) and/or the atmospheric pressure is low (relative to the vapor pressure of water). It might only take a few minutes in the 60-65ºC (140-150°F) range to render the coating useless. In high dewpoint situations, the coating might be able to tolerate an hour or more at 71ºC (160°F) and several minutes at 82ºC (180°F)."

NASA KSC's current requirement for chromate conversion coating is extremely limiting and is not based on the coating's performance in the end use service environment of the flight hardware. The standard requires that any and all unpainted conversion coated fight hardware not be used if being stored longer than seven days at ambient temperatures. This time frame becomes much less at higher temperatures and dewpoints. The processing of flight hardware can be a very lengthy process and require coating curing times and temperatures that far exceeds the limitation set forth in the standard. The guidance from the standard is used and implemented with no literature support or actual test data to support these limits. As NASA continue the route of reuse of flight hardware of the Orion crew vehicle for the new Artemis program, it is important to understand how aging, humidity, and processing temperatures effect the corrosion resistance of chromate conversion coating on aerospace alloy Al2219-T87. This will require taking this real-world problem and understanding the fundamental coating formation process of the chromate conversion coating in terms of corrosion inhibition and qualifying the CCC treated hardware using applied testing in an aggressive service environment (Figure 2).
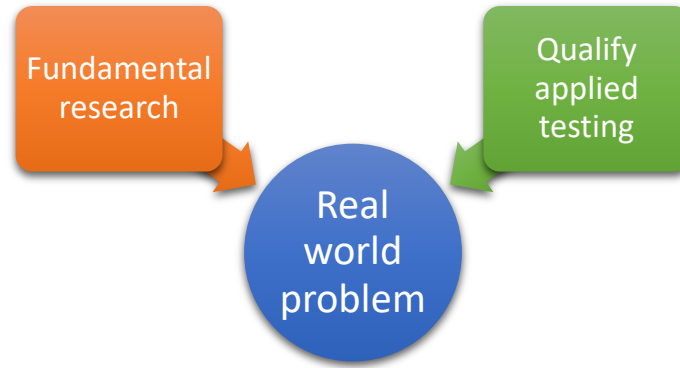
Figure 2: Overall research approach

1.1 Research Objectives:

The aim of this research is to evaluate the coating formation and degradation on Al2219-T87 aluminum alloy. This investigation focused on the effects of corrosion protection as a function of elevated temperatures and storage times. Because uncertainties exist in the understanding of the use of chromate conversion coating at KSC's unique marine environment, the chromate conversion coating was characterized before and after application to the Al2219 substrate and its ability to provide corrosion protection in a high humid and high salt environment. This research sought to provide answers and direction to the following research questions:

RO1. How do the surface characteristics of chromated conversion coating on Al2219 change with elevated temperatures and storage time in ambient and corrosive environments?

RO2. Will the processing temperatures for space flight hardware cause mud-cracking and/or coating degradation in chromated conversion coating on Al2219?

RO3.	What is the maximum applied temperature and exposure time boundaries for flight component boundaries that will lead to coating degradation in chromated conversion coating of Al2219?

RO4.	What is the effectiveness of the chromated conversion coating of Al2219 in mitigating corrosion when exposed to a corrosive environment?

In order to provide a real-world solution to the research objectives, fundamental research was used in combination with current industry qualification testing (Figure 3). The research strategy was separated into two major categories: evaluation of the non-coated Al2219 substrate in tandem with the chromate conversion coated (CCC) Al2219 substrate. Fundamental surface characterization in combination with industry accelerated corrosion testing as a function of temperature and storage were performed. Figure 2 describes the overall research strategy taken in this research and Figure 3 summarized the testing strategy.
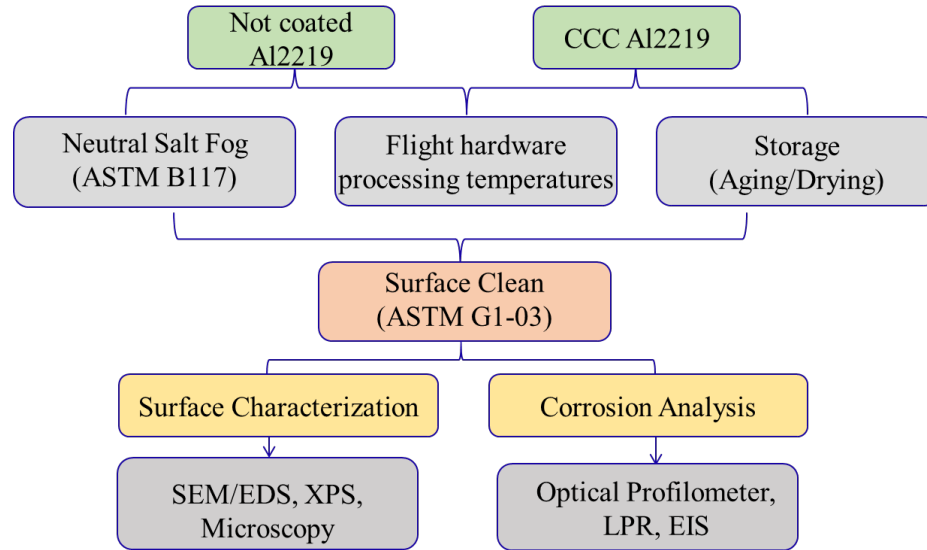
Figure 3: Research strategy used to combine fundamental research with applied testing.

1.2   Dissertation structure

This dissertation consists of 6 chapters.

- Chapter 1, current chapter, provides a brief description of the background and research objective of this thesis.

- Chapter 2 provides a literature review of previous studies on chromate conversion coatings and aerospace aluminum alloys. The current understanding of the coating morphology and structure are reviewed and presented. While development of chromate free coatings is being explored extensively in the field, it is not the topic of this research.

- Chapter 3 describes the surface analysis techniques used in this research to understand the fundamental surface characterization of chromate conversion coating on Al2219.

- Chapter 4 examines the chromate conversion coating formation and degradation as a function of heat treatment, aging, and accelerated corrosion exposure. The results from this study clarified dehydration of the coating and service temperature conditions.

- Chapter 5 summarizes the results from chapters 3-4 and the research objective questions are answered. A better understanding on the coating formation and corrosion inhibition mechanisms is obtained. Some suggestions are provided for the future study of chromate coatings and the development of chromate-free coating systems.

- Chapter 6 concludes the data and links these conclusions back to the research objectives set forth in Chapter 1 and possible forward word from this research are listed.

CHAPTER 2

2.0   Literature Review

2.1   Aluminum Alloy

For metallic alloys used in aerospace applications, it is important to use lightweight and durable materials to support the longevity of flight hardware. Advanced aluminum alloys have been favorable among the aerospace industry because of their high strength and high ductility in progressive heat treatments (1). More specifically, the aluminum alloy 2219-T87 has been widely used in aerospace applications because of its superior mechanical properties including strength-to-weight ratio, which result from the alloying elements such as copper, magnesium, and manganese. Aluminum alloy 2219-T87 is known for its characteristics of strength, fracture toughness, and resistance to stress corrosion cracking, which is attractive to aircraft producers (2). Aluminum alloys have a history of use for spacecraft and are currently being used on crew modules for the Artemis Program, known as Orion, and in commercial space applications. Many of the aluminum alloy types used for flight hardware have high strength but low corrosion resistance, such as 2XXX or 7XXX series alloys. Depending on the environment, chemical conversion coatings, namely hexavalent chromium versions, are used as an adhesive bond layer for primers and topcoats to protect the alloy from corrosion (8). A chromate conversion coating is a lightweight layer on metal components that can protect the substrate after accidental scratches from corrosion that can form from exposure to moisture and/or contamination. (9). In some cases, a conversion coating can be used without an additional coating to provide more limited corrosion protection. Flight hardware undergoes many different, but controlled, processes that require time, changes in temperature and humidity during the processing

stages before launching. The protective coatings need to maintain their integrity throughout processing, so understanding the corrosion mechanisms of the substrates and limitations of the corrosion control is vital for the health of a spacecraft. This literature review focused on understanding the effects of heat, humidity, and corrosion on spacecraft grade aluminum alloys that have been coated only with a chromate conversion coating (CCC) and the accompanying coating degradation phenomena, known as mud cracking.

2.1.1 2XXX Series Aluminum Alloys

The primary structural material in the aviation/aerospace industry is heat-treated aluminum and the use of aerospace grade aluminum dates to the original Wright Flyer (10,11). Aluminum alloys with both metallic (e.g., Cu, Fe, Mn, etc.) or semi-metallic (e.g., Si) elements are strong, easy to heat-treat and machine, light in weight, and low in cost, thus; aluminum alloys are widely favored and used for manufacture of commercial and military grade aircrafts (10). Aerospace grade aluminum applications range from simple components to primary load bearing structures such as the aircraft stringers and skin (12,13). In order to increase the strength of the 2XXX series aluminum alloys, alloying elements are added to the aluminum homogeneously. Copper is typically used as an alloying element to produce stronger and tougher components (14). The key features of aluminum alloy 2219 are strength, fracture toughness, weldability, and machinability with key applications in space boosters, high temperature structural aerospace sectors, supersonic aircraft skin, and fuel tanks. For example, 2219 was used to develop the external tank, or Standard Weight Tank of space shuttles (15). 2219-T87 is a variation of the 2219

aluminum alloy with a T87 temper. Mechanically, 2219-T87 has the highest shear and tensile strength of the 2219 variations and aluminum alloys overall (16). The addition of alloying elements that increases the strength of aluminum alloys may also cause pitting corrosion at locations around the intermetallic inclusions. Different 2XXX series aluminums have varying degrees of alloying elements and corresponding corrosion concerns. The alloying elements and specific corrosion issues of AA 2219 was the main focus, though AA 2024 is mentioned for reference to previous studies due to its sheer volume of historical research in relation to chromate conversion coatings.

2.1.2 Main Corrosion Mechanisms of Aluminum

Corrosion in general is the degradation of a material due to its interaction with the surrounding environment (17). All materials are susceptible to corrosion, especially metals in which the corrosion occurs by an oxidation reaction and the surface of the metal will be oxidized by the surroundings. Corrosion normally occurs at a rate determined by equilibrium between opposing electrochemical reactions. An anodic reaction occurs when the metal is oxidized releasing electrons into the metal. A cathodic reaction, in which a solution species (often O^{2-} or H^+) consumes the electrons released from the metal. When these two reactions are in equilibrium, the flow of electrons from each reaction is balanced, and no net electron flow (electrical current) occurs. The two reactions can take place on one metal or on two dissimilar metals (or metal sites) that are electrically connected.

2XXX series aluminums are known to corrode due to their alloying elements (16,17). For example, Huda et. al reported the formation of intermetallics such as Al-Cu, Al-Cu-Fe-Mn, and Al-Cu-Fe-Si-Mn on the AA 2024 substrate. These precipitates were characterized by electron probe micro-analyzer (EPMA) and scanning electron microscope (SEM), alloying elements (19). Precipitates form in the alloy and corrosion initiates at these sites due to the galvanic potential differences between the alloying elements and the aluminum base metal. In Al2219, the major secondary phase precipitates are Al-Cu which are cathodic with respect to the aluminum matrix, creating small galvanic sites across the surface (20,21). The intermetallic behavior of Al-Cu secondary phase particles has been the subject of several aluminum alloy studies (22,23). The Al-Cu phase diagram, Figure 4, is interesting in that solubility of copper in aluminum only goes up to 60% (weight % of copper) and Al2219 behaves similarly to this binary Al-Cu. The Al_2Cu phase was described initially by Owen and Preston (24,25) using XRD. Many researchers have tried to describe composition of Al-Cu binary phase in high composition ranges using SEM/EDS, but this remains unclear (24) (Figure 4). Understanding the microstructures of the aluminum alloy will promote proper processing and coating applications of the substrate. Zodiac utilized microscopy and SEM/EDS to better describe the Al_2Cu phase compositions and was able to confirm the solubility being used in the current Al-Cu phase diagrams (24). In the Al-Cu binary phase diagram, the aluminum rich area shows that pure aluminum is typically alloyed with about 4 wt.% copper at 550°C which is referred to as the aluminum α-phase. In the literature, the Al_2Cu region is at times referred to as the Θ phase and for clarity this region is referred to as Al_2Cu intermetallics in this dissertation. Thus, the major feature of Al2219 is that of a poly-crystalline aluminum microstructure with about 4 wt.% of

copper atoms fully dissolved which will naturally have dislocations and vacancies. The

high copper concentration of Al2219 deceases the potential of aluminum making it more

noble and cathodic behavior (Figure 5) to the copper precipitates. Excessive amount of

Al-Cu intermetallics can form at grain boundaries and will facilitate corrosion attack in the

material (26).
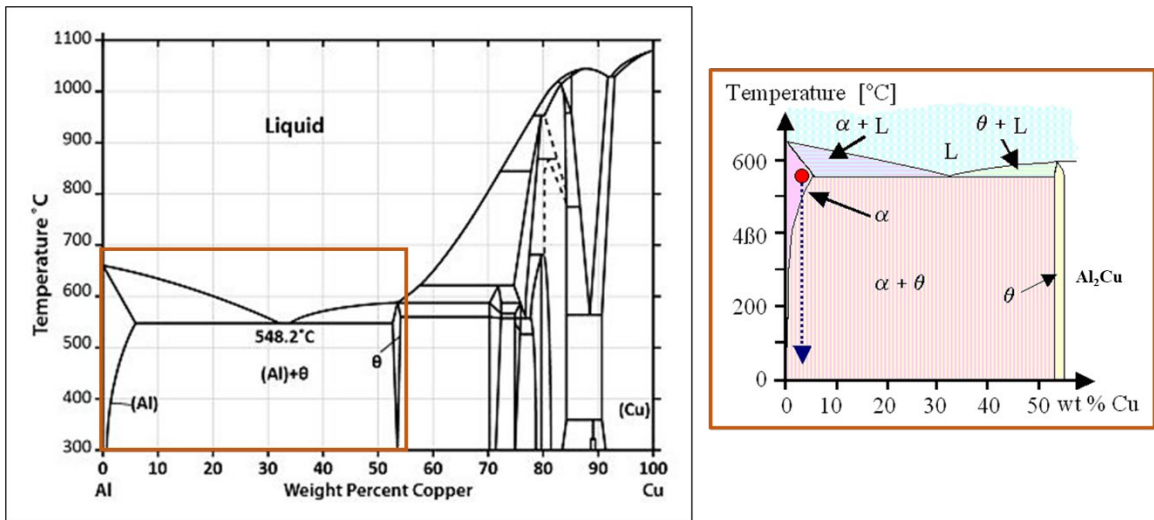
Figure 4: Binary Phase Diagram of Aluminum – Copper and the blown-up region of
interest for the Aluminum rich area (25)
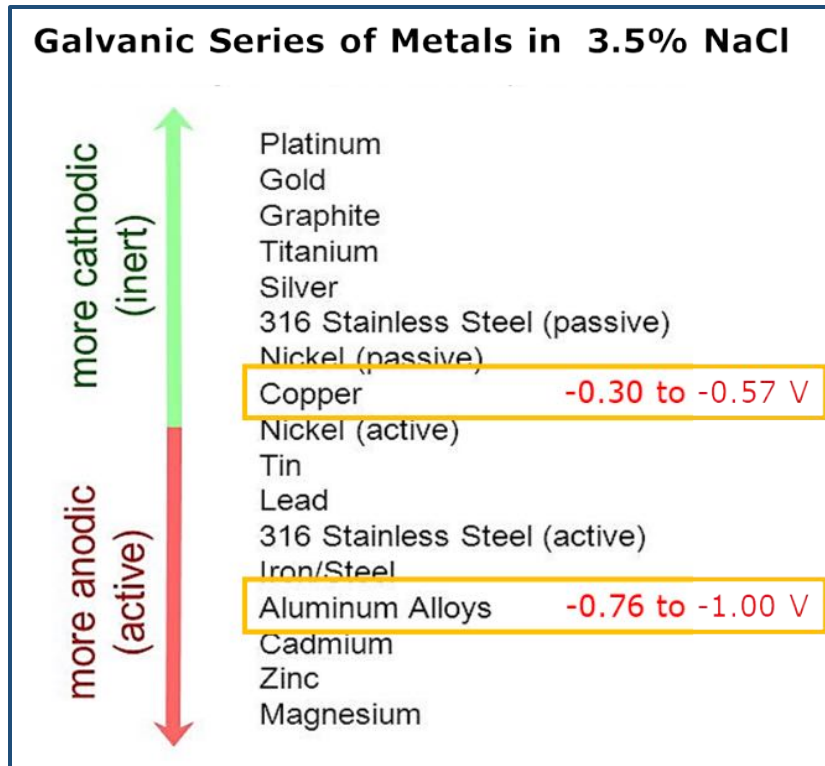
Figure 5: General electromotive force of metals and alloys measured in 3.5% NaCl with respect to a calomel electrode (27) .

Immersion studies have shown that pitting on AA2024 was primarily due to its many constituent particles, such as Al-Cu-Mg and Al-Cu-Fe-Mn (28). Al2219 has similar alloying elements (29) (22) and therefore, similar corrosion behavior as AA 2024. However, Al2219 corrodes less aggressively than AA 2024 due to the nature of precipitates (mainly Al-Cu-Mg). Table 1 lists the chemical composition of AA2024 compared to Al2219 by wt.% (30). Two types of Al_2Cu particles are produced when Al2219 is aged as can be observed using surface characterization instrumentation: (a) primary coarse particles that precipitate out of the aluminum matrix and (b) secondary fine particles that dissolve in the aluminum matrix (31–33). Strain incompatibility develops at the interface of the Al_2Cu particles and the aluminum matrix because of their differences in elastic

constants and deformation behavior. This difference essentially creates areas in the alloy
that are more susceptible to stress corrosion cracking (SCC).

Table 1. Chemical composition of AA2024 compared to Al2219 (wt.%). The
composition of major known secondary phase precipitates is shaded in grey. (34)

Alloy	Cu	Mg	Mn	Zn	Fe	Cr	Ti	V	Si	Zr	Al
2024	4.6	1.5	0.64	0.15	0.17	0.01	0.03	-	-	-	Balance
2219	6.4	0.01	0.31	0.03	0.14	0.01	0.04	0.07	0.06	0.12	Balance

Figure 6 is a schematic illustration of a primary coarse Al_2Cu particle of Al2219 that can
act as a crack initiations site. Furthermore, these particles (Al_2Cu) create areas in the alloy
that are susceptible to galvanic corrosion due to the galvanic potential generated at the
Al_2Cu/Al interface resulting with oxidation of the latter and the formation of pits.

$$2Al + 3Cu^{2+} \rightarrow 2Al^{3+} + 3Cu \quad E_a = 1.13 \text{ volt}$$
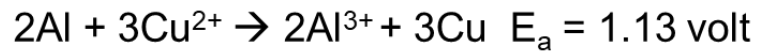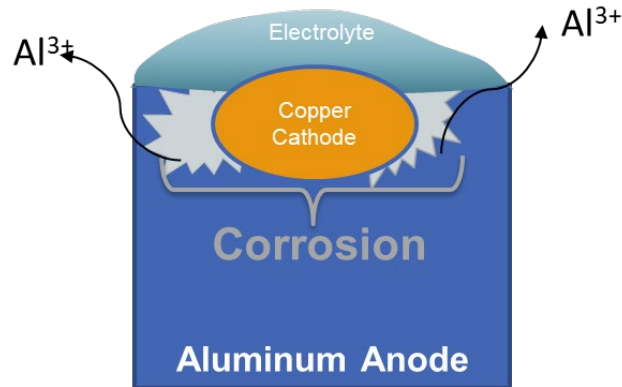
Figure 6: Representation of galvanic corrosion cell that is formed between the bulk metal
and the Al_2Cu intermetallic particles.

2.1.2.1 Corrosion of Aluminum Alloys

Aluminum can react in both acidic and basic media to form a thin protective layer of aluminum oxide on its surface over a wide range of pH. Oxygen accelerates the corrosion of aluminum as illustrated in the following chemical equations (35,36):

$$4Al + 3O_2 \rightarrow 2Al_2O_3$$
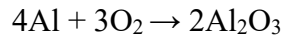
other reactions between aluminum and water:

$$2Al + 6H_2O \rightarrow 2Al(OH)_3 + 3H_2$$

$$2Al + 4H_2O \rightarrow 2AlO(OH) + 3H_2$$

$$2Al + 3H_2O \rightarrow 2Al_2O_3 + 3H_2$$
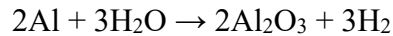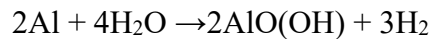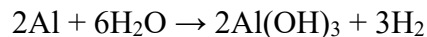
These reactions are favorable at room temperature up to aluminum's melting point (660°C). Aluminum oxide (Al_2O_3) is the most stable oxide at high temperatures and is comprised of a barrier layer on the substrate metal with a permeable oxide layer on top. This natural oxide bilayer provides corrosion protection to the substrate over a wide range of pH (37). This is illustrated in the Al-H_2O Pourbaix diagram of Figure 7 where corrosion susceptibility of aluminum is depicted. Nevertheless, the passivation exhibited by the barrier layers lies within a pH of 4.5 – 8.5 and extends to high potentials. The hydration lines between which water is stable (38,39) are represented by the following equations:

(a) $O_2 + 2H_2O + 4e^- \leftrightarrow 4OH^-$

(b) $2H^+ + 2e^- \leftrightarrow H_2$
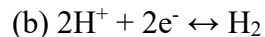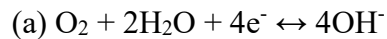
Aluminum will corrode in highly acidic and highly basic environments because the oxide layer is very soluble in these conditions. For example, chlorine can react with the oxide

layer producing hydrogen ions, which in turn break down the protective bilayer. This breakdown may lead to various forms of corrosion: crevice, intergranular, and galvanic.
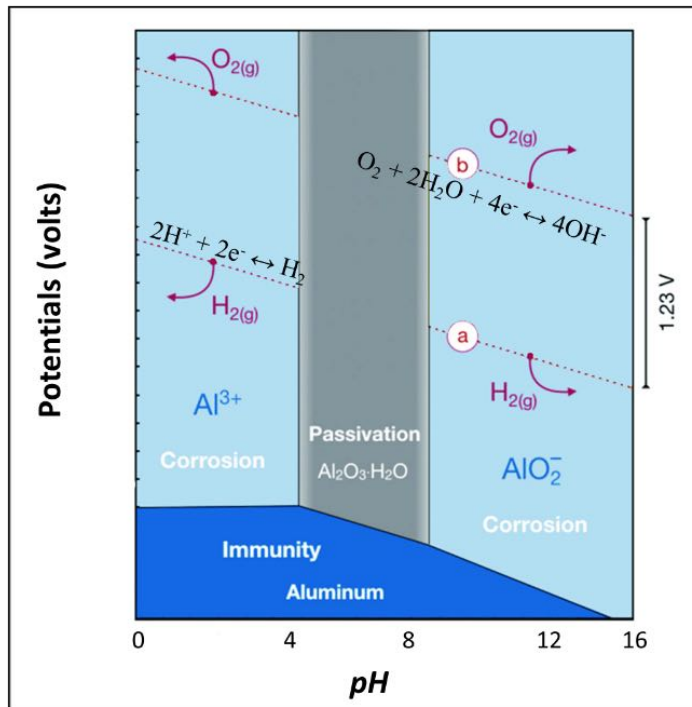
Figure 7: Pourbaix diagram of aluminum in water at 25°C showing its corrosion behavior.

Corrosion in aluminum alloys is driven by both the environment and the intermetallic compounds formed between the alloying elements and the host element. The intermetallics tend to be more noble than the aluminum matrix, which create a corrosion potential. For example, in the Al-Cu intermetallic system, aluminum is the less noble (anodic) and more active material whereas, copper is more cathodic. Thus, aluminum serves as the sacrificial anode to the intermetallic Al-Cu in a seawater environment. The passivity of both the aluminum matrix alloy (anode) and the intermetallics (cathodes) muse be taken into consideration when evaluating the corrosion protection of the alloy. In the case of Al-based flight hardware exposure to the seacoast or corrosive environments where the bilayer

oxide can be compromised, then pitting, crevice, and galvanic corrosion are all possible. Studies have attempted to correlate pitting and localized corrosion in the vicinity of intermetallic particles (40–44). Pitting features that have been reported include trenching around the intermetallics, anodic dissolution around isolated particles, and inconsistencies in the formation of metastable pits. Also, intermetallics are usually located along grain boundaries and dealloying of aluminum around copper usually occurs preferentially (45).

Intermetallic driven corrosion

Pitting corrosion is common in aluminum alloys. Pitting is an autocatalytic process where dissolution of the metals result in a breakdown of the protective passive film on the alloy surface. In the case of aluminum alloys with copper intermetallics in seawater environment, pits will initiate around the intermetallic. The pH decrease within the pit due to hydrogen ions being produced and chloride ions diffuse to the site to bring about electro neutrality causing the concentration to increases, whilst oxygen reduction takes place on adjacent surfaces to consume electrons released by corrosion of the metal in the pit, which exemplify the autocatalytic nature of pitting corrosion. As the chloride concentration increases, so do the hydrogen ions that produce hydrochloric acid, which further breaks down the oxide bilayer film. Interestingly, due to the lack of oxygen reduction within the pit, oxygen reduction occurs adjacent to the pitted area and suppresses corrosion in that area. Thus, the pit cathodically protects certain areas on the alloyed surface (46–48). Almost all localized corrosion such as pitting in aluminum alloys are from noble intermetallic phase particles especially that of copper (23). Figure 8 shows the overall dealloying pitting that occurs at the intermetallic sites. Dealloying begins and then the

alloy matrix begins to dissolve locally, and this leads to trenches all around the intermetallic and corrosion propagates deeper (49,50).
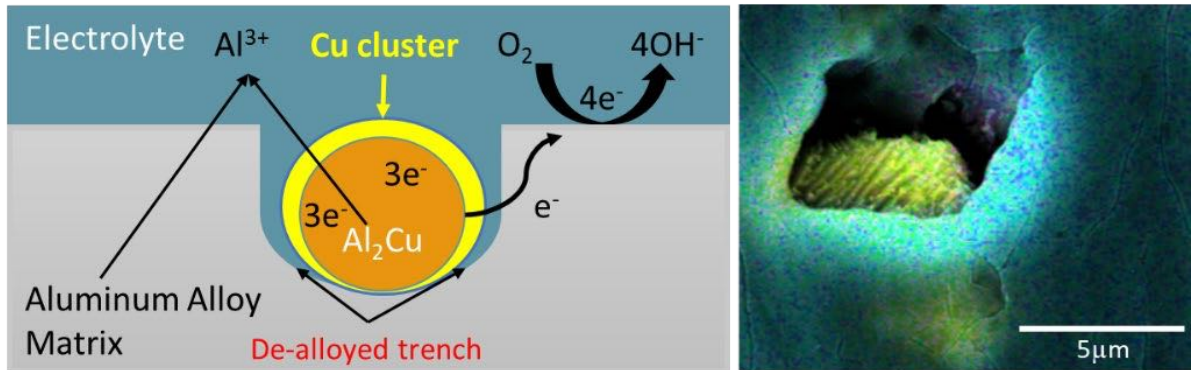
Figure 8: Schematic illustration and SEM/EDS images. (Left) Schematic of localized corrosion with pit initiating at the surface of the intermetallic particle and then propagates in the trenches of the alloy matrix. (Right) SEM/EDS image of a copper intermetallic (yellow) trenched in the aluminum matrix (blue) from this current study.

2.2   Chromate Conversion Coating Mechanism

2.2.1   Chromate Conversion Coating Process on Aluminum

Spaceflight hardware owners, including NASA, typically call-out specification, MIL-DTL-81706, Chemical Conversion Materials for Coating Aluminum and Aluminum Alloys, or MIL-DTL-5541, Chemical Conversion Coatings of Aluminum and Aluminum Alloys (which is expected to be merged into MIL-DTL-81706 in 2021) for processing of conversion coatings. CCCs are Type I chemical conversion coatings and can be further designated as Class 1A, which is thicker for maximum corrosion protection, and Class 3, which is thin and typically used for corrosion protection where low electrical resistance is also required (51).

In general, the process for chromate chemical conversion coatings on aluminum has several key steps that must be followed carefully. A conversion coating forms due to the reactions between a metal surface and a specific chemical solution in an immersion. CCC formation is essentially a redox reaction between chromate or dichromate ions in solution with aluminum. The metal surface is converted from an originally active condition to an inert film, hence the name conversion coating. Chromate conversion coatings have been used on aluminum alloys for more than ninety years (52). The general processing steps of CCC on aluminum alloys are cleaning, deoxidizing, chromating, rinsing and drying (52,53).

Conversion coatings must be applied to bare aluminum for it to react and convert the aluminum to an aluminum-chromium-hydroxide or chem-film gel. The cleaning process is required to ensure that contaminants, like grease, oil, soil etc. and the oxide film is completely removed. Cleaning is carried out using both etch and non-etch cleaners (53). This is followed by deoxidizing using acidic deoxidizers (52) which remove all traces of alkaline cleaner and activate the surface for chromating process.

The chromating process is the most critical step and it depends on several factors of time, temperature, pH, accelerator concentration, and chromate concentration. Solutions containing hexavalent chromium (Cr^{6+}) are used to develop a film on the metal surface in contact. CCC solutions are acidic and contain chromates, fluorides combined with phosphates or ferricyanides (54,55). Chromate exists either as $HCrO_4^-$ or $Cr_2O_7^{2-}$ at pH<= 2, with both ions acting as strong oxidizing agents with high reduction potentials. This helps oxidize Al and hexavalent chromium is reduced to trivalent chromium with reduction of oxygen and hydrogen evolution taking place simultaneously. For coating to form, Fe

$(CN)_6^{3-}$ first oxidizes Al to Al^{3+} and $Fe(CN)_6^{3-}$ is reduced to Fe $(CN)_6^{4-}$. This Fe $(CN)_6^{4-}$ is oxidized again to form $Fe(CN)_6^{3-}$ by Cr^{6+} and Cr^{6+} is reduced to Cr^{3+}. This results in Cr^{6+} being reduced to Cr^{3+} and Al oxidation to Al^{3+} which is accelerated by $Fe(CN)_6^{3-}$ [55]. The excess chromic acid must be rinsed off after the reaction is complete by rinsing in a bath containing regular and deionized water. This process ensures that the drag over caused by alkaline cleaner into acid deoxidizer is reduced. The final step is drying which is a controlled activity and should take place in temperatures below 60°C [13,53,54]. This gel dehydrates partially to become an oxide-hydroxide film.

2.3 The Corrosion Protection Mechanism of Chromate Conversion Coatings

The protection mechanism of CCCs has been a relevant area of study for many decades. With the advancement of analytical techniques, several explanations such as barrier layer protection, bipolar membrane mechanism, active corrosion protection, chromate in solution- anodic inhibition and cathodic inhibition were put forth explaining how CCCs protect substrate metals from corrosion. These different mechanisms will be explained, and the larger research community has combined these explanations to reach a general consensus with what is currently known.

2.3.1 Barrier Layer Protection

A chromate conversion coating can act as an inert and impervious barrier between the substrate metals and a corrosive environment. The barrier function arises from the insoluble

trivalent chromium species which is hydrated and amorphous and forms a stable layer. It was observed in multiple experiments that once the soluble hexavalent chromium species are leached out of the coatings, the insoluble portion of the film still provides a high level of corrosion protection in salt spray test. Other evidence for barrier protection suggests that after the soluble hexavalent chromium is transformed to the insoluble form by heating to 100°C, only a limited decrease in corrosion resistance was observed. These results indicate that the insoluble portion of CCC coatings does provide partial protection against corrosion (56,57).

2.3.2 Bipolar Membrane Mechanism

Sato suggested a bipolar membrane model where, as the metal dissolution proceeded, a porous, gel-like hydrated and anion selective film formed on the metal surface (58–60). When non-aggressive oxyanions like CrO_4^{2-} are absorbed on the precipitate film and the outermost layer turns cation-selective while the innermost layer remains anion selective making the precipitate film bipolar in nature. Ion transport is bipolar asymmetric and only in forward direction restricting anodic ion transference from metal to environment. The cation selective outermost layer impedes absorption of aggressive anion like Cl^-, making the film resistant to corrosion.

2.3.3 Active Corrosion Mechanism

The active corrosion protection mechanism is also referred to as the self-healing mechanism (61). In active corrosion protection, the CCC coatings self-repair when they face damage. This is possible when soluble chromate remaining in coatings dissolves and travels to active corrosion sites via diffusion or electromigration (62). The chromate gets adsorbed on the gel corrosion product and stops both anodic/cathodic reactions, thus inhibiting the corrosion damage. In this process, the release rate of soluble chromate from CCCs must not be too high as it can cause reduction of protection life of CCCs, nor should it be too low which can lead to lack of chromates in repairing damage.

2.3.4 Chromates in Solution

Chromates are strong oxidizers and its reduction products are insoluble, impervious, and passive in nature. Moreover, its speciation as an oxo anion makes it a stable corrosion inhibitor. Chromates retained in solution can dissolve into the local environment and provide partial protection offered by CCCs, which is effective in dealing with pitting corrosion and the repassivation process of corroding metals. Chromate affects metastable pitting behavior (63) like nucleation frequency, peak pit current, apparent pit radii and apparent pit current densities which educed the chance for pit stabilization, thus, reducing pitting corrosion (63). Chromium has been shown to inhibit both the anodic and cathodic corrosion reactions. As a cathodic inhibitor, reduced chromate leads to formation of a mixed aluminum-chromium oxide film, which has higher electrical resistance than alumina

film and is insoluble. This mixed oxide film inhibits cathodic activity, blocking the cathodic partial reaction(54). When the cathodic current is limited, the anodic reaction will gradually decline and prevents the metal from corroding further (64). As an anodic inhibitor, the pitting potential has shown to be reduced, which decreased the likelihood of localized corrosion initiation. Chromates have not been found to be effective in inhibiting localized corrosion growth beyond a certain point where the ratio of anions in the exposed environment becomes critical(65).

2.4 General Consensus of Chromate Conversion Coating Protection Mechanism

The multiple explanations, as highlighted above, have led to the conclusion that more than one simple mechanism is causing the surface protection. According to Buchheit et al., the self-healing process for chromate conversion coating involves the release and transport of chromate from the coat and the stifling of corrosion in damaged areas, like pits (66). Research in the last decade has led to a general consensus of how chromate conversion coatings prevent corrosion (67–72). The research supports the idea that soluble hexavalent chromium in CCCs migrates to defect areas in a coating, providing a mechanism that inhibits further corrosion. The mechanism of CCCs consists insoluble trivalent chromium oxide that is the cathodic component and the soluble and transportable hexavalent chromium species that is the anodic component. The trivalent chromium oxide acts as the insoluble and durable coating, and when damage occurs a pH-controlled transport mechanism is enabled releasing soluble hexavalent chromium species to control corrosion. The release of the active hexavalent chromium inhibitor species in CCC involves the

reversible formation of a hexavalent chromium-oxygen-trivalent chromium, Cr(VI)-O-Cr(III), mixed oxide (**Error! Reference source not found.**).
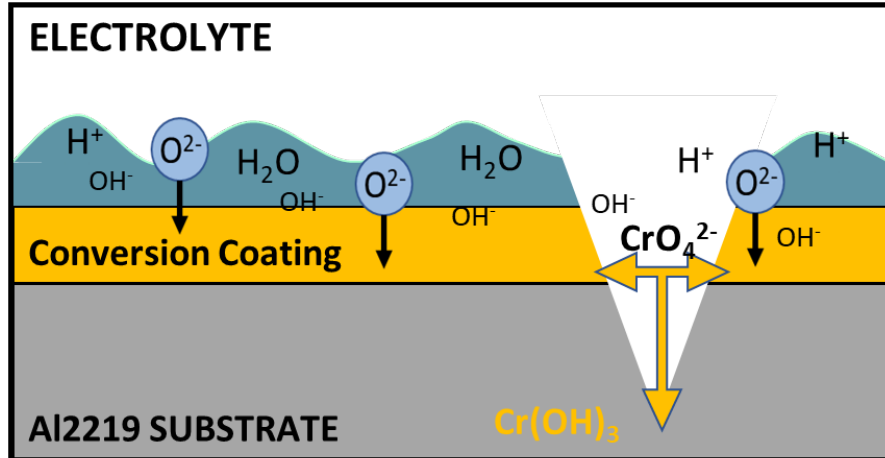
Figure 9: Schematic illustrations of the corrosion inhibition associated with Cr(VI) compounds when morphological defects (e.g., scratches) occur, the self-healing properties occur, and the barrier film forms.

2.4.1   Degradation Phenomenon of Mud-cracking of CCC on 2XXX Aluminum

The breakdown of a chromate conversion coatings can occur d ue to different factors, such as poor pedigree of the film or initial substrate, exposure to corrosive solutions, over dehydration, and aging. When used as the only layer of corrosion protection, a CCC is directly affected by environmental changes that the manufacturers did not originally intent. The CCC is meant to be an adhesive bond layer for primers, but CCCs are often used as the only form of corrosion protection when the corrosive conditions are perceived to be less likely or hardware is used for a limited lifetime. The degradation of conversions has been studied previously, and often relies on environmental exposure testing, such as atmospheric, salt fog or humidity chamber testing to understand durability. The mechanism

due to these failures is relatively well-known and will not be largely addressed in this background literature. Failure ultimately occurs via pitting at the same particulates as for the uncoated 2XXX series aluminum substrates, as discussed above in previous sections. A relatively less-studied, but relevant, degradation path that sometimes occurs prior to corrosion is the dehydration of the film, termed mud-cracking (**Error! Reference source not found.**). Several researchers have speculated regarding the occurrence of this feature and have linked it to the dehydration of the film (73–77). However, the minimum/maximum temperatures for the occurrence of this feature have not yet been derived. Nor have the minimum/maximum aging that may lead to dehydration of the conversion coating on Al2219.

Figure 10: SEM images (magnification 1000x) of the aged CCC on Al2219, illustrating the mud-cracking surface film features. Inset picture is of 10kx magnification.

CHAPTER 3

3.0 Surface Analysis Techniques used to Characterize Chromate Conversion Coating

3.1.1 Optical Profilometer

Optical profiling uses the wave properties of light to compare the optical path difference between a test surface and a reference surface. As seen in Figure 11, a light beam is split, reflecting half the beam from a test material which is passed through the focal plane of a microscope objective, and the other half of the split beam is reflected from the reference mirror. The beams are then recombined and directed to the detector. If the optical path of the two beams vary, an interference pattern will emerge. The reference mirror has a known flatness which makes any optical path difference due to height variations on the sample surface. Since the wavelengths difference between the reference path and the test path are known, height differences and surface measurements help create a 3D surface map of the sample. Optical microscopy helped observe coating morphology like amorphous nature of CCC films and developments in ambient air, dry air etc.

The fully automated Keyence Model VR-5200 Non-Contact 3D profilometer was used to provide a complete surface profile of each sample. Patterned light was emitted from the transmitter lens and projected onto the surface of the sample. As the reflected light is viewed from a different angle using the receiver lens, the light appears banded and bent due to the height changes on the object's surface. A CMOS camera is used to capture this reflected light, and based on triangulation, the height and position is calculated and provides a high-resolution surface topography of the samples. Initial surface roughness was

taken of the sample set prior to coating, and pitting density of the samples were taken after accelerated corrosion using the stitching feature. The resolution of this technique is typically sub-nanometer.
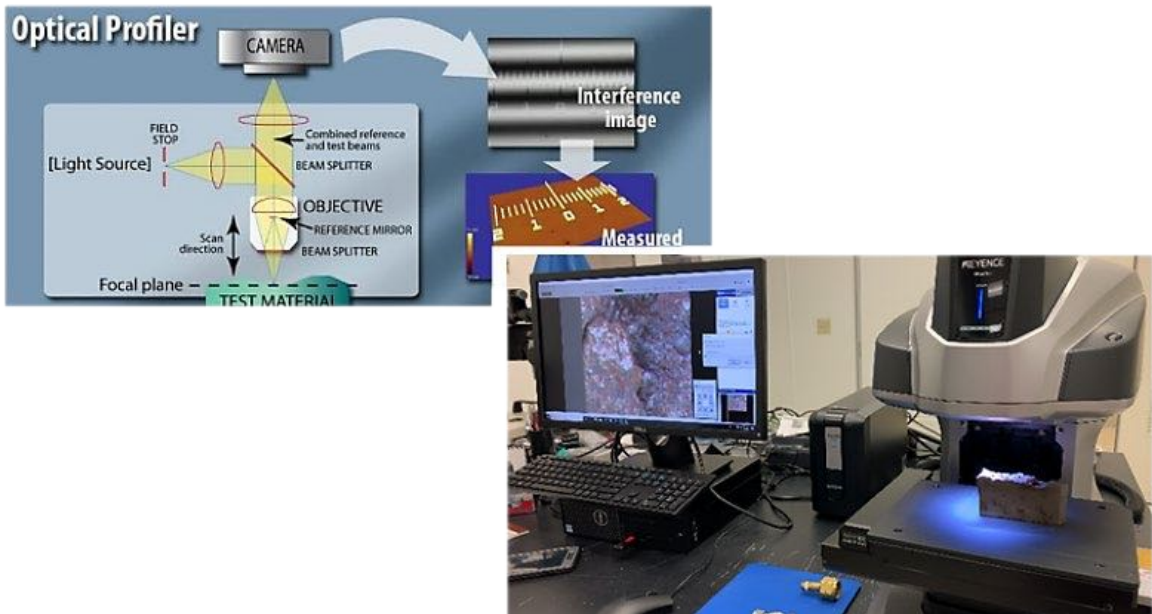
Figure 11: Images of Keyence VR-5000 (top left) working principle of the light-section method and (bottom right) instrument setup.

Three-dimensional surface mapping is a known instrument in failure analysis for evaluating hard and amorphous coatings, scratch, and wear test(78,79). Several researches have reported the use of this instrument to report damage depths, pitting, surface roughness (67,78–80). This non-destructive testing will provide pitting density across the surface and 3D mapping of the surface for comparison to the aging and heat treatment samples. This will allow a direct correlation between pitting and aging and heat treatment.

3.1.2   X-ray photoelectron spectroscopy

XPS instrumentation can detect all elements from lithium to uranium. The sensitivity of XPS is between 0.01 and 0.5 atomic percent, with a sampling depth of 0-10nm and lateral resolution of 15μm.

XPS studies have been used to distinguish between the Cr(VI) and $Cr(OH)_3$ species. Researchers were able to use XPS analysis to differentiate between amorphous surface changes and the presence of metal oxides across the surface of the substrate (81–83). Katzman et al. utilized the changes in binding energy of XPS analysis to monitor CCC coating growth on pure aluminum (83). This was accomplished by the monitoring the increase in Al^{3+} as aluminum oxidized and at the coating interface. Current research shows that that hydrated chromium oxide is linked to confirmation of CCC formation on aluminum alloys(84–86). Hydrated oxides and hydroxides of chromium were identified while small concentrations of Cr^{6+} were detected in AA2024 (43,87).

X-ray Photoelectron Spectroscopy (XPS) is a method used for surface analysis of materials. Also known as Electron Spectroscopy for Chemical Analysis (ESCA), XPS can measure the chemical state, electronic state, elemental composition, and other quantitative and chemical information from a range of materials (88,89). As one of the most standard utensils for surface analysis techniques, XPS provides a photoelectron spectrum by using an x-ray beam to irradiate the material surface while measuring within an average depth of 5nm and lateral spatial resolution of 7.5 μm. The spectrum provides many peaks that represent atoms emitting electrons of a specific characteristic energy. Through analysis of

the peak intensities, the materials can be investigated. Thus, this surface analysis technique is applicable to several research and industrial areas that observe surface layers and thin film structures: corrosion, welding, soldering, lubrication, catalysis, fibers, oxidation, fatigue, adhesives, grain boundary segregation, and more.

To understand the way that XPS characterizes material surfaces, it is important to understand and identify the different types of layers of materials. These layers include the surface layer, the ultra-thin film layer, and the thin film layer. The surface layer is ~1 nm thick with about 3 atomic layers. The ultra-thin film layer is about 1-10 nm thick with about 3-30 atomic layers. And the thin film is about 10 nm –1 μm thick with about 30-300 atomic layers (88–90). The remainder is the bulk of the material. Depending on the depth of the surface, the surface properties can be identified. Therefore, the properties of the surface layer differ from the bulk and is more reactive.

XPS analyzes the surface of materials by irradiating or heating the surface with mono-energetic Al kα x-rays at a maximum of 10 nm depth (Figure 12). Photoelectrons are emitted from the material and the kinetic energy of those photoelectrons is measured by an electron energy analyzer. A photoelectron spectrum is recorded from that kinetic energy with varying peak intensities and energies. Those varying peaks can be used to identify and quantify the material based on its chemical state, elemental identity, and quantity.

Scanning electron microscopy (SEM) and Energy Dispersive X-ray Spectroscopy (EDS) use an electron beam to create SEM images for analysis. Like SEM/EDS, physical electronics XPS instruments also use a photoelectron beam to create images for compositional analysis. The size of the PHI XPS beam is adaptable in relation to the sample sizes, where larger samples with homogeneous composition have increased beam support. However, the difference between SEM/EDS and XPS is that SEM/EDS has a depth of 1-3 μm whereas XPS has a depth of close to 5nm, which is better for thin and ultra-thin samples. This is one of the best tools used from evaluating thin films such as chromated conversion coatings that is the subject of this dissertation.
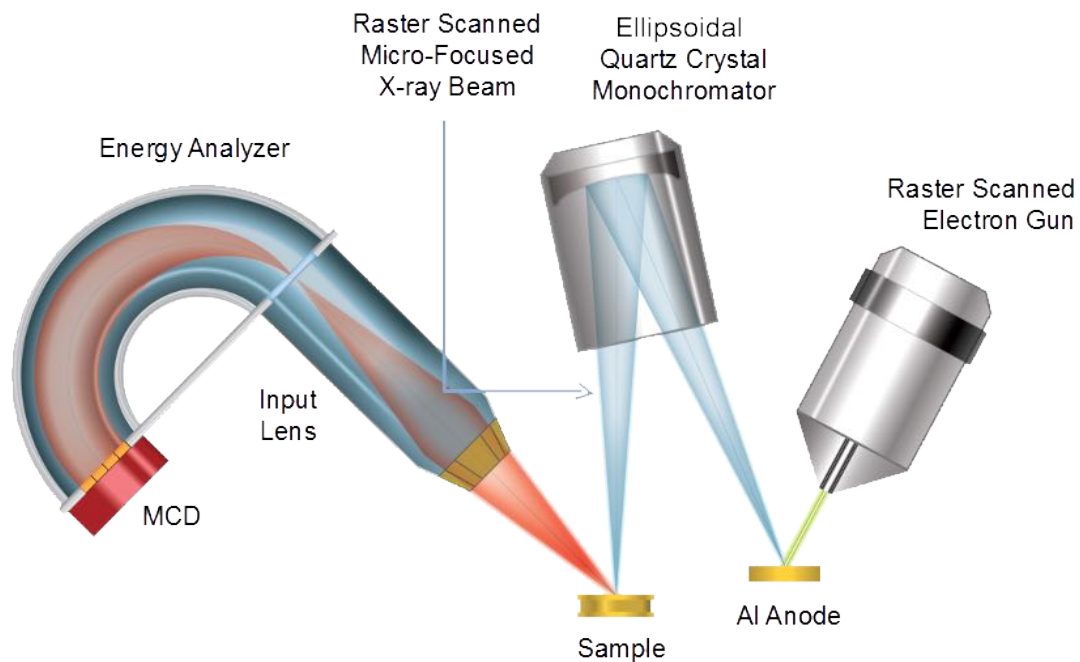
Figure 12: Focused monochromated probe in a typical x-ray photoelectron spectrometer (XPS) with reaction chambers. (91)

In XPS, the energy emitted from the photoelectrons of an X-ray is hv (usually Al Kα or Mg Kα). This energy is analyzed by the spectrometer. The data it provides is a graph of intensity (counts or counts/second) versus energy minus the x-ray induced photoelectron spectrum. Kinetic energy (E_K) of the electron is calculated by the spectrometer as different elemental characteristic excitation energies. It is dependent on the specific binding energy (E_B) of an electron and its radiation energy, hv. This calculation goes as follow (89,90):

$$E_K = hv - E_B - W$$

Within the equation, E_B represents binding energy of the electron, represents the experimental quantity of kinetic energy, hv, represents the photon energy, and W represents the spectrometer work function. As schematically illustrated in Figure 13, in the XPS photoemission process, an atom absorbs an x-ray photon and relaxes by emitting an x-ray photon or an Auger effect, where the filling of an inner-shell of an atom is paired with the emission of an electron of the atom. Measurement of the kinetic energy of the ejected electron allows for the identification of the elements within the material, the chemical states, and the binding energy of the electron.
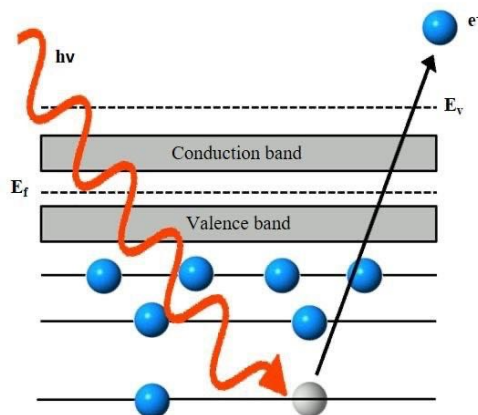
Figure 13: Schematic of the XPS photoemission process, where the x-ray (*hv*) ejects an electron from an energy level of the receiving atom (86).

The photoemission spectrum that is produced will include all the electrons with a binding energy less than the photon energy. The energy loss does not contribute to the spectrum peaks but to the background. Thus, XPS photoemission spectrums are accurate representations of the actual surface of the material. Depth profiling can be used to get the same profiling for the bulk of the material.

Qualitative Spectral Interpretation

The product of XPS is a spectrum. To describe spectral interpretation, a sample spectrum of the 2219 aluminum alloy is provided in Figure 14 using a wide energy range. Initially, characterization starts with identifying the elements within the material surface by recording a wide scan spectrum with a range between 0-100eV or higher. Within the scan, the strong photoelectron peaks can be used to identify elements based on their peak binding energies. For the 2219 aluminum alloy sample, the elements within the material surface are

carbon (C KLL), aluminum (Al KLL), oxygen (O KLL), and chromium (Cr LMM). In the

scan, the y-axis represents the intensity of the electron counts per second and the x-axis

represents the kinetic and binding energy. From left to right, the kinetic energy increases

and the binding energy decreases.
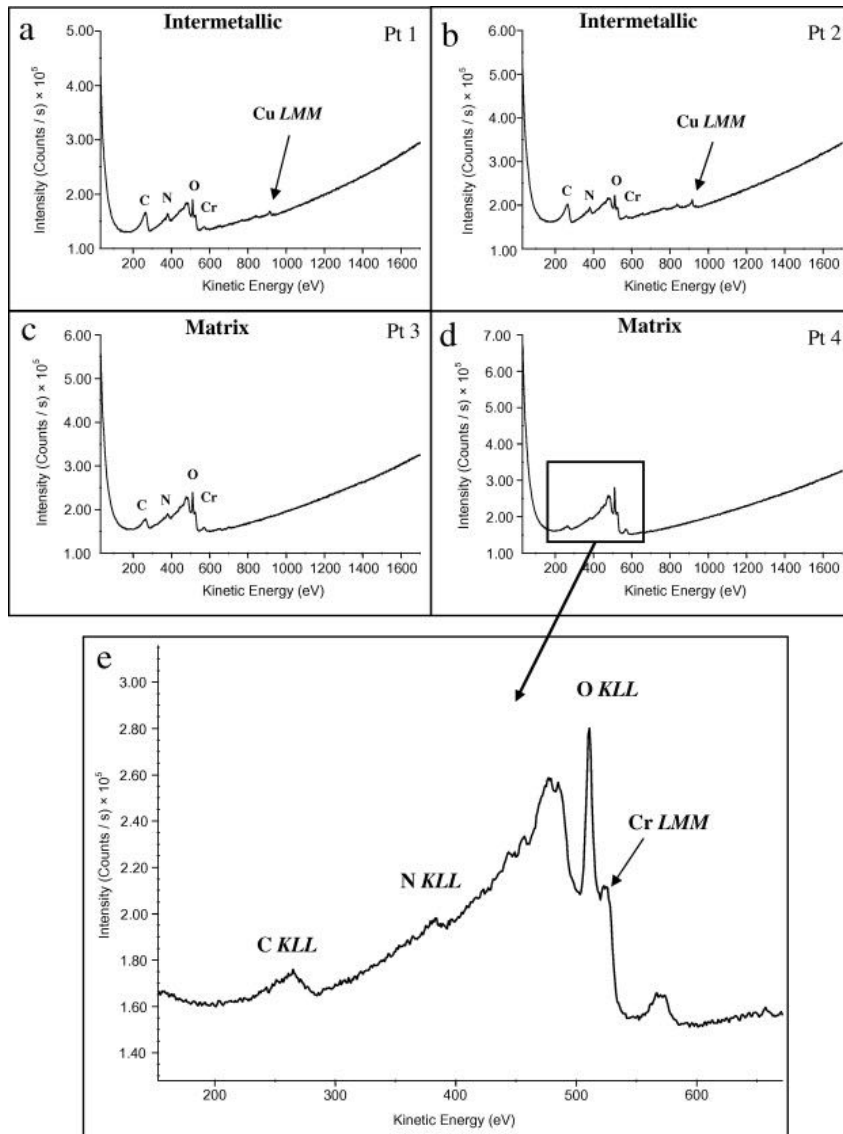
Figure 14: XPS examples of Auger spectra of a specimen coated with chromate
conversion coating; (a) point 1 on the intermetallic; (b) point 2 on the intermetallic; (c)
point 3 on the matrix; (d) point 4 on the matrix; (e) is an expansion of the region in the
point 4 spectrum (85)

The scan or spectrum that is recorded may contain scattered background static in the form of smaller peaks. The background is produced by a mix of the Bremsstrahlung radiation, which is a broad, continuous radiation, and the loss of energy from a portion of electrons through inelastic scattering. Inelastic scattering is when there is an interaction that causes loss of energy and produces reduced photoelectron peaks. Inelastic scattering reduces kinetic energy and intensity from peaks. Elastic scattering is when there is no loss of energy and produces major photoelectron peaks. It is suggested that the background produced from inelastic scattering is removed before quantification.

Photoelectron peaks are grouped into core levels, valence, levels, and Auger series. Core levels are electron structures of atoms that can be singlets or doublets with energies that provide information about the chemical state. Valence levels have low energy electrons in bonding orbitals. Auger series occur during relaxation of the excited atom – Auger effect.

The XPS spectrum also has other secondary unwanted features such as x-ray satellites and x-ray ghosts. These features have no analytical use. X-ray satellites occur if non-monochromated radiation is used. While x-ray satellites are expected, it may present a limitation if they occur at the elemental photoemission peaks. X-ray ghosts are from unsuspected x-rays irradiating the sample. Both x-ray satellites and ghosts occur when the atom has impurities that produce x-rays.

A solution for x-ray satellites, x-ray ghosts, and Bremsstrahlung continuum may be to use a monochromator, where the goal of a monochromatic x-ray would be to reduce

background, satellite and ghost peaks, and narrow peak widths. In a Roland circle, the monochromator selects a line doublet through diffraction in a crystal lattice and when the x-ray reaches the lattice, the x-rays disperse and focuses on the sample. Figure 4 provides a visual of the apparatus.

The Bragg's Law equation can be used to explain why the crystal lattice reflects x-ray beams at specific angle(89,93)s: $n\lambda = 2d \sin\theta$

Within the equation, n represents the order of diffraction, λ represents the wavelength of interest, d represents the crystal lattice spacing, and θ represents the angle of diffraction (91).

Quantitative interpretation

When quantifying the XPS spectrum, consider sample-related factors and spectrometer-related factors. Sample related factors are cross-section for emission and the escape depth of the ejected electron. Cross-section for emission is the probability of the emission of an electron due to radiation, which is dependent on the material, orbital, and energy of the radiation. The escape depth of the emitted electron is dependent on its kinetic energy and the material's nature (94,95).

Spectrometer-related factors are the transmission function of the spectrometer, efficiency of the detector, and the magnetic fields that affect the transmission of low-energy electrons. The transmission function of the spectrometer is the portion of electrons that are

transmitted as a function of their kinetic energy. The efficiency of the detector depends on its ability to detect electrons that strike it. Magnetic fields that affect the transmission of low-energy electrons must be considered because it may affect low-energy electrons more than high-energy electrons.

To quantify XPS, the intensity of a photoelectron peak from a homogeneous solid can be found using the following equation(96):

$$I = J\rho\sigma K\lambda$$

Within the equation, I represent intensity, J represents photon flux, ρ represents the concentration of the atom, σ represents cross-section of the photoelectron, K represents instrumental factors, and λ represents the electron attenuation length. The intensity can also be referred to by the integrated area under the peak following the subtraction of the background.

After intensity is determined, σ, K, and λ can be used to determine sensitivity factors that affect the concentration of elements in the sample. The atomic percentage can be determined if the x-ray flux remains constant by using the following equation(96):

$$[A] \text{ at\%} = [(I_A/F_A)/\Sigma(I/F)] \times 100$$

Summary of XPS

A limitation of XPS is that the smallest area that XPS can measure is about 10 μm. A few other limitations are that XPS is restricted to ultra-high vacuum environments, XPS provides a limited amount of information, and XPS cannot detect hydrogen or helium because of its restricted measurements of elements with an atomic number of 3 or greater. However, the advantages of XPS is that outside of hydrogen and helium, XPS can detect all elements. XPS has a greater range than most other applications and can identify and detect the difference in chemical states of sample surfaces (96–98).

3.1.3   Scanning Electron Microscopy with Electron Dispersion

Researchers studied the chromating steps using Scanning Electron Microscopy (SEM) and found that more etching time in the pretreatment removed a large number of cathodic sites (99,100).   Sun et. Al. and others have used SEM/EDS to monitor composition of conversion coatings before and after to corrosive environments (30,100). Lunder et. al. was able to perform high resolution surface analysis of the role of microstructure in conversion coating formation on aluminum substrate (101,102). A detailed microscopic study of etchant attack and pitting in conversion was examined by Mo et. al. (43,87,103). The researchers found that local attack on the aluminum matrix of AA204 consisted of severe pitting, resulting in grain boundary attack and subsurface etch out. Using EDS it was determine that there were high concentrations of chlorides present inside the pit. High resolution SEM (87,102) and TEM helped observe cathodic overpotential and features like mud cracks on CCC. Bulk intermetallics were examined in Al7075 using SEM and a full phase analysis of the elemental composition was obtained through EDS (104). Using this

technique, the coarse intermetallics were clearly identified and coating formation on the substrate was confirmed.

Characterization of the metal to coating interface is important to understanding the limits of the conversion coatings on flight hardware. Moreover, SEM will be used to identify intermetallic pitting and the monitor the mud-cracking conversion (1975 Navy SJ Ketcham,) coating feature as a function of heat treatment and aging. Several researches used SEM secondary electron micrographs to identify the mud-cracking morphology and topography of CCC treated aluminum alloys 7075 (86,105).

Scanning Electron Microscopy (SEM) uses an electron beam to enlarge features on material surfaces and form images in the optical light microscope. SEM has three different components – the computer control system, electron column, and the specimen chamber (Figure 15). Because SEM samples are scanned with an electron beam and produces signals of information about the sample, SEM is named Scanning Electron Microscopy. The SEM electron beam interacts with the sample and emits an x-ray whole energy can be measures to determine the composition of the material. Thus, SEM can be used to identify the structure, composition, contaminants, and imperfections in the material. More specifically, the following can be found using SEM: morphology, phase distribution, surface topography, atomic number, elemental identification and quantification, x-ray maps, and more.

Figure 15: Schematic image of NASA KSC Scanning Electron Microscope (SEM), TESCAN FIB-SEM typical with major components labeled.

While the resolution of a human eye is 200 μm, a light microscope has a resolution of nearly 0.2 μm. In other words, two objects that are 200 μm away from each other will be seen as one object, but if it is seen under a light microscope or SEM they would be seen as two separate objects. In SEM, the electrons have smaller wavelengths, allowing it to reveal finer details compared to other optical microscopes. Thus, the resolution of SEM is high with a magnification of nearly one million times the original size and a resolution smaller than 1 nm (106). The following equation is used to find the useful magnification of a microscope:

Useful magnification of a microscope = resolution of human eye / resolution of microscope

Thus, the useful magnification of light microscope is ~1,000x and the useful magnification of SEM is ~200,000x.

Compared to traditional machines, SEM is one of the more efficient in terms of power and versatility. Where traditional machines use thermionic emission to attract electrons to a positive anode, current machines may use a Field Emission Gun (FEG) which emits electrodes from an electric field gradient caused by a highly negative emitter near an electrode. The benefits of using a FEG is a smaller beam with higher brightness, clarity, and consistency. The beam produces detectable secondary electrons and back-scatter electrons when it interacts with a material surface (107).
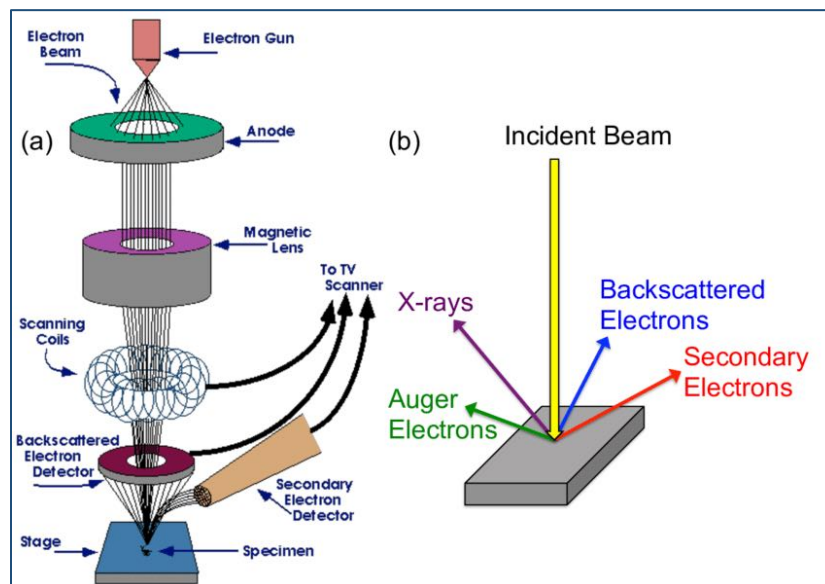
Figure 16: Schematic drawing of (a) the typical Scanning Electron Microscope (SEM) column and (b) sample-beam interactions within a SEM (107).

Everhart-Thornley detectors, like the TESCAN Amber SEM/FIB used in this research, are scintillator-photomultiplier systems that can detect secondary electrons and back-scatter electrons (108). Secondary electrons are ejected from the sample because of inelastic interactions from the sample and beam. When imaged, secondary electrons are low-energy electrons that can provide topographical information about a sample. They can also provide

information about the chemical composition and ionization state of a sample through the emission of a photon from the energy lost in a core shell where the secondary electron was ejected.

Back-scatter are high-energy electrons that provide information about the atomic number and phase of a sample. They are ejected from the sample because of elastic scattering from a sample. For backscattering, because heavy samples scatter more than light samples, the atomic contract can be found through symmetrical collection of those electrons.

There are many benefits and limitations of SEM. The benefits include the speed of imaging and analysis, high spatial resolution, and versatility. SEM is known for its quick and efficient sample preparation and results. Combined with its user friendliness, comparative affordability, and platform supports of other devices and tools, SEM is helpful for a broad range of disciplines including materials and life science. The limitations of SEM are relative to its conditions and preparation. SEM sample sizes are limited, and the samples must be solid, although the solid could be dry or wet. The samples must be analyzed in a vacuum, and non-conductive samples must be coated. It should also be noted that EDS detectors cannot detect the element: H, He, or Li.

Energy Dispersive X-ray Spectroscopy

Energy-Dispersive X-Ray Spectroscopy (EDS) is used with Scanning Electron Microscopy (SEM) as a microanalytical tool that characterizes materials based on their chemical and elemental properties. EDS uses the x-rays generated by a sample from its interaction with

a primary electron beam to identify and characterize the sample. EDS is dependent on the ionization of atoms through the ejection of inner shell electrons from incident electrons. The hole that is left in the inner shell is called a relaxation process, which creates photon emission of x-rays. The photon x-rays that are generated are collected by the detector, converted to ana-electrical signals, and used to determine the chemical composition of the sample through a spectrum. The inner shell hole and the ejected electron produce a charge from their division that is proportional to the energy of the x-ray. Thus, quantitative data is produced using the spectra to determine the elemental concentrations.

EDS is capable of providing both quantitative and qualitative analysis. For quantitative analysis, the energies in the EDS spectrum are referenced with known x-ray energy values. Qualitative EDS analysis is limited by elemental atomic numbers ranging from beryllium to uranium, and the minimum detection limits range from 0.1 to a few atom percent.

After qualitative EDS analysis, the level of concentrations within the sample are determined through quantitative EDS analysis by using known specimens with standards that are similar in composition to unknown specimen that are being analyzed. The spectrums are compared to find the concentrations of the elements within the unknown sample. Higher concentrations (10 wt.% and more) are identified as major elements while lower concentrations are identified as minor elements (1-10 wt.%) (108). The higher the concentration, the higher the quantified accuracy.

Another method of quantitative EDS analysis is through standardless semi-quantitative actions, where mathematical corrections are made based on the composition of the sample

and the parameters of the analysis. Thus, only the unknown sample is analyzed, and it is compared to spectral data that is stored on the computer. While the procedure is quick and less cumbersome, this technique is less accurate. For the purposes of this research, EDS analysis will be focused on qualitative interpretation of the trends observed on the samples.

Elemental mapping is usually used in combination with SEM using EDS. Elemental Mapping is an imaging technique that develops a high-resolution image of the sample from the EDS results. It develops an image based on the spatial distribution of elements within the analyzed sample. Elemental mapping works by measuring the characteristic x-ray intensities and comparing it to the lateral position of the sample. The elemental maps are recorded simultaneously, and an example is shown in Figure 17. The maps use brightness intensity as a function of relative element concentration, and elemental mapping has ~1 μm lateral resolution.
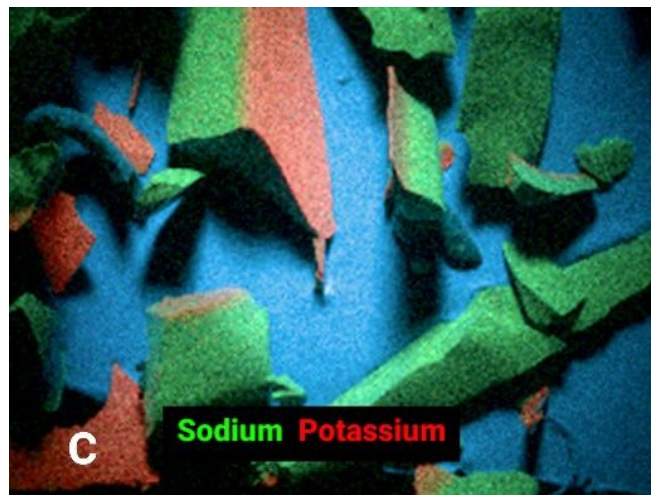
Figure 17: Example of elemental mapping using TESCAN SEM with Aztec EDS software where each color corresponds to a specific element (103).

44

Profile Analysis is usually used to quantify structural parameters of nanomaterials and characterization of microstructures in crystalline specimens(110). In Line Profile Analysis, the SEM primary electron beam is scanned from a line across the sample. The x-rays are detected to determine the discrete positions along the line. The x-rays that are detected are analyzed at each position to determine the relative elemental concentration of the elements in relation to its position on the line.

Where EDS identifies elemental compositions in SEM samples, the application of EDS involves materials evaluations in terms of contaminants and elemental diffusion profiles. Other applications include foreign material analysis, failure analysis such as Stringer location and identification of unknowns, and quality control such as material verification and plating specification. This paper focuses on its applications in corrosion evaluations and coating composition analysis.

For SEM, the smallest sample size that can be analyzed is 8 inches (200nm) in diameter (106,108). Sample size can be as big as 12 inches (300 nm) in diameter and will have limited stage movement. The height of the sample has a maximum of 2 inches (50nm). The sample is usually polished down to 0.1 μm. When loading, samples must be flat and stable under the beam. The sample must be able to undergo a moderate vacuum atmosphere (pressures of 2 Torr or less).

Like SEM, EDS has a few benefits and limitations. One of the benefits of EDS is its ability to detect multiple elements simultaneously. EDS is quick because of its high efficiency and large solid angle of collection (~0.5 steradian)(108). While EDS can be versatile, user-

friendly, small, and highly efficient, the limitations that it has are low-energy resolution (122eV), low detectability of elements (0.1-0.2 wt.%), and low sensitivity to minor and lighter elements compared to the wavelength dispersive x-ray spectrometer (WDS)(111).

In this work re-occurring features were found in the samples and are briefly described here. In SEM, the mud-cracking morphology is easily observed in magnification as low as 500x. The features are described as follows based on Figure 18: (A) the typical mud-cracking morphology for conversion coating that has been reported and is a known feature in some coated samples, (B) the mud-cracking formation of islands, (C) the width between islands as dehydration and/or aging increases, (D) crushed islands, (E) jagged edges along the separated islands, and (F) potential initiation points.
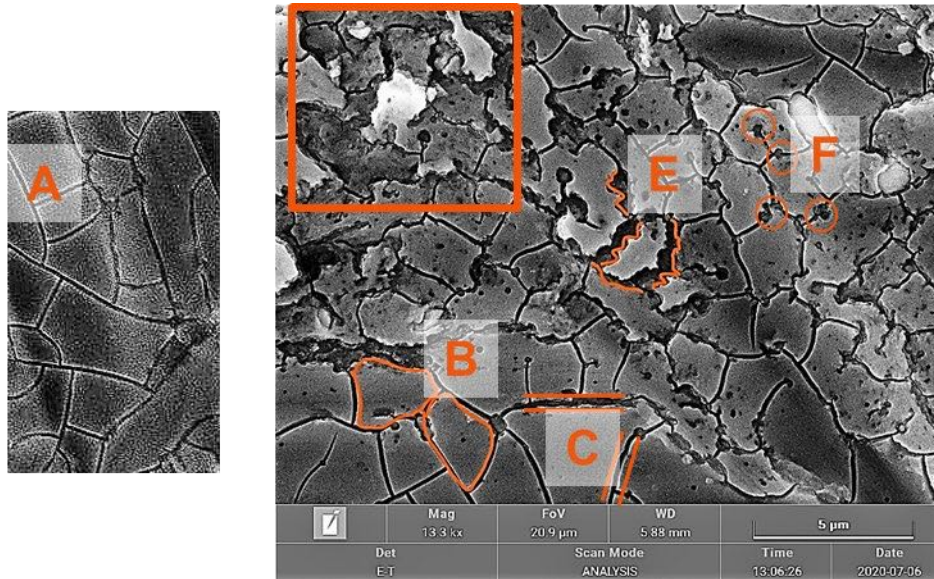
Figure 18. SEM image of mud-cracking morphology with key features delineated: (A) the typical mud-cracking, (B) formation of islands, (C) the width between islands, (D) crushed islands, (E) jagged edges along the separated islands, and (F) potential initiation points.

3.1.4 Electrochemical Methods

The chemical conversion coating technique has been extensively applied onto conventional metallic materials for corrosion protection. The corrosion behavior of the chromated aluminum surface was investigated by means of electrochemical impedance spectroscopy EIS (112,113). The characterization of surface layers formed by either chemical or anodic surface treatments is among the various applications of this technique (113,114) . Zhang also conducted studied CCCs using many surface sensitive characterization techniques which help understand structure, morphology, composition, and traits of CCC (115,116). The electrochemical techniques will all collectively provide information regarding the corrosion protection provided by the CCC treated aluminum substrate as a function of aging and heat treatment.

Electrochemical Impedance Spectroscopy or EIS helped quantify factors and variables of corrosion resistance and define values of indentation damage, effects of ageing etc. of CCCs. Campestrini et. al. carried out electrochemical studies of CCC treated Alclad 2024 alloy in 3.5% NaCl solution and monitored the concentration of intermetallics on the surface based on the current density of cathodic sites (53,99,112). Correlation between electrochemical properties and corrosion of trivalent chromium coated AA2024 in salt fog exposure were evaluated by Dr. Munson group (117). The group was able to show a minor link between negative open circuit potential and lower coating capacitance to samples that failed in salt fog testing(117). Salt fog testing vary greatly alongside electrochemical analysis, and more testing need to be done before being able to accept this process as a clear indicator for predicting corrosion resistant coating. While electrochemical testing is

much faster than salt fog testing, it cannot be used as a stand-alone test for coating corrosion prediction. Electrochemical studies, such as Zhang et al, can be used to evaluate CCC anodic reactions and to measure the resistance breakdown of the electrode (54). Ultimately, it was concluded that anodic inhibition by CCC may be controlled by the aggressiveness of the electrolyte and coating breakdown via pitting can be in the substrate or in the coating. Discerning between defects due to surface intermetallics or defects in the coating was challenging. But these defects were captured in the low potential and resistance to breakdown decreased more so at the net cathodes than the net anodes.

3.1.4.1 Open Circuit (Corrosion) Potential

Open circuit potential (E_{OC}), also referred to as corrosion potential (E_{corr}), is a simple technique used to monitor the substrate surface in an electrolyte solution. During open circuit potential, no potential or current is applied during the measurements so that the overall potential value of the system at open circuit conditions can be measured. This is considered the general baseline of the substrate's surface at this point the substrate has both anodic and cathodic currents present which allows it to be at equilibrium with the electrolyte(118). E_{corr} is then defined simply as the potential where both the rate of oxidation and the rate of reduction are equal. This method is considered passive and is used to determine the resting potential of the system. OCP was used to determine the electrochemical stability of the non-coated and coated samples prior to performing further electrochemical measurements. OCP ensures that the system is thermodynamically stable and provides greater confidence in measurements. For all samples, a stable OCP was

obtained prior to running other electrochemical testing. The current response as a function

of potential over time is plotted. Shown in Figure 19, E_{corr} values correspond to where the

anodic (i_a) and cathodic (i_c) current densities are equal.
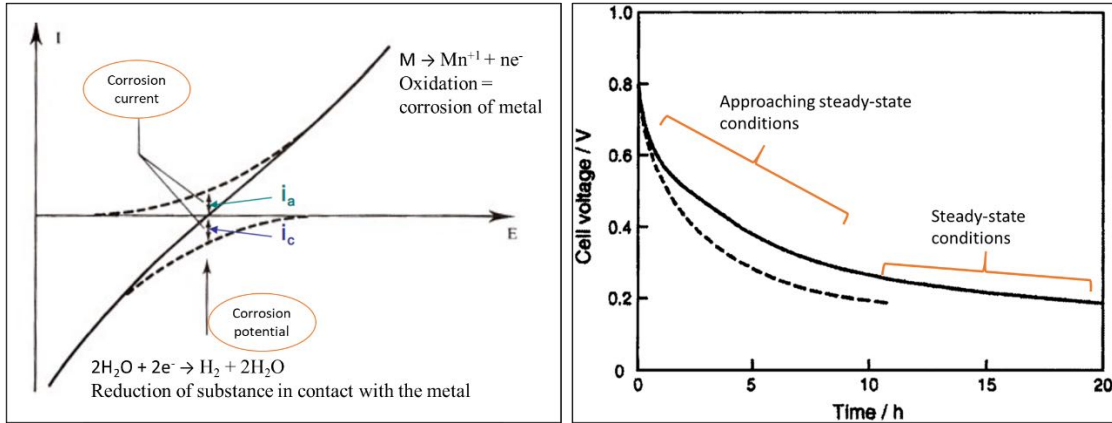
Figure 19: (Left) Potential vs current density plot showing where anodic and cathodic reactions are equivalent. Ecorr is where $i_a = i_c$. (Right) Schematic illustration of open circuit potential (V) versus time (h).

Corrosion potential measurements accurately provide information that can be translated to

the condition of the substrate, such as whether passivation or corrosion is occurring at the

surface of the metal. Figures xx shows the basic schematic regions on an open circuit

potential versus time plot. The figure illustrates that the potential begins at a high potential

and after continued immersion in electrolyte the metal electrode begins to approach steady-

state potential values. However, the dotted line has not reached steady state and was still

out of steady state before the experiment ended.

E_{corr} values are important to note prior to most other electrochemical measurements, mainly

because understanding the state of the electrode (whether anodic or cathodic reactions are

controlling or steady state conditions are occurring) prior to the other measurements is

necessary in interpreting other subsequent measurements (such EIS and polarization resistance).

3.1.4.2 Linear Polarization Resistance

Linear Polarization Resistance (LPR) is an electrochemical method for measuring the corrosion rate of a material in electrolyte. Polarization resistance scans through the potential range that is about ± 25 mV of the measured E_{corr}. The plot of polarization resistance is given as current versus potential as seen in Figure XX. Unlike the open circuit potential measurements, polarization resistance (R_p) provide corrosion rate information. After performing the passive open circuit measurements and obtaining steady state, the non-destructive LPR electrochemical analysis was performed to obtain the corrosion rate of the samples as a function of heat treatment and aging. The corrosion rate is obtained indirectly using the Stearn-Geary (119) relationship between potential and current given by:

$$R_p = \Delta E / \Delta I$$

where E is the potential, I the current, and R_p the polarization resistance. The polarization resistance is inversely proportional to the corrosion current, and thus to the corrosion rate. The corrosion current can be calculated using (120):

$$I_{corr} = 1/R_p (\beta_a \beta_c) / 2.303 (\beta_a + \beta_c)$$

where β_a and β_c are the anodic and cathodic Tafel constants, respectively.

Since the corrosion current and the corrosion rate are directly proportional, the corrosion rate can be calculated by determining the corrosion current density from the Stearn Geary equation. The corrosion rate can then be solved by dividing the corrosion current by the

area of the exposed substrate in electrolyte as shown in the below equation:

$$CR \text{ (mpy)} = K_1 \text{ EW } (i_{corr}/\rho)$$

where K_1 is a unit conversion constant, ρ is the density of the material, and EW is the equivalent weight. The corrosion rate was calculated using the following values: $K_1 =$ 3.27 x 10^{-3} mm·g/μA·cm·yr, EW = 26.9815, and $\rho = 2.85$ g/cm^3 for aluminum. High corrosion rate values indicate an increase in general corrosion across the surface area.
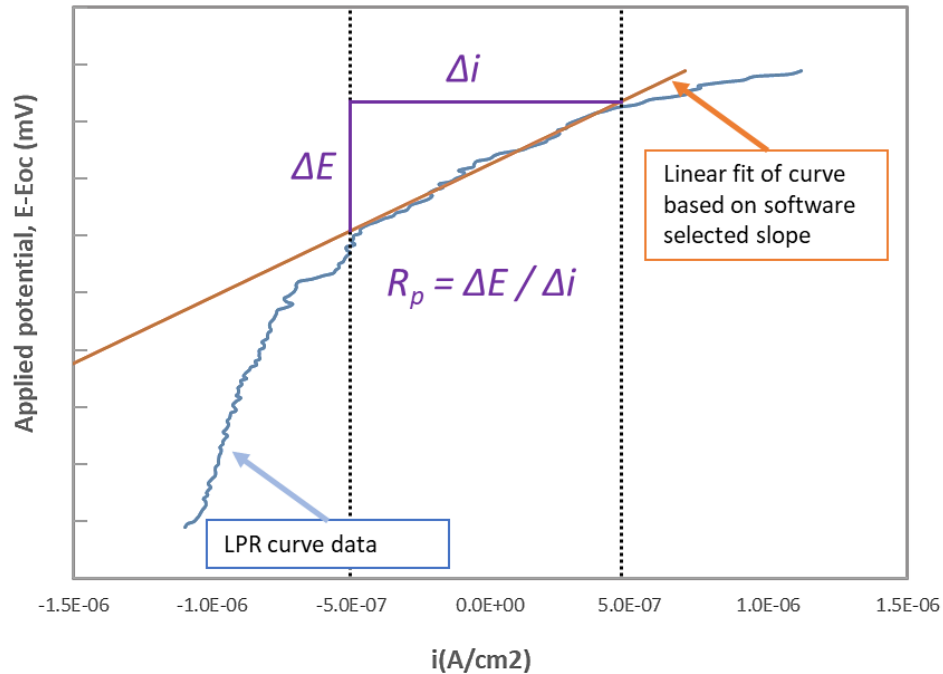
Figure 20: Experimentally measured polarization resistance in 3.5% NaCl.

Figure 20 is an example of a polarization curve where a potential, ±10 mV vs E_{corr}, was applied and was used to measure the ΔE/Δi slope. The solid blue line represents the measured data, the line with the dotted lines on either side is the region selected to calculate the slope, and the gold line is the best fit line based on the selected slope. The ΔE/Δi slope was used to measure corrosion rate in mpy.

3.1.4.3 Electrochemical Impedance Spectroscopy

In electrochemical impedance spectroscopy (EIS), the response of an electrode to alternating potential signals of varying frequency (AC voltage) is interpreted on the basis of circuit models of the electrode/electrolyte interface (46,121). The EIS technique was used to determine polarization resistance and to model the corrosion process by fitting impedance data with corresponding equivalent circuits (Figure 21). The modeling procedure uses electrical circuits built from components such as resistors and capacitors to represent the electrochemical behavior of the coating and the metal substrate. In EIS, the impedance of the corroding metal (working electrode) due to an applied sinusoidal potential change (AC voltage) is analyzed as a function of frequency, ω. At each frequency, the resulting sinusoidal current waveform, and the applied potential are out of phase by phase angle (θ), whereas the current amplitude is inversely proportional to the impedance of the interface (122). The electrochemical impedance, Z (ω), is the frequency-dependent proportionality factor in the relationship between the voltage signal and the current response:

$$Z (\omega) = E (\omega) / i (\omega)$$

where, E is the voltage signal, $E = E0 \sin (\omega t)$; i is the current density, $i = i0 \sin (\omega t + \theta)$; Z is the impedance (ohm - cm2); and t is the time (seconds) (122,123)

Impedance is described by the frequency-dependent modulus, |Z|, and the phase angle, θ, or, alternatively, by the real component, Z′, and the imaginary component, Z″ (46). In electrochemical impedance analysis, three different types of plots are commonly used: (1)

Nyquist plot, (2) Bode impedance modulus, and (3) Bode phase angle plot. Figure 21

illustrates the EIS plots. The Nyquist plot which shows complex plane Z'' vs. Z' and the

capacitive semi-arc is used to provide an estimate of corrosion resistance of the material.

The semi-arc diameter is directly proportional to the charge transfer resistance or

polarization resistance (R_p). Ann increase in semicircle diameter correlates to an increase

in corrosion resistance (121,122).
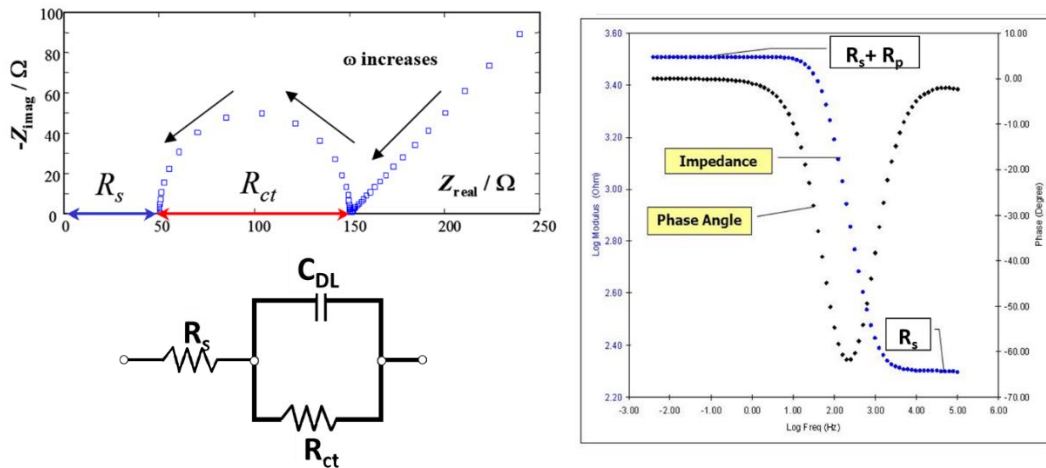
Figure 21: (left) A typical Nyquist plot that depicts the real and imaginary impedance values, on the XY- axis, respectively and (right) Bode plot that shows log frequency on the x-axis, and both the absolute value of the impedance Log Z and phase-shift θ on the y-axis. The Randles circuit used to describe both of these plots is pictured on the bottom. (114–116)

Real world electrochemical data processes hardly ever show pure capacitance, during EIS

analysis, the non-ideal response of the corrosion system is represented by a C_c to obtain

accurate impedance values(126,127). Bryan H et. al. has shown that C_c behavior can be

attributed to the distribution of physical properties of coatings in a direction normal to the

electrode's (substrate) surface (81,128).   EIS is graphs are generally interpreted

qualitatively. The two general equivalent circuit modes used to represent the bare Al2219 substrate and the CCC treated Al2219 samples in this research are shown in Figure 22.
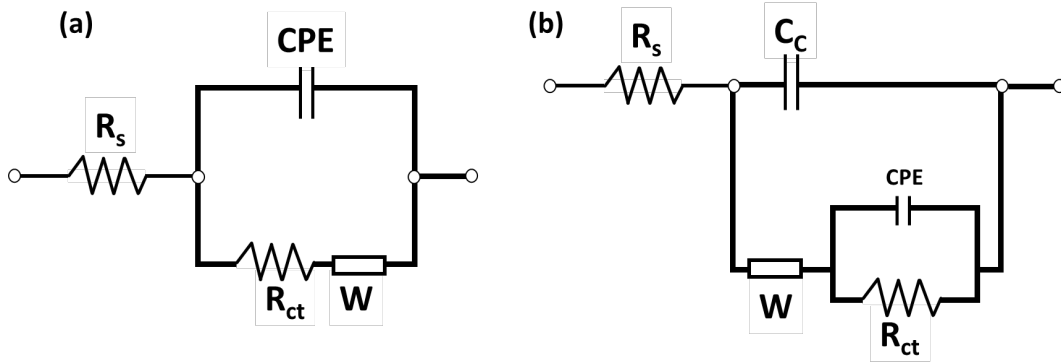
Figure 22: (a) A modified Randles cell model typically used for non-coated metal substrates and (b) a modified circuit typically used for thin coated substrate.

Parameter R_p coupled with C_c, represent the processes that occur at the substrate layer (at the electrolyte/substrate layer interface). R_{ct} corresponds to the charge transfer resistance associated with the penetration of the electrolyte through the pores or pinholes that exist in the external coating and R_p is the polarization resistance at the electrolyte/substrate interface in the pores. Qc corresponds to capacitance of the coating layer and Q_s to the capacitance at the electrolyte/substrate interface, which seems to be associated with the double layer formation (124). R_s is the ohmic resistance of the electrolyte. The impedance of a constant phase element (Cc) Q is given by equation (46,124,126)

$$Q = ZC_c = (1/Y0)/ (j\omega)n$$

3.2   Experimental Process Flow

In order to evaluate the corrosion reaction in Al2219, familiarity with the material and the chromating coating process was acquired. The surface of the non-coated Al2219 substrates

was evaluated by characterizing the polished alloy surface and surface analysis using profilometry microscopy, SEM/EDS, and XPS. Emphasis was given to the understanding and the characterization of the intermetallic secondary phase particles embedded in the substrate. The chromating coating application process was performed at NASA Launch Equipment Shop (LES) and was witnessed for all samples from cleaning to drying. All coatings were applied per NASA Standard 6012 called out MIL-C-81706/MIL-DTL-5541 (51).

The process for the experimental design is listed in Table 2. Generally, there were two larger sample series: (1) "Fresh" samples that were processed immediately after chromated conversion coating was applied and (2) "Aged" samples that were processed three months after storage in doors in ambient temperature and humidity. These two larger batch samples were separated further into four sample series: (1) the control samples were the not coated bare Al2219 series, (2) the 25°C CCC treated Series were Al2219 samples that were treated with chromated conversion coating but were not subjected to heat treatment, (3) the 65°C CCC treated series were Al2219 samples that were treated with chromated conversion coating and were heat treated to about 65°C ±5°C for 16 hours, (4) the 129°C ±5°C CCC treated series were Al2219 samples that were treated with chromated conversion coating and were heat treated to about 129°C ±5°C for 16 hours. Surface analysis was conducted 20-30 minutes after the heat-treated samples cooled to room temperature in ambient lab environment. Surface characterization consisted of visual inspection, microscopy, XPS, EIS and SEM/EDS were performed on all samples prior to CCC application, immediately after CCC application, and before/after heat treatment.

Additionally, surface characterization of all samples was performed after exposure to accelerated corrosion. This surface characterization entailed visual inspection, microscopy, SEM/EDS, and profilometry before and after accelerated corrosion exposure in the salt fog chamber.

Table 2. Process flow for evaluating CCC application and heat treatment for both freshly applied coating and aged samples.

Conversion Coating	Samples	Step 1	Step 2	Step 3	Step 4	Step 5	Step 6
*Type I: Class 1A Fresh samples and three months aged samples	Control Non-coated	Surface Examination	No-Heat treatment		Salt Spray	Surface Examination	Analysis
	25°C CCC treated Series	Surface Examination	Heat treatment	Surface Examination	Salt Spray	Surface Examination	Analysis
	65°C CCC treated Series	Surface Examination	Heat treatment	Surface Examination	Salt Spray	Surface Examination	Analysis
	129°C CCC treated Series	Surface Examination	Heat treatment	Surface Examination	Salt Spray	Surface Examination	Analysis

*The "*Fresh samples*" are Al2219 panels that were CCC treated and processed immediately after coating application process.
The "*three months aged samples*" are Al2219 panels that were CCC treated, stored in a control environment to mock storage of hardware component, and were then processed after three months.

3.2.1 Materials

In collaboration with Blue Origin, Al2219-T91 bare aluminum samples were purchased from Q-Lab. Samples were 3" x 10" and 0.032 thick. The composition of the Al2219 were certified and is listed in Table 3. After conversion coating application, the samples were sectioned to 3"x3" squares to accommodate the sample holder for microscopy, profilometry, and SEM/EDS. Some sample were sectioned to 1"x3" to accommodate the sample holders for EIS and XPS.

Table 3. Chemical composition of the Al2219 (wt.%) (34)

Alloy	Al	Cu	Mg	Mn	Fe	Zn	Si	Ti	V	Zr
Al2219	Bal.	5.8-6.8	0-0.02	0.2-0.4	0-0.3	0-0.1	0-0.2	0.02-0.1	0.05-0.15	0.10-0.25

3.2.2 Corrosion Test Cell

The ParaCell™ Electrochemical Cell Kit from EG&G Princeton Applied Research (Model K0235) was used for all electrochemical experiments. The cell has two end plates for the working electrode and the counter electrode and has four port to accommodate the electrode connections. The cell body is a chemically resistant polycarbonate and all metal in the cell is 304 stainless steel that does not touch any of the electrodes except for grounding. The control (non-coated Al2219) samples in the electrochemical experiments were prepared by ultrasonic cleaning in ethyl alcohol to eliminate organic contamination. All test samples were exposed to fresh 300 mL 3.5% NaCl aqueous solution in accordance with ASTM D-1141-52, Formula A, Table 1, Section 4 Standard Practice for Preparation of Substitute Ocean Water (129). The solution was never re-used. The measurements were carried out under ambient laboratory conditions with the electrolyte at rest (no external stirring). The electrochemical cell was designed so that 0.75 cm^2 of the sample surface area

was exposed to the electrolyte. The cell used a traditional 3-electrode cell configuration as seen in Figure 23 (left). The working electrode consisted of the exposed surface area of the sample, the counter electrode was a graphite rod, and the reference utilized a standard calomel reference electrode. All components were purchased from Gamry Instruments. All testing was performed in a Faraday cage as shown in Figure 23 (right). Prior to running the electrochemical impedance spectra, the open circuit potential (OCP) of the system was monitored to ensure that the system reached steady state stability.
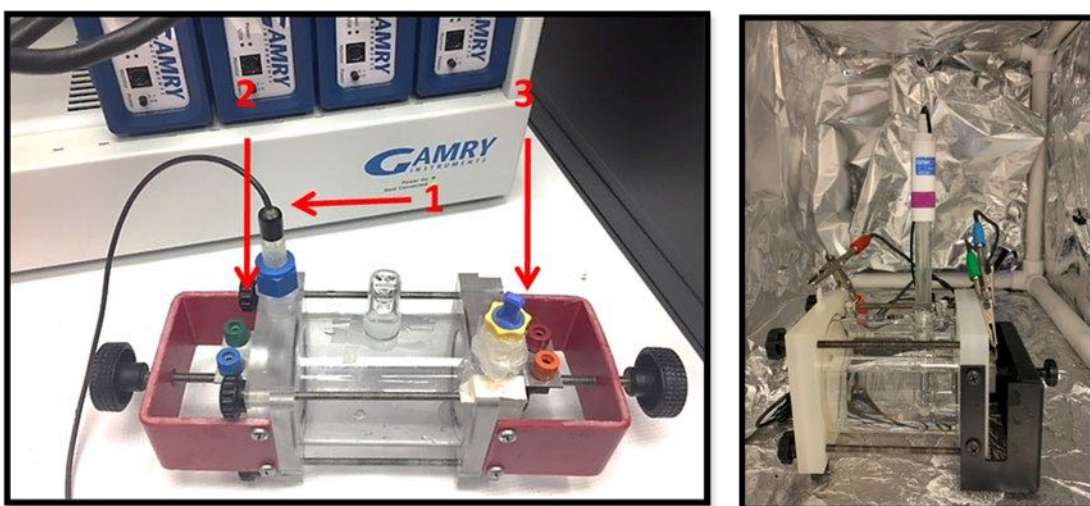
Figure 23: Photograph of the corrosion test cell used during electrochemical measurements (left) and the Faraday cage setup (right). (1) Standard calomel reference electrode, (2) Working Electrode (mounted), and (3) Counter Electrode (graphite rod).

3.2.3   Application of Chromate Conversion Coating

Chemical conversion coating on aluminum 2219 substrate was applied by NASA LES machine show which is strategically located in the heart of Kennedy Space Center and is a state of the art AS 9001 REV C Certified Manufacturing Facility specializing in a wide range of Aerospace Hardware. The LES Shop's manufacturing capabilities range in size

from small highly precise mechanisms to very large and complex assemblies weighing several tons. Completion of these projects is done through the latest concurrent manufacturing techniques utilizing the latest CADCAM and CNC Technology. Manufacturing projects from "Concept through Completion", including final assembly, paint, and testing. LES provides qualification testing for NASA's space flight hardware conversion coating line per MIL-DTL-5441F (51) and the location and tanks used during the entire process is shown is shown in Figure 24. This specification is approved for flight hardware application per NASA-STD-6012 Corrosion Protection for Space Flight Hardware. This specification covers chemical conversion coatings formed by the reaction of chemical conversion materials with the surfaces of aluminum and aluminum alloys. Type 1, Class 1A provides chromated conversion coating for maximum protection against corrosion, painted or unpainted is selected.

Test panels were provided by Blue Origin in ready-to-use condition. All panels were wrapped in paper containing a vapor-phase corrosion inhibitor to prevent scratches and oxide formation. During application, the ambient conditions were acceptable in accordance with manufactures' recommendations and ranged from:

- Ambient Temp – 74 to 84°F
- Dew Point – 67.5 to 74.6°F
- Surface Temp – 76.1 to 90°F
- Humidity – 65.5 to 89%

Prior to coating, the base metal was chemically cleaned such that a water break-free surface is obtained after rinsing. water break test is commonly the simplest and gross tests of part cleanliness.   The water break test is a simple and quick way to look for surface containments, oils, and other hydrophobic films on the substrate. The test simply immerses the panel in fresh, clean water at a vertical angle to look for complete "sheeting" or shedding of water. Formation of droplets rather than sheet is a clear indicator that oils, or other residues are present. Prior to application of the chemical conversion coating, it is imperative that samples are pristine. Contamination and oils will lead to poor coating adhesion.

The chemical conversion coating was applied non-electrolytically by immersion on the aluminum substrates. The chemical conversion coating appeared continuous in appearance and was visibly discernible in daylight. The sample were free from areas of powdery or loose coating, voids, scratches, flaws, and other defects or damages which reduce the serviceability of parts or are detrimental to the protective value and paint bonding characteristics. Samples that had mechanical scratches or non-uniform coating were not included in the final sample set as part of this thesis.

Figure 24: (a) NASA LES Machine shop chromate conversion line, (b) Al2219 samples drying after coating, and (c) chromate tank.

3.2.4 Thermal testing of CCC samples

The thermal testing was performed in air using the thermal drying and heating chamber, BINDER GmBh, Model FD 23 (Figure 25). The samples were heat treated in the chamber at the following temperatures: (a) 65°C ±5°C and (b) 129°C ±5°C for 16 hours. After heat treatment, the samples were cooled at room temperature for about 20-30 minutes before handling.

Figure 25: BINDER Drying and heating chambers with forced convection.

3.2.5   ASTM B117 Salt Spray, Salt Fog and Corrosion Testing

Per NASA-STD-6012 Corrosion Protection for Space Flight Hardware requires that coatings on flight hardware that will be (a) within 50 mile of the seacoast and in an uncontrolled humidity environment, and (b) hardware in crew compartments that will be used for single flight, or reuse after saltwater landing shall follow the following test methods (7):

- Salt Spray (Fog): the coating system shall be tested with a Salt Spray (Fog) for 168 hours in accordance with ASTM B117.

All samples (except samples for XPS and EIS) were tested in the neutral salt fog chamber in accordance with ASTM B117. The test was for 168 hours and was continuous for the entire test period.

The neutral salt spray also referred to as salt spray test is a corrosion testing method that uses high-saline environments to measure the corrosion resistance of products, paints, and coatings over extended periods. This test is conducted in a closed chamber that can be adjusted to create a variety of corrosive environments. The salt spray fog chamber is shown in Figure 26. This chamber isolates chlorides, temperature, and water vapor to accelerate corrosion reactions. The chamber continuously uses a salty fog of 3.5% NaCl at $35 \pm 2°C$ to maintain one-hundred percent RH values which allows for a constant salty moisture environment. All water used for in the salt spray test conformed to Type IV distilled water in per ASTM D1193 Standard Specification for Reagent Water (130). All test panels were placed on the polypropylene slotted support rack at 30° from the vertical parallel to the principal direction of flow of fog through the chamber as shown in Figure 26 (inset

photo). The pH range in the chamber was between 6.5 to 7.2. The panels were in this accelerated exposure environment for 168 hours (7 days) and were not allowed to contact other surfaces in the chamber or the condensate nor with each other.

Figure 26: Photograph of Q-Fog neutral salt fog chamber and inset is examples of test panels on the polypropylene slotted support rack between 15 and 30°.

After the 168-hour salt fog exposure in the Q-Fog, model CCT1100, test panels were rinsed in deionized water to remove salt deposits from the surfaces and allowed to air dry. Test panels with extraneous deposits and bulky corrosion products were subjected to a nitric acid clean for 5min and then rinsed thoroughly in deionized water. Areas within 10 mm from the edges of the panel, identification markings, and holding points were excluded from inspection and analysis as displayed in Figure 27. Differences in color between the test panels were not cause for rejection.
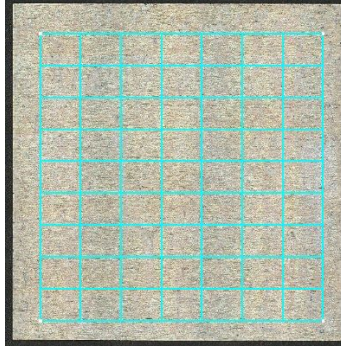
Figure 27. Example of typical sample with blue areas designating area used for analysis.

CHAPTER 4

4.0   Results

In this chapter, surface characterization and corrosion analysis of the alloy Al2219 is performed. Corrosion analysis have experienced great breakthroughs in the advance of experimental and computation instruments that allows for development of rigorous observations and faster timescales for experimentations. This research sought to advance the fundamental understanding of chromate conversion coating on aerospace aluminum and evaluate it for its specific intended environmental reactions. In attempt to doing this, the effects from the molecular intermetallic micro levels were evaluated to its effect on the larger macro scale.

Corrosion analysis of the surface of thin coating on metal substrates has historically provided irregularities due to the inconsistent nature of coating application. In this research it must be noted that, it was very common to find micro features in random sections of the sample, thus making its limited occurrence on the surface to deem the surface non-continuous. Aging of the samples is defined as samples stored at ambient temperatures in a laboratory setting for three months as this is the typical storage for flight hardware vehicles during processing. Heat treatment was performed at two elevated temperatures: a) 65°C ±5°C and (b) 129°C ±5°C for 16 hours in drying oven. The temperatures were selected because these are the typical flight hardware processing temperatures used for curing other components on the vehicle.

This research sought to combine both the fundamental understanding and the industry standard qualified testing to answer a real-world problem that will help direct NASA KSC's handling of future flight hardware components for the next generation Artemis program where the first woman and next man will launch to the moon.

4.1 Qualification of the Chromate Conversion Coating Application Process at NASA LES

Launch Equipment Support (LES) Shop services (Figure 28) provides high crew support services to enable access to flight hardware or ground support equipment, and commercial payload offloading support to NASA, Commercial Partners and Cape Canaveral Space Force Station (CCAFS). NASA-STD-6012 Corrosion Protection for Space Flight Hardware provides clear direction for the approval and use of inorganic finishes on flight hardware components. Per the standard, the requirement allows the use of inorganic finishes such as chromate conversion coatings per MIL-DTL-5541 Chemical Conversion Coatings for use as a primer base or as a temporary coating during fabrication. In accordance to MIL-DTL-5541, classification inspections and process control inspections are required for the chromate coating process line.

Figure 28: NASA KSC LES machine shop used for the application of chromate conversion coating onto Al2219 substrates.

For the verification process, chromating classification used was Type 1, Class 1A which provides chromated conversion coating for maximum protection against corrosion, painted or unpainted was selected. The verification process for Type 1, Class 1A consists of using five Al2219 panels for corrosion resistance testing. Test specimens used for process control testing were 3 inches wide, 10 inches long, with a nominal thickness of not less than 0.020-inch are shown in Figure 29. The test specimens were processed with the hardware during an actual production run, including all pre- and post-treatment processes such as cleaning and rinsing. After processing samples, the sample were allowed to dry for 24 hours and then processed in 3.5% salt spray test in accordance with ASTM-B117 for 168 hours. After exposure, test pieces were cleaned in running water, blown with clean, dry unheated air, and visually examined for corrosion resistance conformance. Conformance indicates that No more than 5 isolated spots or pits none larger than 0.031 inch in diameter, per test specimen and no more than 15 isolated spots or pits on the combined surface area of all five test specimens. Edges, identification marks and holding points during processing shall be excluded from evaluation and loss of color was not a cause for rejection.

Table 4 lists the results from the control testing of the coating process. Visual inspection showed zero (0) spots/pitting found across the surface of the samples. The LES Machine Shop passed the conformance for coating application and was used to coat all samples for this study.
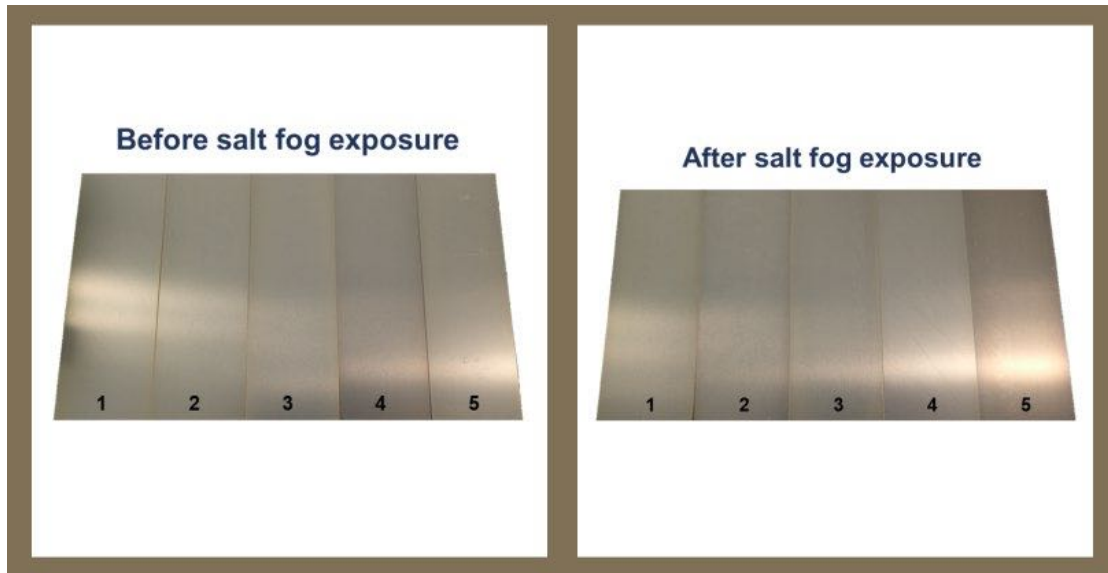
Figure 29: Photograph of CCC treated Al2219 (3"x10") samples that were processed for conformance at the LES Machine Shop (left) before and (right) after salt fog exposure.

Table 4. Evaluation of CCC coated panels for process control inspection

Panel	Pit count*	
	Al2219	Pass/Fail
1	0	Pass
2	0	Pass
3	0	Pass
4	0	Pass
5	0	Pass
Total	0	Pass

*All pit diameters smaller than 0.031"
Pass Criteria: Per MIL-DTL-5541, no more than 5 isolated pits, none larger than 31 mils diameter per specimen. No more than 15 isolated pits, none larger than 31 mils diameter, on the combined surface of 5 specimens in each set. Areas of the specimen within 0.25" from edges, ID markings, and holding points during processing shall be excluded from examination.

4.1.1   Corrosion resistance testing for coating performance conformance

Profilometry was used to confirm visual conformance of pitting across the surface. The samples were evaluated after salt fog exposure on the optical profilometer and no pitting was found. Figure 30 is an example of one sample from the sample set.
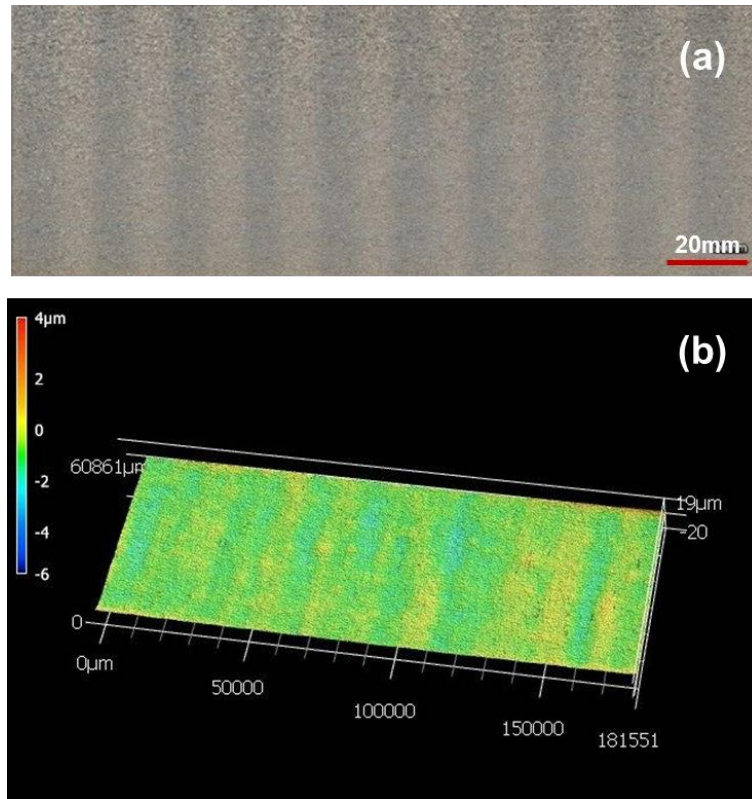
Figure 30: Profilometer images of (a) optical view and (b) 3D surface topography of CCC treated Al2219 after 168hour exposure in 3.5% neutral salt fog.

4.2 Surface Characterization of the Al2219 as received

Aluminum alloy 2219 has been widely used in aerospace applications because of its superior mechanical properties including strength-to-weight ratio, which result from alloying elements such as copper, magnesium, and manganese. However, the corrosion performance of the material can be problematic because of the addition of copper leads to the formation of various intermetallic particles that make the alloy highly susceptible to localized corrosion, especially pitting corrosion, and intergranular corrosion. Addition of copper in this alloy ranges from 5.8% to 6.8% and this far exceeds the maximum solubility of copper in aluminum. This allows two types of precipitates to form readily: (1) primary coarse precipitate of Al_2Cu, and (2) secondary fine particles of Al_2Cu. These intermetallic

precipitates can act as crack initiations points due to the large stress concentrations that are induced at the coarse particles during deformation, thereby reducing the corrosion resistance of the alloy (20,131).

To ensure corrosion protection, Al2219 are usually coated with a chemical conversion coating layer. The only chemical conversion coating that meets the stringent requirements of NASA standards are chromated conversion coating (CCC) outlined in military specifications MIL-C-81706/MILDTL-5541 (51)). Chromate conversion coatings have been employed in the surface finishing process for AA2219 and other metal alloys due to their excellent ability to resist localized corrosion and to promote paint adhesion for a long time [(132–135)]. The coating is formed via a reduction process where chromate ions are reduced and produces Cr_2O_3. The hydrated Cr_2O_3 forms a protective barrier to through the production of residual chromate ions that are corrosion inhibitors (136).

In this chapter, CCC was applied to Al2219-T87 and was characterized by various analytical techniques (Table 5), namely Scanning Electron Microscopy (SEM) and Energy Dispersive X-ray Spectroscopy (EDS), X-ray Photoelectron Spectroscopy (XPS), Optical Profilometer, Linear polarization resistance, and electrochemical impedance spectroscopy (EIS), to understand the coating morphology and corrosion behavior of chromated Al2219. In order to monitor the chemical responses and the corrosion reactions of the CCC treated aluminum alloy, the non-coated bare aluminum substrate and non-heated CCC samples were characterized for comparison. After treating the aluminum alloy with CCC, the samples were subjected to two different elevated temperatures and analyzed to assess any

relevant chemical and surface variation as a function of temperature. This will provide comparative data to understanding the effects of heating and aging on the degradation and chemistry of chromium in the coating of Al2219. Figure 31 provides an image of an as received aluminum sample compared to a CCC treated aluminum sample.

Table 5. Tests performed on Al2219 samples.

	Non-coated	CCC application	After heat treatment	After Salt spray
Surface profilometry	-	-	-	x
XPS	x	x	x	-
Electrochemical analysis	x	x	x	-
SEM/EDS	x	x	x	x
Neutral Salt spray	x	x	x	-
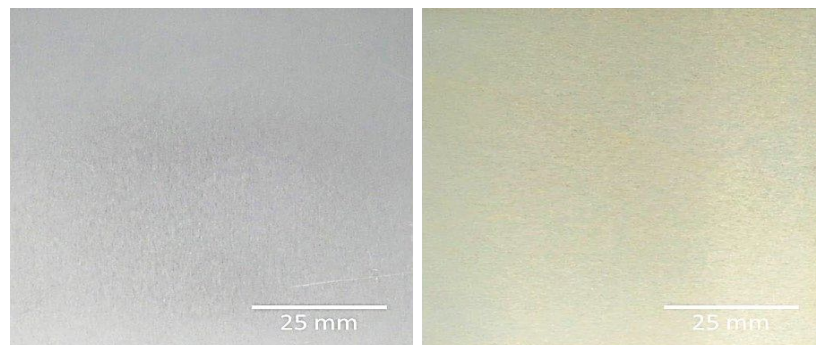
Figure 31: Images showing the typical surface of the aluminum alloy 2219 (left) non-coated (right) and after CCC treatment.

Evaluation and Surface characterization of the non-coated Al2219 alloy

The surface of the non-coated Al2219-T87 sample coupons was analyzed by optical microscopy, SEM/EDS, and XPS. Aluminum alloy 2219 has been widely used in aerospace applications because of its superior mechanical properties including strength-to-weight ratio, and its composition is listed in Table 6. To achieve the T87 temper, the alloy is solution heat-treated, strain hardened by 1%, then artificially aged to achieve precipitation hardening (32,137). This gives the alloy one of the highest strengths compared to other tempered 2219 alloys.

Table 6. Chemical composition of the Al2219 (wt.%) (34)

Alloy	Al	Cu	Mg	Mn	Fe	Zn	Si	Ti	V	Zr
Al2219	Bal.	5.8-6.8	0-0.02	0.2-0.4	0-0.3	0-0.1	0-0.2	0.02-0.1	0.05-0.15	0.10-0.25

Sample coupons Al2219 of about 50x50 mm each were wet ground with 600, 1200, 2500 and 4000 grit silicon carbide papers, and then were polished with diamond solution to 1 μm finish. The samples were ultrasonically cleaned in isopropanol and rinsed in deionized water. The beam energy of 15-20 kV was used for the acquisition of SEM spectra and EDS elemental maps and 1486.6 eV for XPS. Thermo Avantage data systems were used for the acquisition and processing of XPS data and Oxford Ultim max was used for EDS. For XPS, the survey spectra provide kinetic energy values for the Auger peaks. This data provides more of a semi-quantitative understanding of the surface due to the low energy

resolution of a survey spectrum and the broad shape of the Auger peaks. The aluminum, oxygen, and chromium peaks along with the shape of the peak will distinguish the metal state from the

4.2.1 Optical Microscopy - Visual inspection

Metallurgical Microscope (Olympus Inverted Metallograph GX71F5) was used to illustrate the surface of the non-coated Al2219. The surface of the sample has a predominant aluminum matrix with intermetallic particles with a mean size ranging from ~1µm to 10 µm. These intermetallics are a known feature for Al-Cu alloy 2219 and is described by several authors (138–145). Figure 32 shows the fine and coarse particles on the surface using brightfield and differential interference contrast (DIC) imaging techniques.
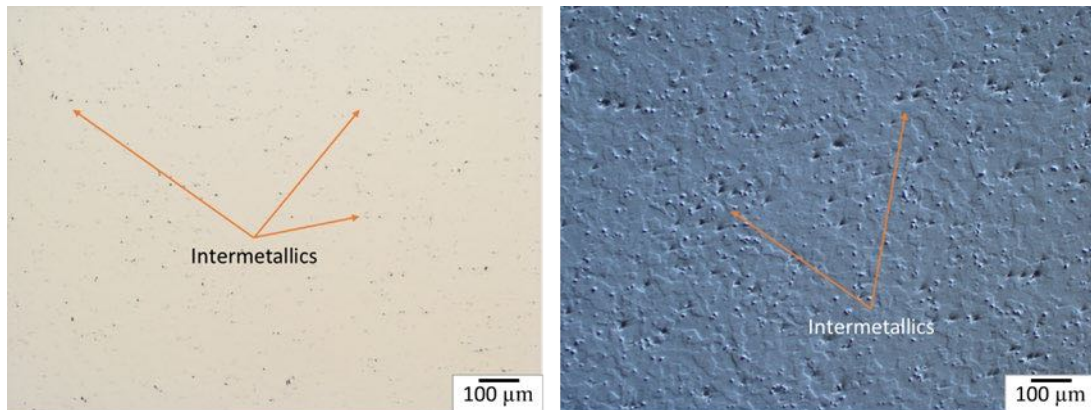
Figure 32: Images of intermetallic particles on the surface of Al2219 sample after surface polishing (a) Brightfield (100x) and (b) high contrast DIC (100x).

4.2.2 SEM/EDS of non-coated Al2219

SEM with backscattered-electron (BSE) imaging provided a clear visual examination of the surface of the Al2219 alloy. Since the copper atoms have a higher atomic mass than aluminum, these atoms scatter more electrons back towards the detector than the lighter aluminum atoms and consequently appear brighter in the SEM image. Particles of various sizes, ranging from 200 nm to 10 µm were found across the surface of the non-coated samples (Figure 33).

The major phase precipitates in Al2219 alloy is copper and the regions in these phases are generally said to be cathodic in respect to the aluminum matrix (145–150). Several groups have found that the cathodic copper S phase sites tend to be initiation sites for pitting (114,151–158). The electron SEM image of the coating surface is shown in Figure 34. The image shows the presence of porosity on the polished surface along with defects "holes" in the surface either from polishing or from the copper precipitates.
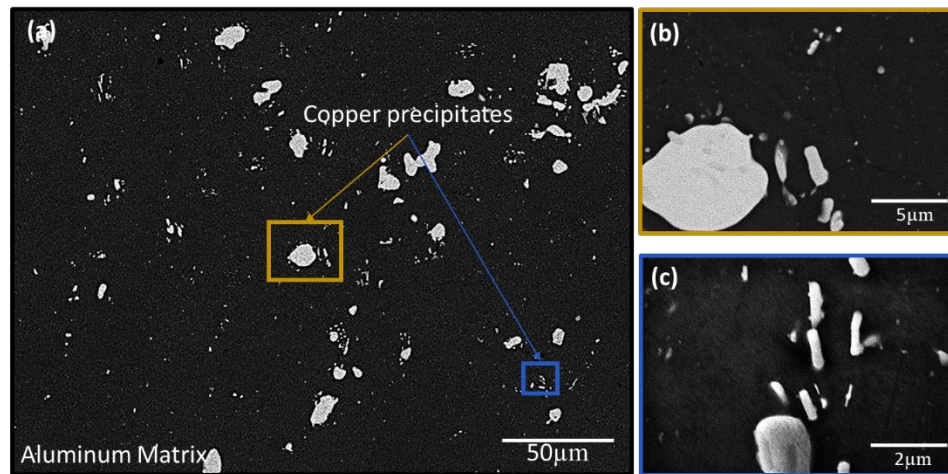
Figure 33: SEM backscattered image of a polished surface of the Al2219 alloy denoting the (a) aluminum matrix containing copper phase, 1kx, (b) spherical copper precipitates, 10kx, and (c) longitudinal copper precipitates, 30kx.

EDS point analysis was performed on the intermetallic particles and its surrounding region. As seen in Figure 35, the EDS point analysis and mapping confirmed that the lighter contrast particles were from copper (Cu Kα/Lα) peaks. The darker contrast regions had a high intensity of aluminum (Al Kα) and oxygen (O Kα) peaks. Additionally, the aluminum matrix contains needle like copper precipitates that are referred to as secondary fine particles (Figure 34). These are the strengthening precipitates of Al_2Cu, and their presence is expected in the T87 tempers (32,159,160).

Figure 35 shows a magnification of the particles in the aluminum matrix along with an EDS comparative summary of the elemental composition of these two features. The point analysis of the average weight % composition of the intermetallic particles was 43.5% Al, 52.4% Cu. The aluminum matrix had an average point analysis weight % composition of 59.8% Al, 24.5% Cu, 8.4% Fe, and 2.5% Mn. The EDS point analysis map confirmed a high intensity of both Al and Cu over the intermetallic surface, indicating the particle to be comprised of a single Al-Cu phase.
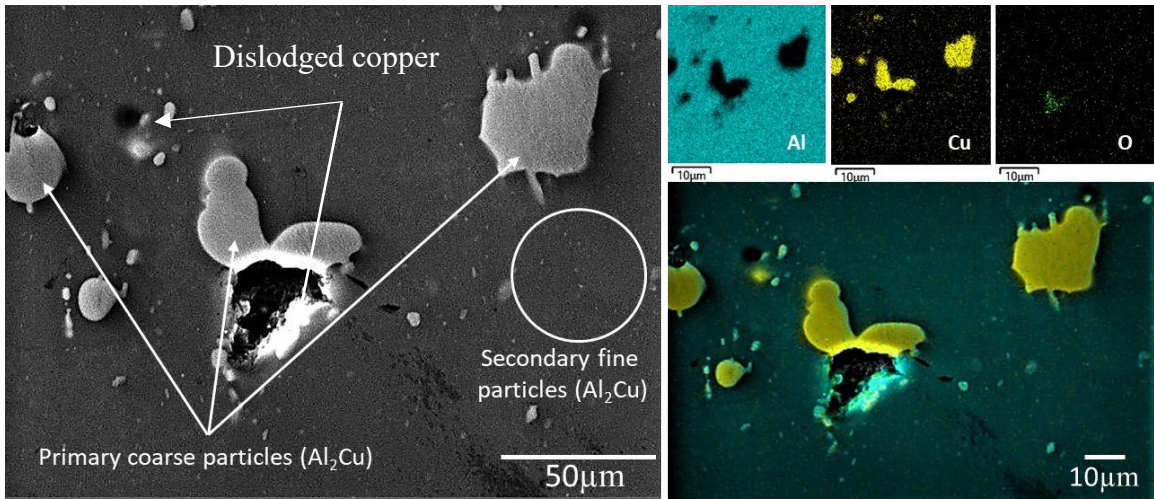
Figure 34: (Left) SEM backscattered image of the polished surface of Al2219 alloy denoting the primary coarse particles and secondary fine particles (Al2Cu), 5kx. (Right) EDS mapping and overlay of the aluminum matrix indicating the regions with the intermetallic particles.
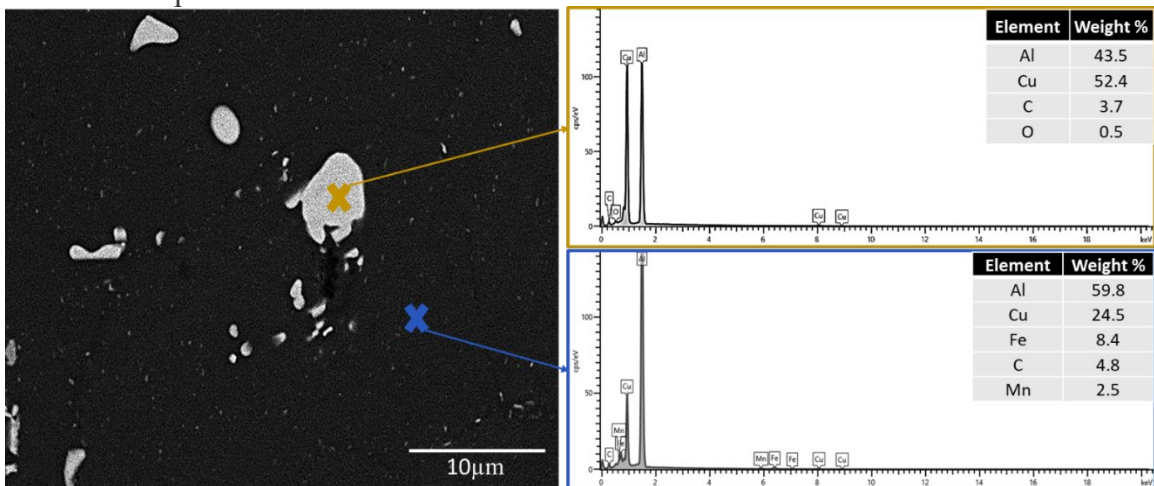
Figure 35: SEM image (5kx) of a polished Al2219 and EDS point analysis of areas of intermetallic secondary phase particles on the surface of the alloy and of the general aluminum matrix.

Summary of Surface characterization of non-coated Al2219

The first stage of the coating process was examined. A better understanding of the alloy

surfaces relevant to aerospace industry was obtained revealing the wide presence of second

phase precipitates with variable dimension and composition. The application of chromate

conversion coating and the effect of temperature and aging of the coating will be evaluated

in the upcoming chapters.

4.3 Surface Characterization of Chromate Conversion Coatings as a function of heat treatment and aging

The aluminum test samples were treated with chromated conversion coating by NASA

Launch Exploration Shop (LES) as previously described in Chapter 3. After CCC

treatment, a set of samples were evaluated immediately and are referred to as "fresh" CCC

treated samples. Another set of samples were CCC treated in tandem and then were stored

in an indoor ambient environment to mock Orion vehicle storage for three months and are

referred to as "aged" CCC treated samples. The process flow for the evaluation of both

sets of samples are listed in Table 7. Overall, after CCC treatment, the samples were heat

treated and then underwent corrosion exposure in the Neutral Salt Fog chamber. Surface

characterization was performed before and after each processing step. Visual inspection

was performed immediately after receiving the coated samples and after heat treatments.

The coating appeared uniform and there were no signs of delamination throughout the

process flow. Pictures of all samples were taken and examples from the batch of samples

are displayed in Figure 36. There were slight variations in color of the coated samples as it

is extremely difficult to obtain exact shade with chromate conversion coatings even within the same batch (51,161).

Table 7. Process flow for evaluating CCC application and heat treatment.

Conversion Coating	Samples	Step 1	Step 2	Step 3	Step 4	Step 5	Step 6
*Type I: Class 1A Fresh samples and three months aged samples	Control Non-coated	Surface Examination	No-Heat treatment		Salt Spray	Surface Examination	Analysis
	25°C CCC treated Series	Surface Examination	Heat treatment	Surface Examination	Salt Spray	Surface Examination	Analysis
	65°C CCC treated Series	Surface Examination	Heat treatment	Surface Examination	Salt Spray	Surface Examination	Analysis
	129°C CCC treated Series	Surface Examination	Heat treatment	Surface Examination	Salt Spray	Surface Examination	Analysis

*The "Fresh samples" are Al2219 panels that were CCC treated and processed immediately after coating application process.
The "three months aged samples" are Al2219 panels that were CCC treated, stored in a control environment to mock storage of hardware component, and were then processed after three months.

4.3.1 Visual inspection as a function of heat treatment

Samples were CCC treated as a function of heat treatment and evaluated immediately after drying. Figure 36 shows a snapshot visual representation of the surface of the samples prior to heating and after heat treatment at elevated temperatures 65°C and 129°C. Prior to heating, the surface of all samples had the iridescent gold appearance which is the inherent color of hexavalent chromium on aluminum. The same iridescent gold color feature was seen after the samples were heat treated to 65°C. However, the samples that were heat treated at 129°C had a translucent tint gold appearance. The iridescent gold

appearance was not as profound as the other series of samples. According to ASTM B449 (161), the classification system for the appearance of chromate coatings indicates that the colorless to yellow appearance of the coating should still provide some corrosion resistance. Ultimately, samples that had blatant mechanical scratches and defects not consistent with the overall mechanical and physical appearance of the sample set were eliminated from testing. All samples that went through the heat treatment process were not eliminated for lack of yellow/gold color. Generally, all the samples heat treated to 129°C were consistently translucent gold in appearance and was deemed a characteristic feature of heating to this temperature.
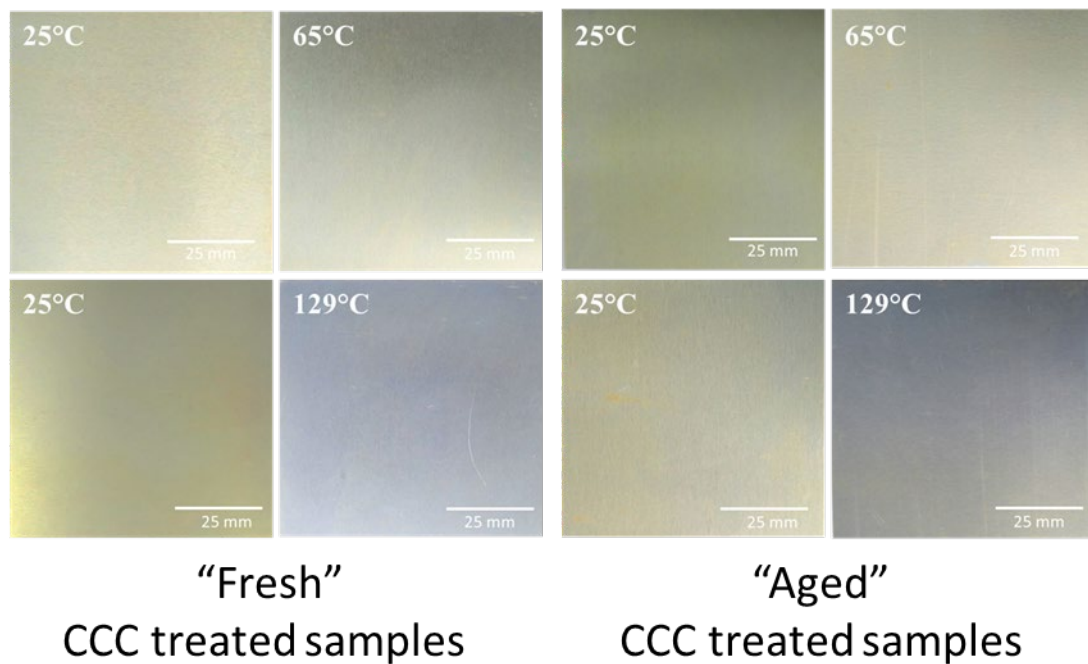
Figure 36: Images of the freshly applied and three-month aged surface of Al2219 after CCC treatment with no-heat applied represented at 25°C and after heat treatment at 65°C and 129°C.

4.3.2 SEM/EDS of the CCC treated surface of Al2219 and intermetallics as a function of heat treatment and aging

Energy dispersive x-ray spectroscopy (EDS) associated with a scanning electron microscope (SEM) is the most common technique used to obtain chemical identification of corrosion products. EDS can detect elements C through U with a detectability limit of about 0.1 weight %. The scanned electron beam interacts with the specimen's surface, which produces secondary and back-scattered electrons and x-rays. These x-rays are characteristic for the element that emits them and can be used to identify the elemental composition of corrosion products. The current analysis produced semi-quantitative analysis using the Oxford Instruments Aztec 4.31 HF1 ULTIM MAX software. While the exact composition of the corrosion product will not be concluded as part of this study, information regarding which metals are present was derived along with a general concentration of the metals that are present. A relatively modest beam current was used to produce a high-count rate and facilitate rapid element mapping. However, the interaction between the current and the surface corrosion product causes charging. This can produce images that have blurriness, streaks, and bright areas on the images. The analysis provides a high-resolution analysis of the surface, and so to reduce the charging the surface of all samples were cleaned, and majority of the surface corrosion product was removed before analysis. Carbon contamination is well known to be more prevalent on high energy surfaces and it was noted that there was higher concentration of carbon on the conversion coating rather than in the cracks.

However, to better monitor the surface distribution of the conversion coating, carbon was removed from the EDS analysis. EDS analysis was focused primarily on the intermetallic and overall surface changes, appearance of mud-cracking, and areas of concentration for the aluminum, oxygen, copper, and chromium elements.

Figure 37 displays the SEM/EDS images of the non-coated aluminum alloy along with the CCC freshly treated, and aged CCC treated aluminum alloy. The EDS maps on the bottom of each SEM image displays the key elements of interest. Aluminum (Al Kα) had a high intensity consistently across the surface of the untreated and CCC treated alloy except in the areas that contained intermetallics copper (Cu Kα) precipitates as discussed in Chapter 2. Despite the occurrence of the copper precipitates, the chromium (Cr Kα) intensity appears uniform across the surface of the CCC treated sample confirming that coating coverage is uniform across the intermetallics.
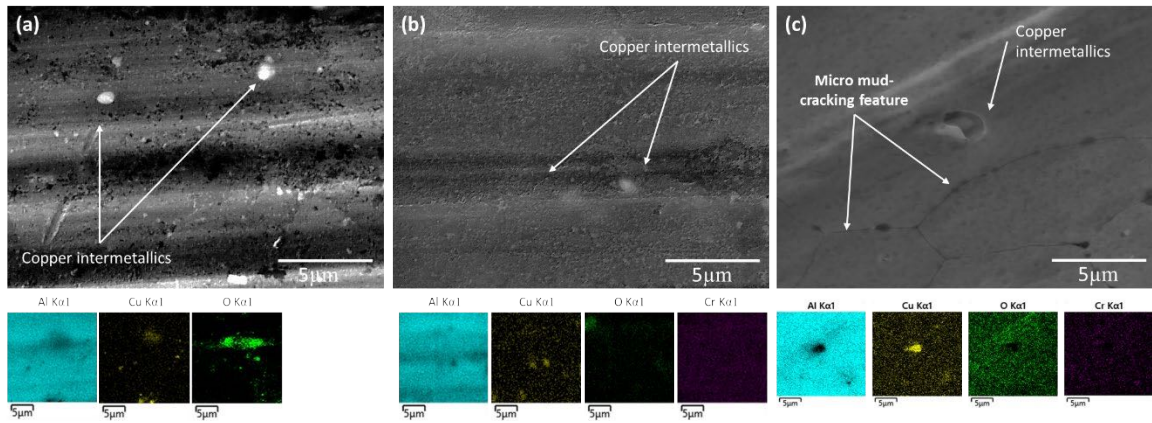
Figure 37: SEM/EDS images (10kx) of the Al2219 alloy (a) non-coated, (b) fresh CCC application at room temperature, and (c) aged CCC at 65°C.

SEM observations of the CCC treated samples that were evaluated immediately after coating application and after heat treatment at 65°C and 129°C all had a uniformed surface

appearance. These samples had very little to no surface defects and the mud-cracking morphology was not observed in the areas analyzed. Secondary phase intermetallics (Al_2Cu) from the bulk aluminum alloy was confirmed by chemical analysis using the SEM/EDS on both the non-coated and CCC treated samples. On wider magnification views, material defects in the form of holes can be seen on the surface and that can be attributed to the mechanical removal of the secondary phases during material processing, or selective leaching of secondary phases by the cleaning agents in the conversion coating.

SEM observation of the CCC treated samples that were aged and after heat treatment at 65°C and 129°C were evaluated. The mud-cracking morphology that is described by numerous authors were not observed in the samples prior to heating (55,73,86,103,139,162–164). After heat treatment of the samples at both the Aged sample series that were heat treated to 65°C and 129°C showed initiation of micro-mud-cracking. Mud-cracking was not observed in the aged sample series that was not heat treated. The mud-cracking feature is linked to rapid corrosion of the alloy due to the dehydration of the film. As the film dehydrates, cracking in the film occurs and these cracks provide access to the unprotected aluminum surface. Due to this phenomenon both the coating drying temperature and the service environment temperatures are limited to 65°C (7,165). For the sample sets that were aged, it was expected to find mud-cracking morphology before heat treatment and after heat treatment, however this was not the case. For the sample sets that were fresh CCC treated, the mud-cracking feature was not observed prior to heat treatment nor after heat treatment.

Figure 38 shows representative examples of EDS point analysis mapping of the

aluminum matrix and the copper for the fresh coated samples and the aged samples after

heat treatment at 129°C. EDS mapping confirms chromium (Cr Kα) consistently across

the surface. Additionally, EDS point analysis confirms the intermetallics as well. Semi-

qualitatively, the EDS spectrums indicated that the intensity of oxygen decreased after

heating which is linked to the dehydration of the surface due to age and heating.

Figure 39 shows an overall qualitative EDS survey summary comparison of CCC treated

Al2219 by aging and heat treatment. Overall, oxygen decreased with aging and after heat

treatment. After salt fog exposure, the 129°C series had a high a high oxygen increase

and the other samples remained about the same. There were no significant changes in

copper and chromium composition throughout processing for the no-heat and 65°C

samples. The chromium composition of the 129°C series overall remained about the

same throughout processing. However, there were several areas of interest where point

analysis of coating degradation on the surface of the 129°C series showed no visible

signs of chromium.
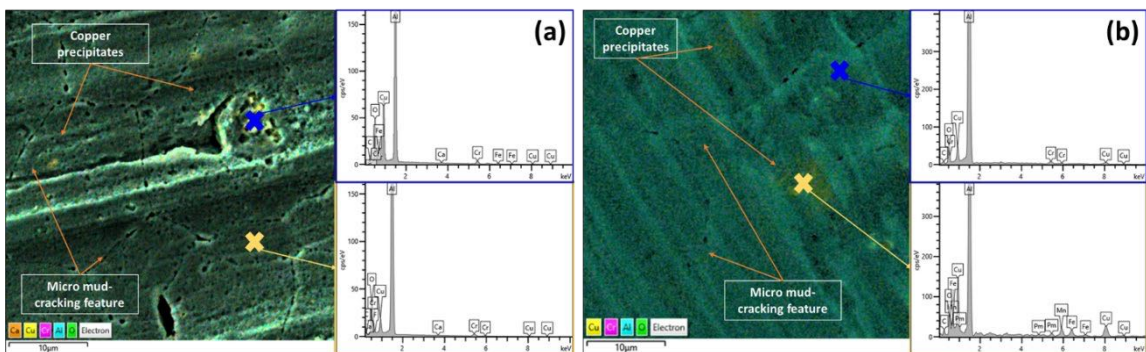
Figure 38: EDS mapping and spectrum of (a) fresh and (b) aged CCC Al2219 surface
after 129°C heat treatment (5000x). The micro-mud cracking feature is also depicted.
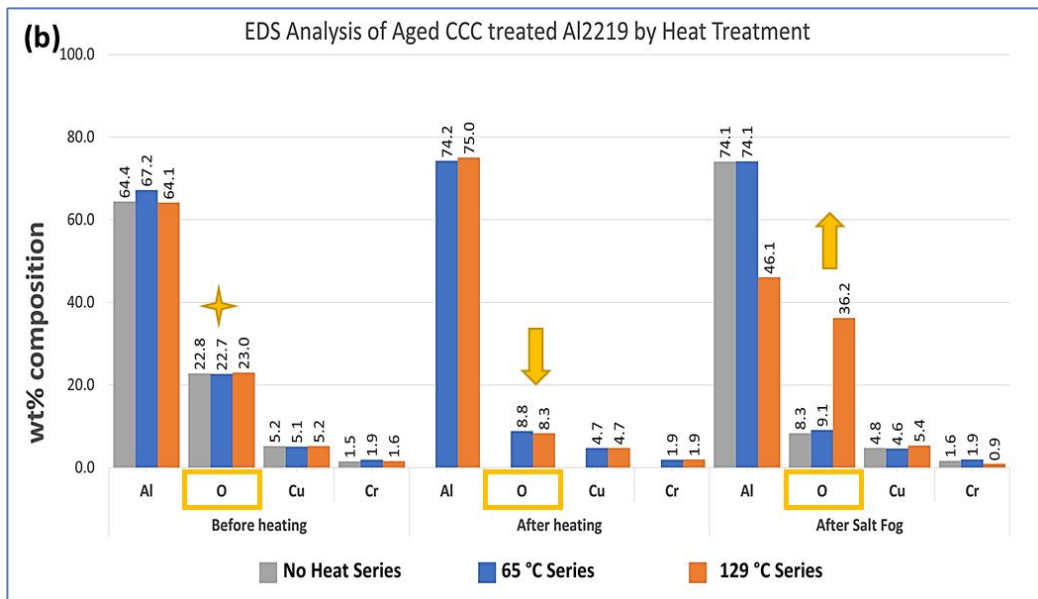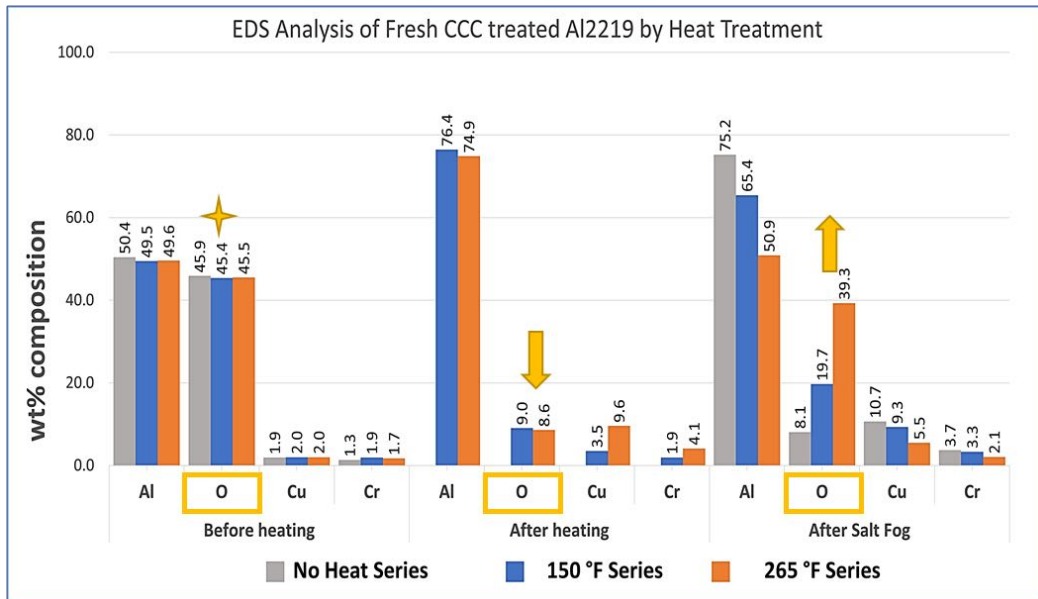
Figure 39: Qualitative EDS analysis of (a) fresh and (b) aged CCC treated Al2219 surface before, after heat treatment, and after neutral salt fog exposure (elemental composition in weight percentage). Oxygen decreases after heat treatment significantly and increases after salt-fog exposure.

Summary of SEM/EDS Surface Characterization of the Chromate Conversion Coatings as a function of heat treatment and aging:

Surface morphology observations by SEM/EDS demonstrated initiation of micro-mud-crack pattern for the surface of the aged CCC treated Al2219 alloy but not for the fresh CCC treated Al2219 alloy. Despite heating to elevated temperatures, the fresh CCC samples did not demonstrate the mud-crack feature. SEM/EDS confirmed a uniform CCC across the surface of all the samples with the consistent chromium (Cr Kα) peak. Dehydration of the coating was indicated by the decrease in oxygen (O Kα) peak intensity. This decrease in oxygen was observed in both the fresh and aged CCC treated samples that were heat treated. There was also an overall decrease in oxygen after aging the samples. Chromated conversion coating is generally understood to be a hydrated film. Aging and heat treatment causes dehydration across the surface where water molecules are lost.

4.3.3   XPS - surface and intermetallic characterization

X-ray photoelectron spectroscopy (XPS) can provide information on the outer atomic layers which provides identification of compounds using energy shifts due to changes in the chemical structure of the sample atoms. The binding energy of elements present on the surface provides a direct correlation to the chemical state of the element. For example, an oxide exhibits a different spectrum than a pure element. Chemical compounds or elements are identified by the location of energy peaks on the undifferentiated XPS spectrum. These techniques are extremely useful for analyzing thin protective scales, multi-layer deposits and sub-surface diffusion into the base metal.

Due to size constraints of the XPS, a separate set of coupons were used for surface characterization. Baseline samples were evaluated to determine the baseline chemical states of the bare aluminum alloy and the non-heat-treated conversion coating. This chapter will characterize the surface of (a) non-coated Al2219 alloy, (b) CCC treated Al2219 at room temperature (25 ±5°C), (c) CCC treated samples that were heat treated for 16 hours at 65°C ±5°C and 129°C ±5°C for 16hours. Specimens were prepared for analysis by XPS using the same processes outlined in Chapter 3. Briefly, XPS measurements were performed on a Thermo K-alpha spectrometer equipped with a micro focused monochromated radiation (Al Kα, 1486.6 eV, micro spot was 400 μm diameter) operating under 1.10^{-7} Pa with the X-ray power at 72 W.

Samples were treated with chromated conversion coating per MIL-C-81706/MIL-DTL-5541 Chemical Conversion Coatings (51). The non-coated alloy was cleaned and polished prior to analysis. Surface characterization of the coated samples was performed at two-time intervals: (a) immediately after coating application and (b) after the coating aged for three months. The sample set of coupons that underwent heat treatment were exposed to heated conditions at two heat treatment temperatures (1) 65°C ±5°C and (2) 129°C ±5°C for 16 hours prior to analysis.

XPS was used to determine the chemical states of the metal and oxide components in the coupons (a) prior to heat treatment, (b) after heat treatments, and (c) aged surface iterations of the heat treatment. All collected spectra in the XPS were calibrated to the C1s peak at 284.6eV (98).

4.3.3.1 Al2219 before and after CCC treatment

XPS analysis of the untreated (non-coated) aluminum alloy sample had the following

photoelectron peaks: O1s, C1s, Al2p, Mg1s, Ca2p, Cu2p3, N1s, Fe2p, and Zn2p. The

survey spectrum for the CCC treated aluminum alloy samples had the following

photoelectron peaks: Cr2p, O1s, C1s, Ca2p, Al2p, N1s, Na1s, Mg1s, Cu2p3, N1s, Fe2p,

and Zn2p. The CCC treated samples were evaluated after fresh CCC application.

Figure 40 shows the survey spectrum for both the untreated (a) and (b) CCC treated

samples with a summary Table 8 indicating peak binding energy, full width at half

maximum (FWHM), and atomic % of corresponding elements from the spectrum.

XPS surface analysis was performed and showed clear differences between the untreated

(non-coated) and treated (CCC coated) Al2219 samples and is denoted in the Figure 41.

Elements of interest that were chosen to evaluate differences in the non-coated vs the

coated samples were: aluminum, copper, and chromium. The high resolution XPS

spectrum of Al2219 curve fitting of Al2p, Cu2p, Cr2p before and after CCC application

are shown in Figure 42. Although the non-coated aluminum sample was polished and

cleaned, oxides were found on the surface of the sample as seen in Figure 43. Aluminum

oxide (Al_2O_3) forms naturally and quickly on the surface of aluminum alloys as a thin

passivation layer (166,167). The aluminum peak indicated in the high-resolution spectrum

shows two chemical states: Al(III) and Al(0). The Al(III) is from the outer passivation layer

of the sample, which covers the metal alloy. Additionally, the copper peak is also present

as copper oxide (CuO) as part of the weak Cu(I) satellite peaks.

XPS Spectrums display that after CCC application, the oxide regions reduced while the metal regions increased and shifted. For example, prior to CCC application, the aluminum oxide peak was sharp with a small shoulder at 75 eV for the aluminum metal. After CCC application, the oxide had a small shoulder peak. As for the copper region, prior to CCC coating, the Cu(I) peak along with its oxide were observed and conformed to the standard (168). After CCC application, the Cu(II) peak at about 960 eV was seen which was not present in the untreated aluminum sample.

The high resolution XPS Cr2p spectrum of CCC treated samples shows peaks at 577.2 eV (for Cr2p3) and 586.2 eV (for Cr2p1) are show in Figure 44. Both peaks fall within the standard spectrum peaks for Cr_2O_3 (168). This confirms the presence of chromium on the sample surface which was predominantly as Cr(III) species. This was confirmed with the deconvoluted spectra for Cr(III) and Cr(VI) standards. A deconvoluted peak at 578.6 eV indicates the minor presence of Cr(VI) which has a similar binding energy to the Cr2p3 peak of Cr_2O_3 (Cr(VI)) standard. $Cr(OH)_3$ species at 577.2 eV could also be present on the surface.

All the binding energy peaks agree well with those reported (169–175) and confirm the formation of the chromium-based conversion coating on the surface of the Al2219 substrate. Figure 45 shows the XPS fit overlay of the survey spectrum for untreated and CCC treated aluminum alloy. Chemical state changes in the elements of interest (aluminum, copper, and chromium) were observed. The XPS fit overlay of the copper peaks shows a broad, strong Cu(II) satellite peak at about 959 eV and a reduction in copper

oxide. The chromium peak was observed after coating and was not present in the untreated alloy. High resolution scans of the chromium peaks correspond to oxides and the shape of the chromium indicates that two chemical states are present: Cr(II) and Cr(VI), which confirm the protective layer. Figure 46 shows the two Cr peaks corresponding to energy range of 568 to 593 eV, for the Cr $2p_{1/2}$ and Cr $2p_{3/2}$ electron configurations. According to the chemical state fit of the chromium peak binding energies and widths, chromium appears to be present in the trivalent state as Cr_2O_3 and $Cr(OH)_3$ (173,174). The area under the deconvoluted peaks indicate that Cr_2O_3 was much higher than the $Cr(OH)_3$ (98,170,172,174). Aluminum oxide significantly reduced as the oxide peak showed less count for the aluminum oxide peak and the aluminum metal shoulder shifted more toward the metal at about 74 eV. These attributes confirm CCC coating covered the surface of the samples and metal oxides were reduced.
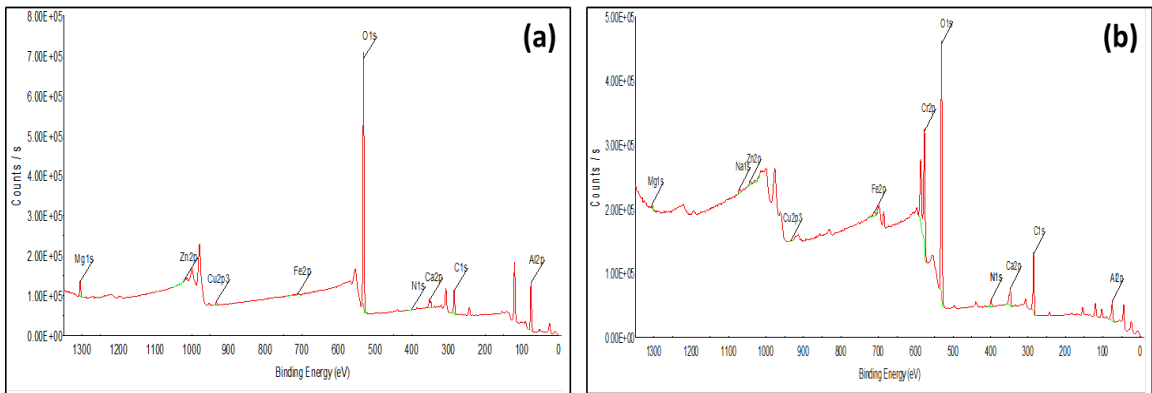
Figure 40: XPS Survey spectrum and data table of chemical composition peak binding energy for (a) untreated/non-coated Al2219 surface after polishing and (b) CCC treated Al2219 alloy with no-heat treatment.

Table 8 XPS Survey summary of non-coated and CCC treated Al2219.

XPS Survey of untreated/non-coated Al2219 alloy				XPS Survey of CCC treated Al2219 alloy with no-heat treatment			
Name	Peak BE	FWHM eV	Atomic %	Name	Peak BE	FWHM eV	Atomic %
Al2p	75.13	3.34	11.22	Al2p	74.40	2.67	0.72
C1s	284.85	3.34	3.78	C1s	284.96	3.01	16.87
Ca2p	351.89	4.02	0.40	Ca2p	347.50	1.97	0.27
Cu2p3	933.67	1.82	0.05	Cr2p	577.84	4.25	1.09
Fe2p	710.90	7.34	0.06	Cu2p3	933.94	0.08	0.00
Mg1s	1304.89	3.15	0.50	Fe2p	711.26	4.71	0.07
N1s	399.92	2.69	0.09	Mg1s	1304.83	0.98	0.02
O1s	531.93	3.27	14.96	N1s	399.82	3.62	0.88
Zn2p	1021.19	1.85	0.02	Na1s	1070.72	0.49	0.02
				O1s	531.44	3.49	11.81
				Zn2p	1031.55	3.07	0.08

(a)

(b)

(c)

(d)
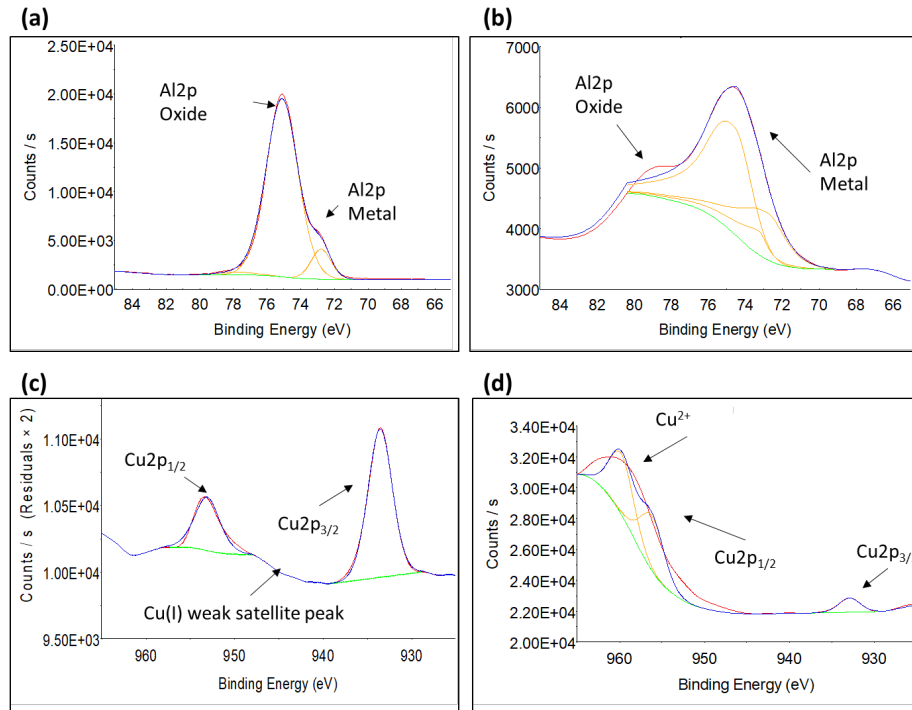
Figure 41: High resolution XPS spectrum of Al2219 curve fitting of Al2p (top) and Cu2p (bottom) indicating the metal and oxide regions: (a) Al2p untreated, (b) Al2p CCC treated alloy, (c) Cu2p untreated, and (d) Cu2p CCC treated alloy.
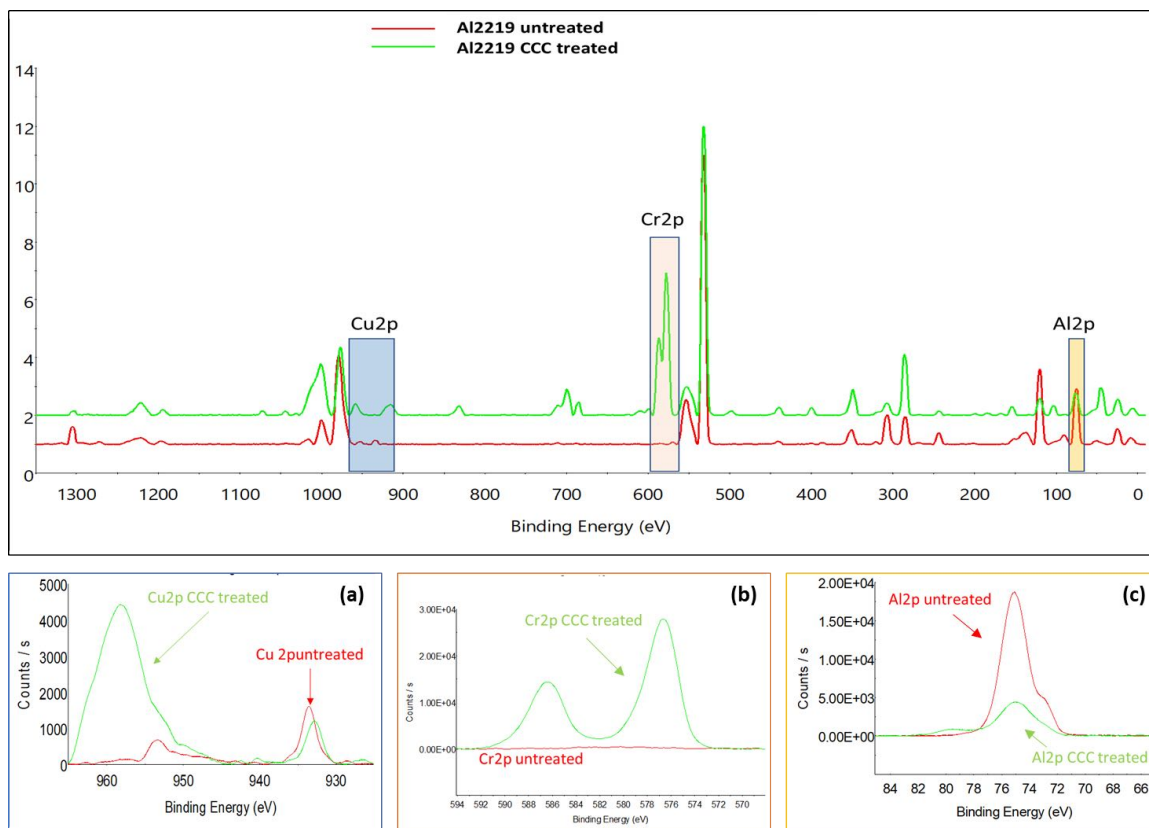
Figure 42: XPS overlays of the (top) survey spectrum for untreated and CCC treated Al229 alloy. High resolution XPS spectrum of overlays of the chemical states of key elements for the untreated and CCC treated surface: (a) Cu2p, (b) Cr2p, and (c) Al2p.

4.3.3.2 Al2219 CCC treatment as a function of heat treatment

Figure 43 provides a comparative XPS spectrum summary of the CCC coated samples that were heat treated to 65°C and 129°C to the samples that were processed at room temperature (25°C). The data tables for the XPS survey listing the photoelectron peaks for these three sample iterations are listed in Table 9.

Much like the room temperature CCC treated samples, in the high-resolution spectra for aluminum in the heat-treated samples there was a small Al2p oxide peak at about 79 eV

and a sharper aluminum metal peak at about 74 eV. The satellite chromium peak at about 587 eV is consistent with the Cr_2O_3 chemical state when preceding $Cr2p_{3/2}$ peak at 576 eV. This was a consistent feature of the chromium peak in all the CCC treated samples despite heat treatment. Despite heat treatment, all samples had the $Cu2p_{3/2}$ peak and the $Cu2p_{1/2}$ peak. The room temperature samples had an observable weak satellite peak at about 942 eV along with the $Cu2p_{3/2}$ peak at 933 eV which is indicative of copper (II) oxide. The $Cu2p_{1/2}$ peak for the copper metal was much weaker. Whereas, the heat-treated samples had a weak $Cu2p_{3/2}$ peak at about 934 eV. The $Cu2p_{1/2}$ peak and the Cu^{2+} peak appeared as one broad peak in the range 950-962 eV. This broad peak is indicative of surface copper metal. This feature was not apparent in the non-coated aluminum alloy (168). The presence of the Al2p aluminum oxide peak shows that the coating layer is either not uniform on the substrate, or that the chromate layer is not very thick. Overall, comparison of the surface of the samples varied in copper and aluminum oxide concentrations. Aluminum oxide and copper increased as a function of temperature.

Figure 43: XPS overlays of the (top) survey spectrum for heat treated CCC Al2219 alloy. High resolution XPS spectrum of overlays of the chemical states of key elements for the CCC/heat treated surface: (a) Cu2p, (b) Cr2p, and (c) Al2p.
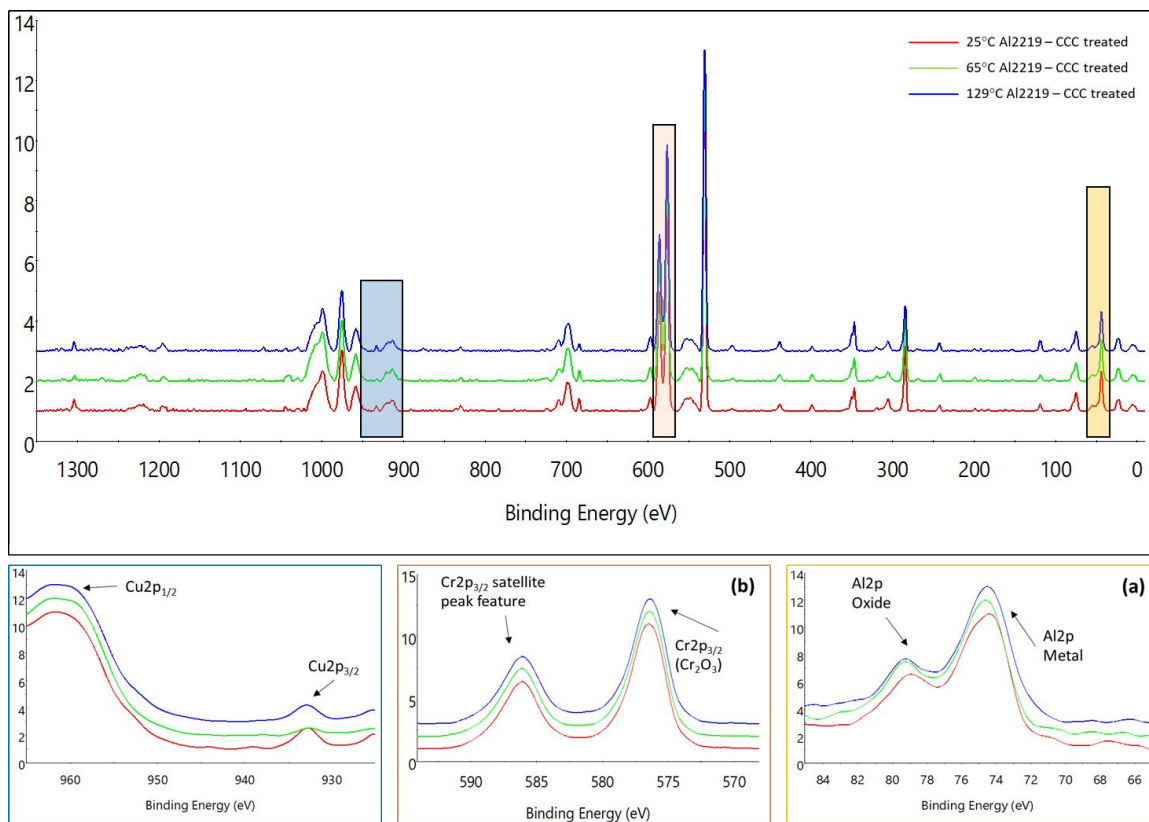
Table 9. XPS Surface composition for CCC treated AA 2219 at room temperature, 65°C, and 129°C.

XPS Survey of CCC treated Al2219 alloy at room temperature (25°C)				XPS Survey of CCC treated Al2219 alloy with 65°C heat treatment				XPS Survey of CCC treated Al2219 alloy with 129°C heat treatment			
Name	Peak BE	FWHM eV	Atomic %	Name	Peak BE	FWHM eV	Atomic %	Name	Peak BE	FWHM eV	Atomic %
Al2p	74.40	2.67	0.72	Al2p	73.71	3.14	0.48	Al2p	73.81	3.04	0.52
C1s	284.96	3.01	16.87	C1s	284.82	3.55	14.52	C1s	284.82	3.25	14.81
Ca2p	347.50	1.97	0.27	Ca2p	347.26	3.48	0.35	Ca2p	347.27	3.43	0.43
Cr2p	577.84	4.25	1.09	Cr2p	577.51	4.36	2.26	Cr2p	577.25	3.83	2.34
Cu2p3	933.94	0.08	0.01	Cu2p3	934.35	1.33	0.01	Cu2p3	935.48	1.39	0.02
Fe2p	711.26	4.71	0.07	Fe2p	711.73	3.37	0.08	Fe2p	710.90	3.80	0.07
Mg1s	1304.83	0.98	0.02	Mg1s	1304.34	0.81	0.03	Mg1s	1304.83	3.22	0.06
N1s	399.82	3.62	0.88	N1s	399.66	3.39	1.25	N1s	399.66	3.70	1.02
Na1s	1070.72	0.49	0.02	Na1s	1071.27	1.29	0.01	Na1s	1071.78	5.43	0.08
O1s	531.44	3.49	11.81	O1s	531.22	3.51	15.00	O1s	531.34	3.50	14.51
Zn2p	1031.55	3.07	0.08	Zn2p	1032.93	4.24	0.12	Zn2p	1039.27	1.71	0.10

4.3.3.3 Al2219 CCC treatment as a function of aging

Chemical conversion coating was evaluated for degradation as a function of aging time. Al2219 samples were evaluated immediately at two-time intervals: (1) after 24-hour drying of CCC application (fresh samples), and (2) after three months of storage (aged samples). The samples were stored indoors, at ambient temperatures, and with an average relative humidity of 51%. This environment correlates to the typical storage conditions for the crew module vehicle. Figure 44, Figure 45, and Figure 46 provides XPS survey overlays of the surface analysis of the fresh samples and aged CCC samples comparatively. High resolution spectrums of key elements identifying chemical state changes are also included.

The overlay of the spectrum shows no significant changes in the elemental survey between the fresh samples and the aged samples. It must be noted that the copper peak Cu2p 3/2 was sharp and defined in the fresh samples but was very narrow and not pronounced in the aged samples. The lack of the copper peak in the aged sample is probably due to the area being examined since the intermetallics are precipitates that are randomly found across the surface of the aluminum matrix. The XPS spot area is 400 µm and is small enough to not include a copper intermetallic.
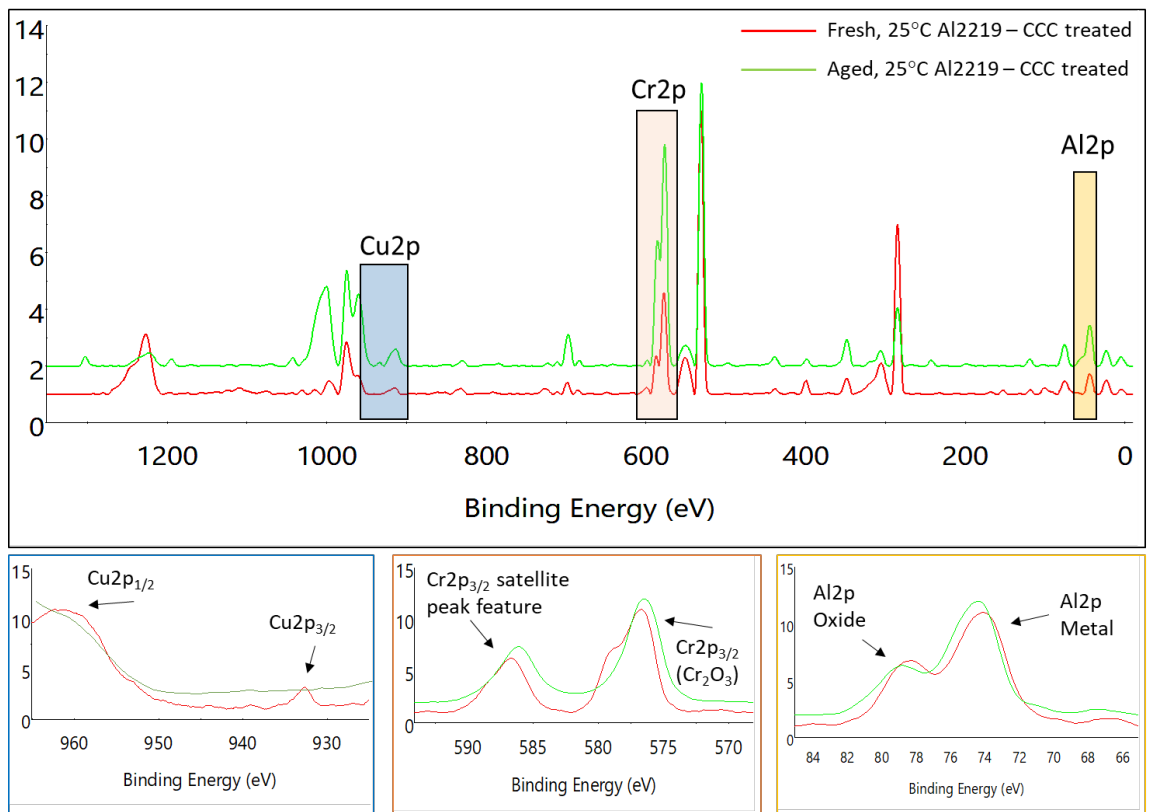
Figure 44: (Top) XPS overlays of the survey spectrum for fresh and Aged CCC coating on Al2219 alloy at room temperature. (Bottom) High resolution XPS spectrum of overlays of the chemical states of key elements for comparison: (a) Cu2p, (b) Cr2p, and (c) Al2p.
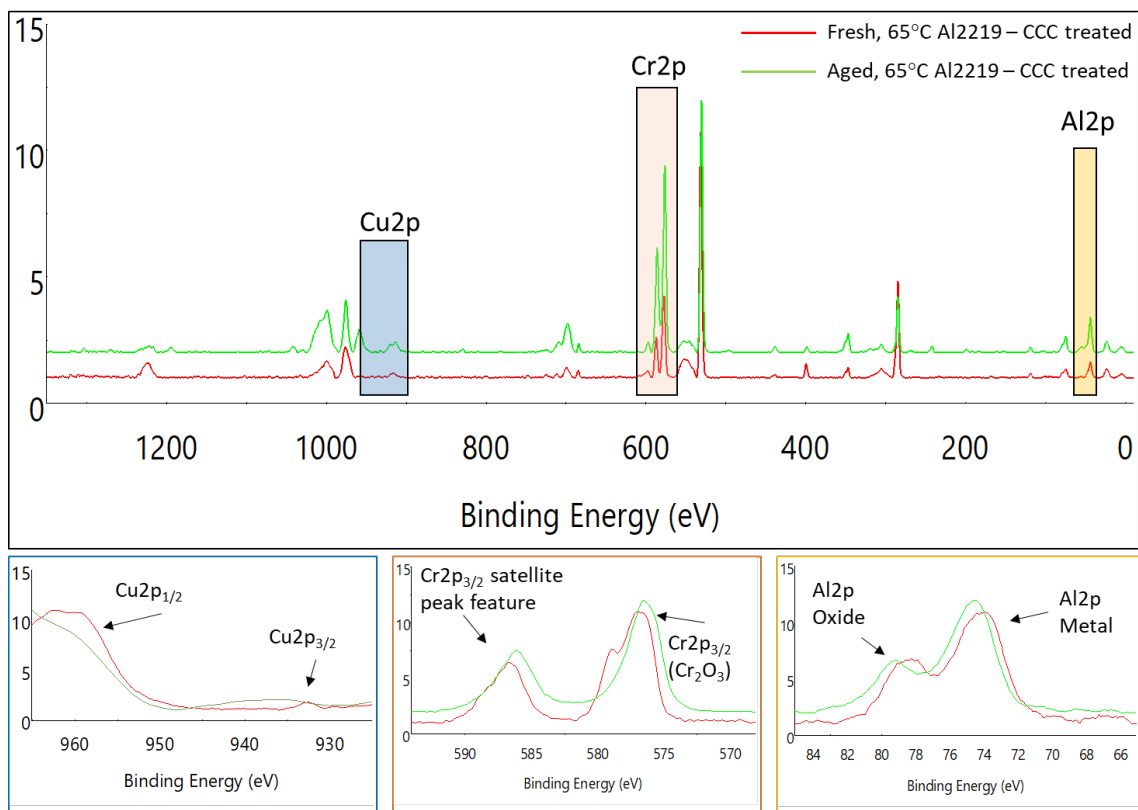
Figure 45: (Top) XPS overlays of the survey spectrum for fresh and Aged CCC coating on Al2219 alloy heated to 65°C. (Bottom) High resolution XPS spectrum of overlays of the chemical states of key elements for comparison: (a) Cu2p, (b) Cr2p, and (c) Al2p.
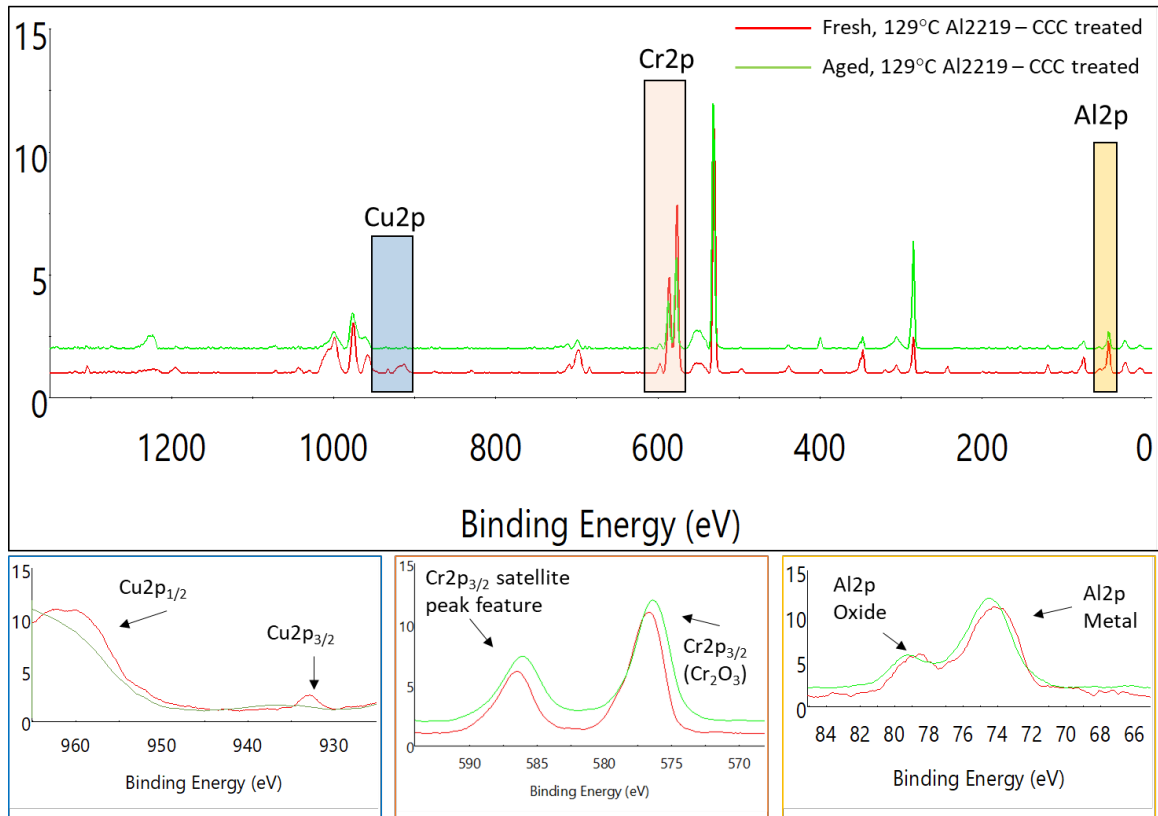
Figure 46: (Top) XPS overlays of the survey spectrum for fresh and Aged CCC coating on Al2219 alloy heated to 129°C. (Bottom) High resolution XPS spectrum of overlays of the chemical states of key elements for comparison: (a) Cu2p, (b) Cr2p, and (c) Al2p.

Summary of XPS Surface Characterization of Chromate Conversion Coatings a function of heat treatment and aging

A comparative study utilizing XPS to evaluate the surface characteristics of the application of chemical conversion coating on Al2219, CCC application as a function of elevated temperature exposure, and CCC degradation as a function of time were all evaluated. The chromated conversion coating appears to give a layer composed of chromium in two different chemical states, Cr(II) in the form of chromium oxide, and Cr(VI) in the form of chromate. Evaluation of the freshly applied CCC with aged CCC application

In the next chapter corrosion properties of the coatings will be examined. The stability of the coating with temperature exposure for a marine landing environment will be evaluated. The corrosion product and coating chemical species will be investigated.

4.3.4 Electrochemical Evaluation of the Al2219 surface CCC treated as a function of heat treatment and time aged

Chromated conversion coating (CCC) on Al2219-T87 alloy was characterized by electrochemical impedance and linear polarization measurements. Corrosion rate and an equivalent circuit model was derived in order to understand the corrosion mechanism of these samples. Surface characterization of the samples evaluated for the (a) non-coated Al2219 alloy, (b) CCC treated alloy, (c) CCC heat treated to 65°C ±5°C, and (d) CCC 129°C ±5°C. The heat-treated coupons were heated for 16 hours and then followed electrochemical testing in 3.5% NaCl electrolyte in using Gamry Potentiostat and EChem Analyst software for data processing. To reduce noise, all measurement was taken in a faraday cage. The measurements started after an open-circuit delay of 1800 seconds at E_{corr}. The collected plots were used to compare the electrochemical corrosion behavior of the coatings with uncoated alloys and the integrity of coatings before and after heat treatment.

4.3.4.1 Corrosion Potential (Open Circuit Potential)

The corrosion potential, E_{corr}, which also referred to as the open circuit potential (OCP), was used to monitor the substrate surface in solution prior to performing electrochemical

measurements. The potential was measured in 3.5% NaCl solution until the samples reached a steady-state potential. E_{corr} values were measured prior to each electrochemical test and steady state conditions were verified which was between 1600 seconds to 1800 seconds. For example, Figure 47 shows the typical OCP of Al2219 surface for the non-coated and heat treated CCC samples. The OCP for the non-coated Al2219, CCC treated Al2219 at 25°C, 65°C series, and 129°C sample sets were about -678 mV, -661 mV, -655 mV, and -668 mV respectively. Typically, the electrode potential increased and decreased rapidly in first 15 minutes and then the potential kept steady.
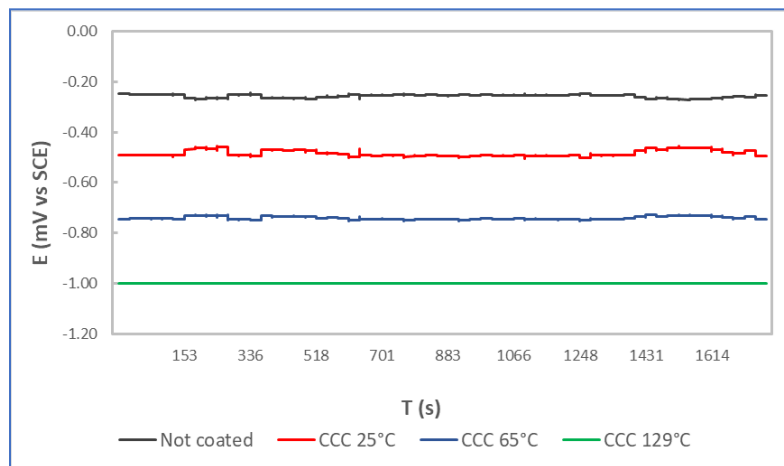
Figure 47: Potential vs time curve of CCC treated Al2219.

4.3.4.2 Polarization Resistance

After steady-state potential was reached, polarization resistance (R_p) was taken at ±10 mV vs E_{corr}. This non-destructive method uses a low current to measure the change in potential. The substrate's resistance to polarization was extracted from the slope of the linear region of the potential vs current density (Figure 47). The derived R_p is inversely proportional to the corrosion current density (i_{corr}). Greater R_p values imply a better corrosion protection. Figure 48(a) provides an example of the region used for analysis. R_p was determined by inserting the slope ($\Delta E/\Delta i$) into the Stern-Geary Equation:

$$R_p = \Delta E/\Delta i = \text{ßaßc}/2.3\ i_{corr}\ (\text{ßa} + \text{ßc})$$

Where i_{corr} = corrosion current (A) βa = anodic Tafel constant (V/decade) βc = cathodic Tafel constant (V/decade). i_{corr} was converted to corrosion rates, in milli-inches per year (mpy), and 120 values were selected for ßa and ßc and using Faraday's law and the following equation:

$$CR = i_{corr}\ K\ EW\ /\ \rho$$

Where $K = 1.288\times10^5$ milli-inches(Amp·cm·yr), ρ for aluminum = 2.84 g/cm^3 , and EW = equivalent weight (W/n = molecular weight/# of electrons) at 26.9815 for aluminum. The corrosion rate shows that the non-coated samples had the highest corrosion rate while the CCC treated samples had lower corrosion rates. Ultimately, both the room temperature and 65°C series samples that were CCC treated showed good corrosion resistance.

Calculated corrosion rates and R_p obtained from the collected I-E curves are listed in Figure 48(b). Anodic polarization of the coating after exposure to heat treatment displayed

the stable current density regions. This was taken to indicate that possible fine cracks might have resulted during the heat treatment at the low temperature. This led to a slightly higher corrosion rate from the no-heat treated samples. However, this value was still low and a large potential region at stable current density indicated that the coating on the 65 °C heat treated samples was still effective as a barrier to minimize the passage of the corrosive electrolyte to the underlying aluminum substrate. This was not seen for the 129 °C heat treated samples. The current density was unstable, and polarization was in the same range as the non-coated substrates.

(b)

Sample Series	R_p (ohm cm²)	Corrosion Rate (mpy)
Non-coated	6.71E+03	6.34
CCC 25°C	8.89E+05	0.05
CCC 65°C	1.17E+05	0.36
CCC 129°C	1.52E+04	2.80
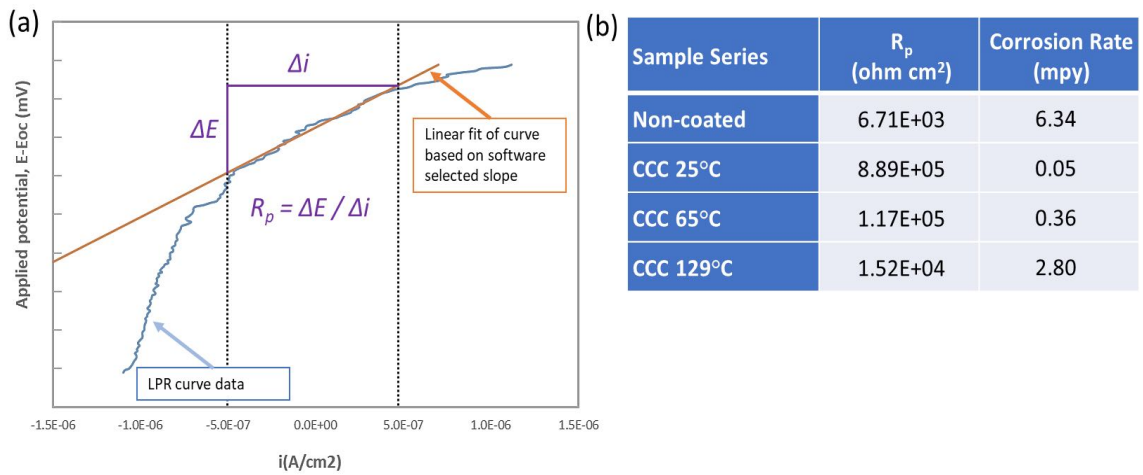
Figure 48: LPR principle and results of LPR measurements using the (a) extracted LPR value from the I-E curve and (b) Rp values of the uncoated AA2219 alloy, CCC coating after heat treatment. Example in the graph is from the CCC heat treated 129°C sample series.

4.3.4.3 Electrochemical Impedance Spectroscopy

The impedance measurements were carried out in 3.5% NaCl electrolyte solution. The experiment had a three-electrode configuration: Al2219 alloy was the working electrode, with a surface area of 0.75 cm², the counter electrode was a graphite rod, and the reference

utilized a standard calomel reference electrode. The examined frequency range was 100 kHz to 0.01 Hz.

The corrosion behavior of the CCC coated substrates was investigated by EIS. Figure 49(a) and Figure 49(b) depict the Bode plots for the no-heat, heat treated, elevated heat treatment of the alloys in 3.5% NaCl solution. The Bode plots are composed of the impedance modulus plot and the phase angle plot. Commonly, the phase angle describes the contributions of the resistive and capacitive portions to the impedance magnitude. A current passing through a capacitor is phase shifted by 90° with respect to the voltage while a current passing through a resistor will be in phase with the voltage. There are typically three different regions to consider: the high frequency region indicative of passivation, the mid frequency region which reflects changes in the coating layer in corrosive electrolyte, and the low frequency region where the metal/coating interface reaction in solution is observed. For the samples, polarization resistance increased with CCC treated samples at low temperatures while the solution resistance decreased with increasing temperatures. From this, it can be concluded that the capacitive portion of impedance is dominant at the high and low ends of the frequency range due to the series combination of the double layer impedance at the electrode-electrolyte interface, double layer at the coating-electrolyte interface, and the solution resistance.

Generally, in the phase angle plots the lower frequencies at about $10^0 – 10^2$ Hz is a typical indicator of the formation of aluminum oxide at the substrate interface with the electrolyte (83,122). This feature is observed in the non-coated aluminum sample and the 129°C heat

treated samples. At higher frequencies, $10^4 - 10^5$ Hz, is associated with the capacitive coating behavior of the CCC (83,122). The phase angle at middle frequencies, $10^2 - 10^3$ Hz, could be related to the interlayer capacitance changes of the substrate.

Figure 50 depicts the Nyquist plot which shows complex plane Z'' vs. Z' and the capacitive arc provides an estimate of corrosion resistance of the material, in terms of its relative diameter, which is directly proportional to the charge transfer resistance or polarization resistance (R_p). The higher charge-transfer resistance indicates better the corrosion resistance and so an increase in the semicircle diameter will be seen and vice versa. The Nyquist plot show that the non-coated Al2219, CCC treated samples, and CCC treated samples at elevated temperatures. The coated samples are characterized by a relevant increase in impedance in all frequency ranges with optimal results for the CCC treated samples at 25°C and 65°C. Additionally, the impedance of the coated samples decreases significantly with the increase in heat treatment and in the non-coated samples. These results imply that the impedance responses of samples are sensitive to temperature and coating.

For further insight into the corrosion behavior, the EIS data were fitted with the appropriate equivalent circuit models (ECM). Figure 51 illustrates the equivalent circuits used to describe the both the non-coated aluminum substrate and the conversion coating on the aluminum substrate alongside their respective surface models. These two circuit models are generally used in literature to evaluate bare substrates and CCC treated substrates which allows comparisons to be made between the current data obtained and the data found in literature and were used for impedance fitting. The ECM for the non-coated aluminum

alloy samples consists of electrolyte solution resistor (R_s) which is in series with constant phase element (CPE) which accounts for the double-layer capacitance. CPE is in parallel with charge transfer resistance (R_{ct}). Model b ECM corresponds to the CCC treated aluminum alloy samples. The circuit consists of solution resistor (Rs) which is in series with constant phase element (CPE) which represent the capacitance of the coating. CPE is connected parallel with charge transfer resistance (R_{ct}). CPE is used to resolve the imperfect capacitance of coating materials and greatly enhances the flexibility of the ECM process by accounting for the phase shift response of the AC current (21,46). The ECM for the CCC treated aluminum surface consists of the electrolyte solution circuit described as resistor for the solution resistance (R_s). The barrier layer is described by polarization resistance (R_p) and coating capacitance (C_c). C_c was treated as a constant phase element (CPE). CPEs are used instead of capacitors to account for a nonideal capacitive behavior. Since the CCC is porous, a diffusion element is also considered here and is placed in series with R_p, which models the diffusion process through the chromate corrosion product. This element was also used in the non-coated aluminum substrate due to aluminum's naturally occurring porous aluminum oxide feature. This additional element is described as the Warburg Impedance W, where W is defined as:

$$W = \sigma_w \, \omega^{-1/2} \, (1 - i)$$

σ_w is the Warburg impedance coefficient (ohm cm^2 s$^{-1/2}$) and ω the angular frequency (rad s^{-1}).
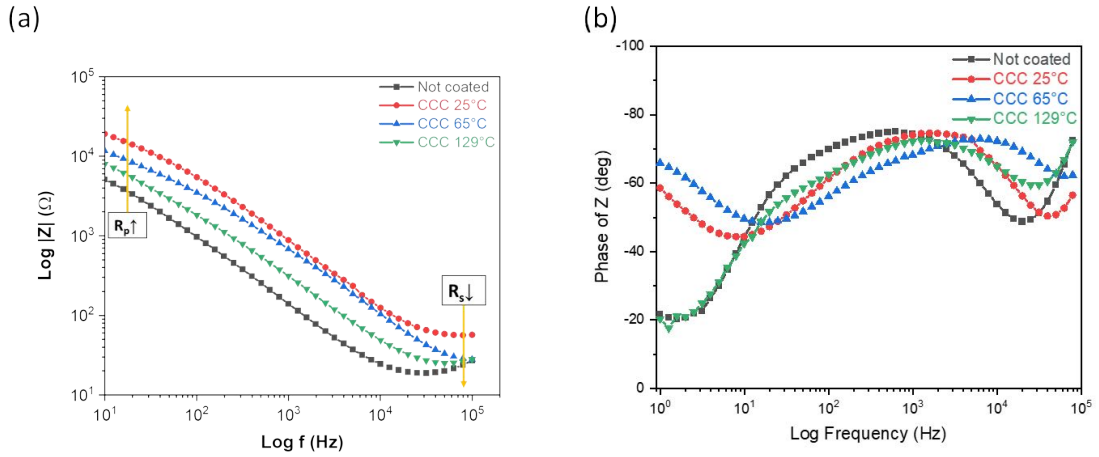
Figure 49: Bode plots, (a) logarithm of the modulus of the impedance and (b) phase angle vs. the logarithm of the frequency, in 3.5% NaCl for the non-coated Al2219 alloy, CCC treated alloy, CCC treated alloy heat treated to 65°C ±5°C, and CCC treated alloy heated to129°C ±5°C.

Figure 50: Nyquist plot of electrochemical impedance spectroscopy (EIS) with insets of magnifications at low Z′ and Z″ values. The symbols represent the actual data measured; the lines indicate the fit to the equivalent circuit shown.

Figure 51: Equivalent circuits models used for fitting the EIS data of the (a) non-coated Al2219 alloy and (b) heat treated CCC Al2219 samples along with their perspective surface models.

Summary of surface characterization via electrochemical studies

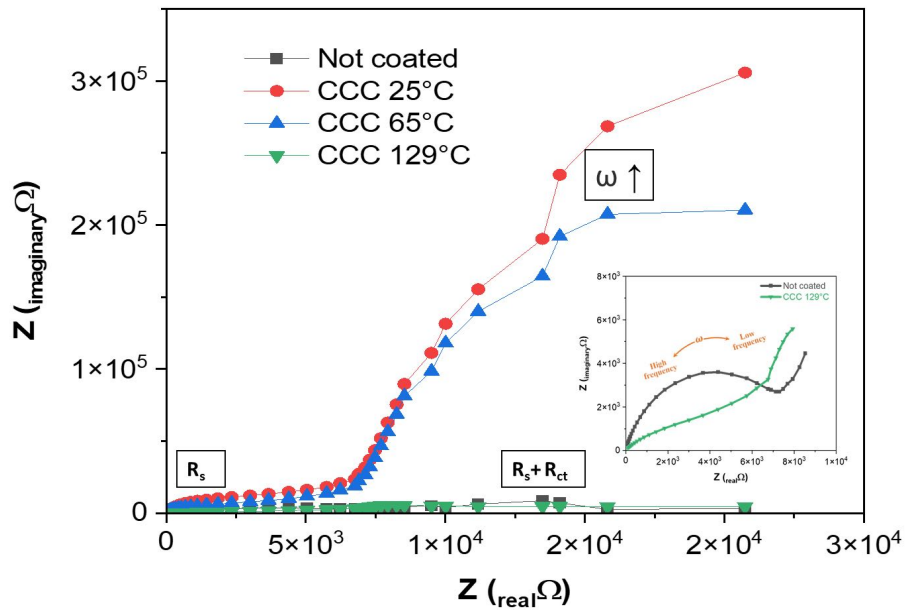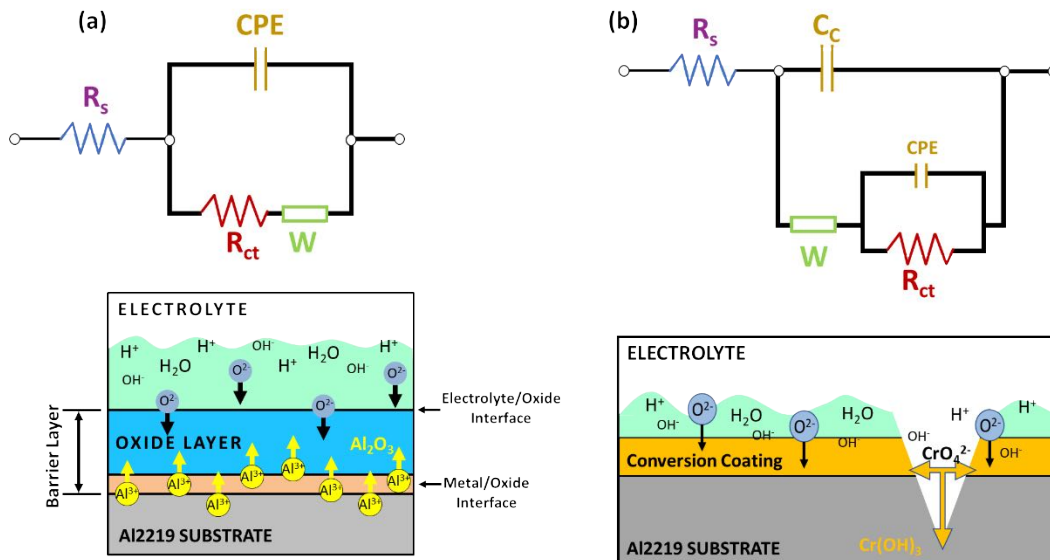Polarization plots from the electrochemical tests were evaluated using the Stearn Geary Equation. The noncoated Al2219 alloy and the CCC samples that were heat treated to 129°C displayed an immediate rapid increase of the current density on slightly increasing the potential from E_{corr}. This immediate rise of the anodic current density is indicative of rapid corrosion occurring at the surface of the uncoated alloy and the electrolyte. The CCC treated samples that were heat treated to 65°C and the non-heated samples displayed a large potential range that was more positive from the E_{corr}, which is indicative of very little corrosion occurring between the coating and the electrolyte. The bode plots confirms consistency in CCC film across the samples. Summarily, the equivalent circuit suggests a transition layer between the CCC and the alloy, as it is also observed on anodically produced aluminum oxide.

Impedance decreased with increasing temperature which correlated with the decrease in coating resistance with increasing temperature. Higher heat treatment exhibited more defect sites that allow electrolyte to impinge on the substrate, which results in less corrosion protection.

4.4 Neutral Salt-Fog (ASTM B117): Corrosion testing of the CCC Al2219 surface as a function of heat treatment and aging

The corrosion performance of uncoated and CCC treated, heat treated, aged test specimens were examined by exposing the samples to a salt spray environment following the guidelines described in the ASTM standard B117 up to 168 hours of exposure period. The testing comprised of exposing the coating surface up to 168 hours to a 3.5% NaCl solution (at 35°C) atomized to create a fog within an enclosed chamber. The composition of this alloy is Cu 5.8-6.8 wt.%, Mn 0.2-0.4 wt.%, Fe 0.0-0.3 wt.% and Al to balance. Surface profilometry and SEM/EDS analysis were performed to evaluate the localized corrosion on the aluminum substrate. Pitting density, changes in morphology, and elemental composition of the surface as a function of aging and heating were monitored. Since the major secondary phase precipitates are Al_2Cu that are considered cathodic with respect to the aluminum matrix, their conformation was observed as well. Surface characterization of the coated samples were done at two-time intervals: (a) immediately after chemical conversion coating application and (b) after the coating was aged for three months. The coupons that underwent heat treatment were exposed to heated conditions at two heat treatment temperatures (1) 65°C ±5°C and (2) 129°C ±5°C for 16 hours and the samples.

Neutral salt fog:

CCC treated Al2219 along with non-coated Al2219 samples of approximately 76mm x 76 mm were placed in the Neutral Salt Fog Chamber (ASTM B117) for 168 hours (7 days). The Salt Fog Chamber isolates chlorides, temperature, and water vapor to accelerate corrosion reactions. The chamber continuously uses a salty fog of 3.5% NaCl at 35°C to maintain one-hundred percent RH values to ensure a constant salty moisture. The samples were placed in the chamber at 30° from the vertical on test racks for 168 hours (7days) and were photographed immediately after removal. The salt spray exposure was carried out in a Q-Fog chamber.

4.4.1   Visual inspection of CCC treated samples as a function of aging and heat treatment

For comparison, non-coated Al2219 was processed alongside the coated samples. For the aged samples, SEM images were taken monthly prior to salt fog to investigate time of mud-cracking. Figure 52 shows example SEM images captured illustrating the surface integrity of the chemical conversion coated Al2219 substrate (left) and remaining images are monthly SEM images showing no mud-cracking morphology.
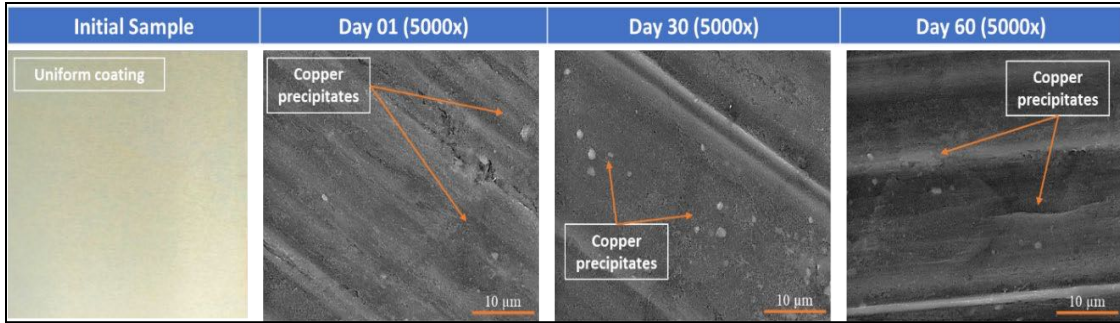
Figure 52: Picture of the surface integrity of chemical conversion coated Al2219 substrate (left) and remaining images are monthly SEM images showing no mud-cracking morphology.

Figure 53 and Figure 54 show images of the process flow (Table 7) for the fresh and aged CCC treated samples: (a) CCC/not heated, (b) CCC/heated to 65°C, and (c) CCC/heated to 129°C. Since the results were very similar within each temperature group, images from a sample specimen per temperature series will be presented. Overall, the characterization process included surface analysis of all samples immediately after CCC treatment, heat treatment, salt fog exposure, removal of corrosion product, and corrosion analysis.

Summarily, the coating of the CCC samples that were heated to 65°C experienced a color change from iridescent gold to dark brown and had minimal corrosion product on the surface. The coating of the CCC samples that were heated to 129°C experienced a color change from translucent gold to almost bare metal and was completely covered in white corrosion product on the surface. The coating of the CCC samples that was not heat treated maintained the same iridescent gold color and there were no visual signs of white corrosion product on the surface.

While the fresh CCC treated samples were processed immediately, the aged samples were stored in a humidity-controlled room to simulate the storage environment that flight hardware undergoes during processing. The aged samples were visually inspected monthly and evaluated for mud-cracking morphology. The mud-cracking morphology was not observed in any samples prior to processing. Figure 54 shows the typical appearance of the coating during aging.

	Before Heating	After Heating (16 hours)	After Salt Fog (168 hours)	After Corrosion Product Cleaning
Not coated		No Heating		
No Heat Series		No Heating		No Cleaning
65°C Series				No Cleaning
129°C Series				

Figure 53: Images of freshly coated CCC treated Al2219 at different temperatures and processing. Samples were processed immediately after CCC dried.

	Before Heating	After Heating (16 hours)	After Salt Fog (168 hours)	After Corrosion Product Cleaning
Not coated		No Heating		
No Heat Series		No Heating		No Cleaning
65°C Series				No Cleaning
129°C Series				

Figure 54: Images of CCC treated Al2219 aged three months at different temperatures and processing.

Visual inspection After heat treatment

After heating for 16 hours, the samples cooled down to room temperature for about 20-30 min. For both the freshly applied CCC and aged samples, heat treatment did not produce visible coating defects in the samples (Figure 55). No cracks, delamination, or other form of degradation after heat exposure were observed from either of the two temperatures series (65°C and 129°C). However, after heat treatment, the coating of the 129°C did lose the translucent gold color. It was evident that the coating was very thin in this series. This probably occurred due to dehydration of the samples.

Visual inspection After salt fog exposure

After 168 hours (7 days) of salt fog exposure, visual inspection was performed immediately after pulling the samples from the salt fog chamber (Figure 53 and Figure 54). For both the freshly coated series and the aged series, a thick white layer of corrosion product (aluminum oxide) was observed on the samples that were heat treated to 129°C and the non-coated Al2219 samples. The non-coated Al2219 samples and the 129°C heat treated samples required a nitric acid clean to remove the white corrosion product build. All samples were rinsed with deionized water prior to further analysis. This was performed for these two series for both the freshly coated trials and the aged trials. Regardless of aging, both the no-heat treatment series and the 65°C heat treatment series, showed minimal visual evidence of corrosion product buildup. These samples had little to no corrosion product build up and did not require a nitric acid clean and were only rinsed with deionized water and allowed to air dry.

4.4.2   SEM/EDS of the surface and intermetallic as a function of heat treatment and aging

Energy dispersive x-ray spectroscopy (EDS) associated with a scanning electron microscope (SEM) is the most common technique used to obtain chemical identification of corrosion products. EDS can detect elements C through U with a detectability limit of about 0.1 weight percent. The scanned electron beam interacts with the specimen's surface, which produces secondary and back-scattered electrons and x-rays. These x-rays are characteristic for the element that emits them and can be used to identify the elemental

composition of corrosion products. The current analysis produced semi-quantitative analysis using the Oxford computer software. While the exact composition of the corrosion product cannot be concluded, information regarding which metals are present can be derived along with a general concentration of the metals that are present. A relatively modest beam current was used to produce a high-count rate and facilitate rapid element mapping. However, the interaction between the current and the surface corrosion product causes charging. This can produce images that have blurriness, streaks, and bright areas on the images. The analysis provides a high-resolution analysis of the surface, and so to reduce the charging the surface was cleaned, and majority of the surface corrosion product was removed before analysis. Carbon contamination is well known to be more prevalent on high energy surfaces and it was noted that there was higher concentration of carbon on the conversion coating rather than in the cracks. However, to better monitor the surface distribution of the elements of interest, carbon was removed from the EDS analysis. EDS analysis was focused on the intermetallic and overall changes and areas of concentration for the aluminum, oxygen, copper, and chromium elements.

Figure 55 illustrates examples of SEM images of the fresh CCC samples for the no-heat treatment series, heat treatment to 65°C series, and heat treatment to 129°C series at each processing steps. SEM observations of the fresh CCC samples with no-heat treatment maintained a more uniformed surface appearance than the heat-treated samples. These samples had very little to no surface defects and the mud-cracking morphology was not observed in the areas analyzed. SEM observation of the fresh CCC samples heated to 65°C showed minor mud-cracking features and this was not continuous across the surface.

Initiation sites of micro-mud-cracking formation was found randomly on the surface. This feature was not consistent across the surface of the samples. However, for the samples heat treated to 129°C, wide trough pits were observed across the surface of the coating and coating degradation was severe. Mud-cracking was observed in random areas and was not seen consistently across the surface. The mud-cracking that was observed had wide cracks that gave way to full coating separation and there were large areas on the surface with no coating.

Figure 55: SEM images (5000x) of the fresh CCC Al2219 surface (a) prior to heat treatment, (b) after prescribed heat treatment, and (c) after neutral salt fog.

Figure 56: SEM images (5000x) of the three months aged CCC Al2219 surface (a) prior to heat treatment, (b) after prescribed heat treatment, and (c) after neutral salt fog.

In the three months aged samples as seen in Figure 56, mud-cracking was observed on all samples after salt fog exposure. SEM observations of the aged CCC samples with no-heat treatment maintained a more uniformed surface appearance than the heat-treated samples. SEM observation of the aged CCC samples heated to 65°C showed non-continuous mud-cracking features across the surface. The widths of the mud-cracking did increase into full coating separation in some areas and shallow, trough pits were observed on the surface of the coating. The aged CCC samples heated to 129°C showed consistently wide trough pitting and large areas on the surface had significant coating degradation.

EDS mapping of select samples are illustrated in Figure 58, Figure 59, and Figure 60. Key features that were found on the surface of the samples are summarized in Figure 61 and Figure 62.

Generally, in all samples, regardless of age and heat treatment, the mud-cracking morphology was observed after salt fog exposure and the 129°C series had severe coating degradation. Semi-quantitative EDS analysis showed a uniform intensity of aluminum and oxygen throughout the samples despite aging and heat treatment. There was also a consistent chromium intensity across the surface of the samples but there was a lower intensity of chromium in the areas between the cracking in the mud-crack feature. Both the freshly coated and aged CCC samples that were heated to 129°C had large areas of no coating and was indicated by very little to no chromium peaks in those areas. Additionally, copper had a high intensity at the intermetallic sites despite the age and heat treatment of the samples. While oxygen and chromium had a low intensity around the intermetallic region, and yet have an enhanced intensity along the general surface compared to that in the cracks. This may indicate that the chromate coating is thinner in the cracked regions as suggested by the EDS mapping in Figure 57 for the fresh CCC treated samples and Figure 58 for the three months aged samples. Pitting was not observed in the samples that did not undergo heat treatment (Figure 57). However, pitting was found on all heat-treated samples. The samples that were heat treated to 65°C had smaller pits compared to the 129°C heat-treated samples (Figure 58, Figure 61, and Figure 62). The pitting size was not linked to aging for these samples.

Figure 57: EDS mapping of the typical coating features found on the surface of the fresh CCC treated samples after 168 hours of salt fog exposure and no-heat treatment.
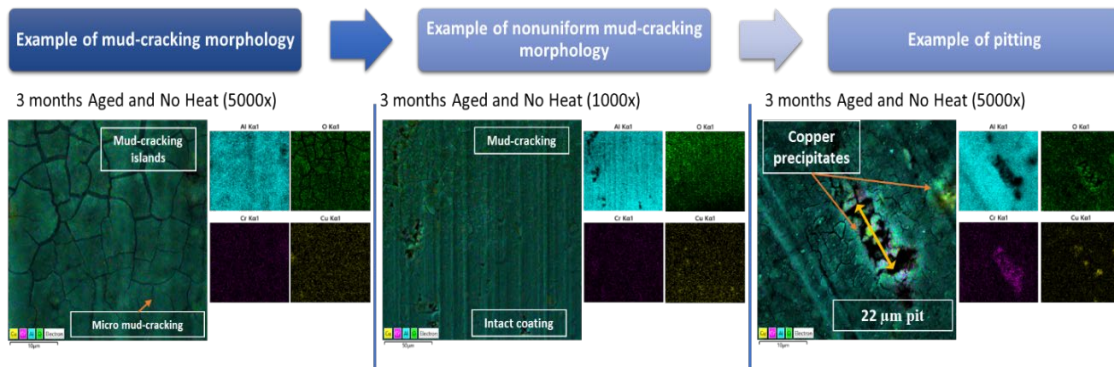
Figure 58: EDS mapping of the typical coating features found on the surface of the three months aged CCC treated samples after 168 hours of salt fog exposure and no-heat treatment.
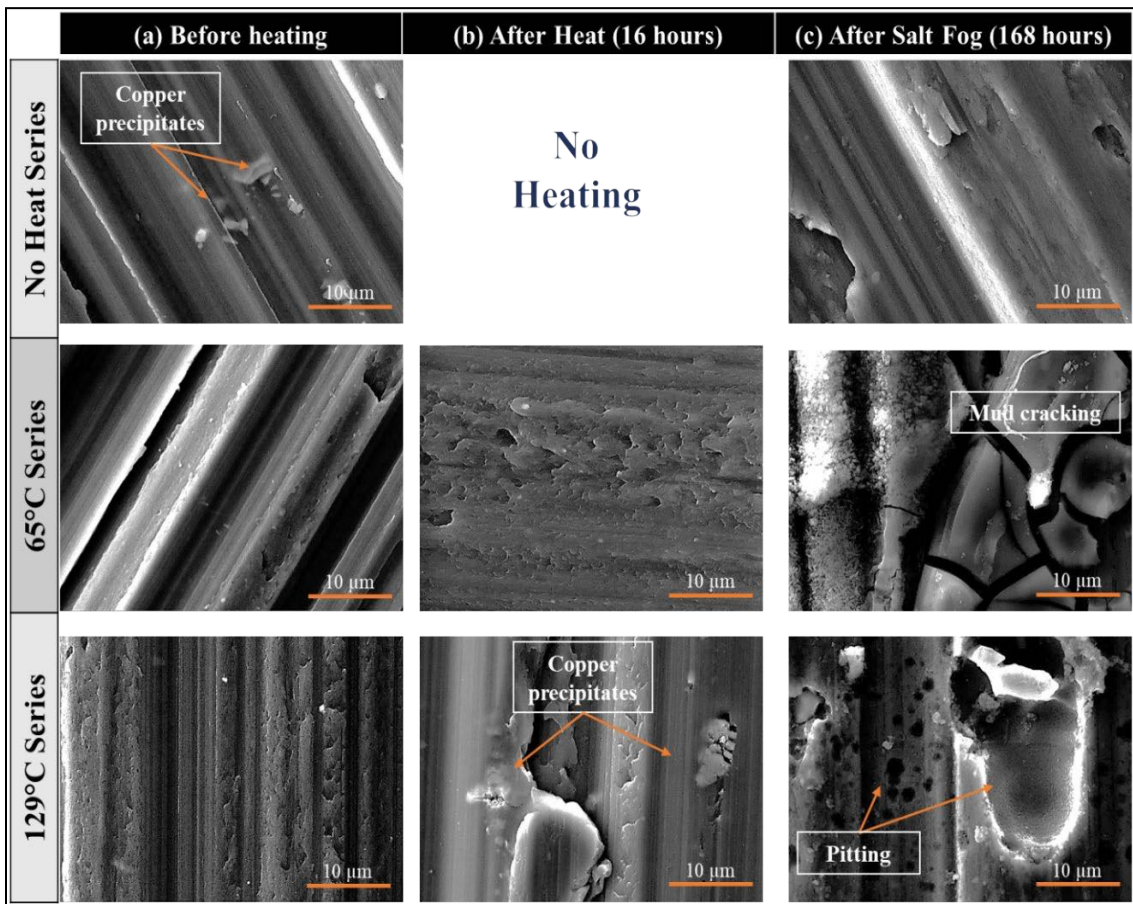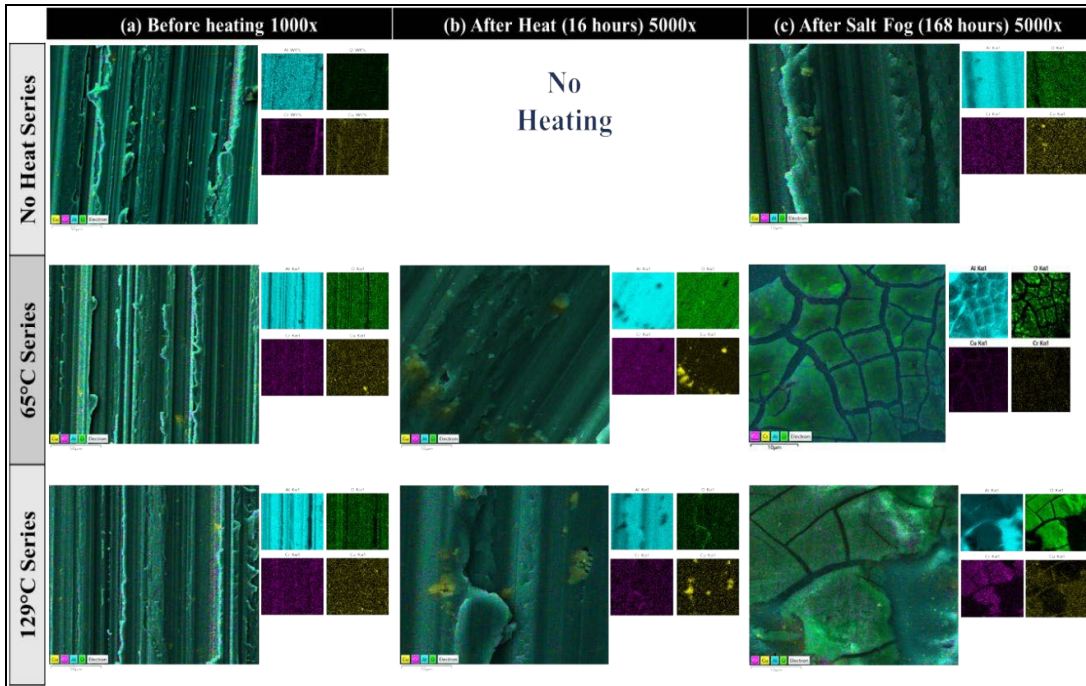
Figure 59: EDS mapping of the fresh CCC Al2219 surface (a) prior to heat treatment, (b) after prescribed heat treatment, and (c) after neutral salt fog.
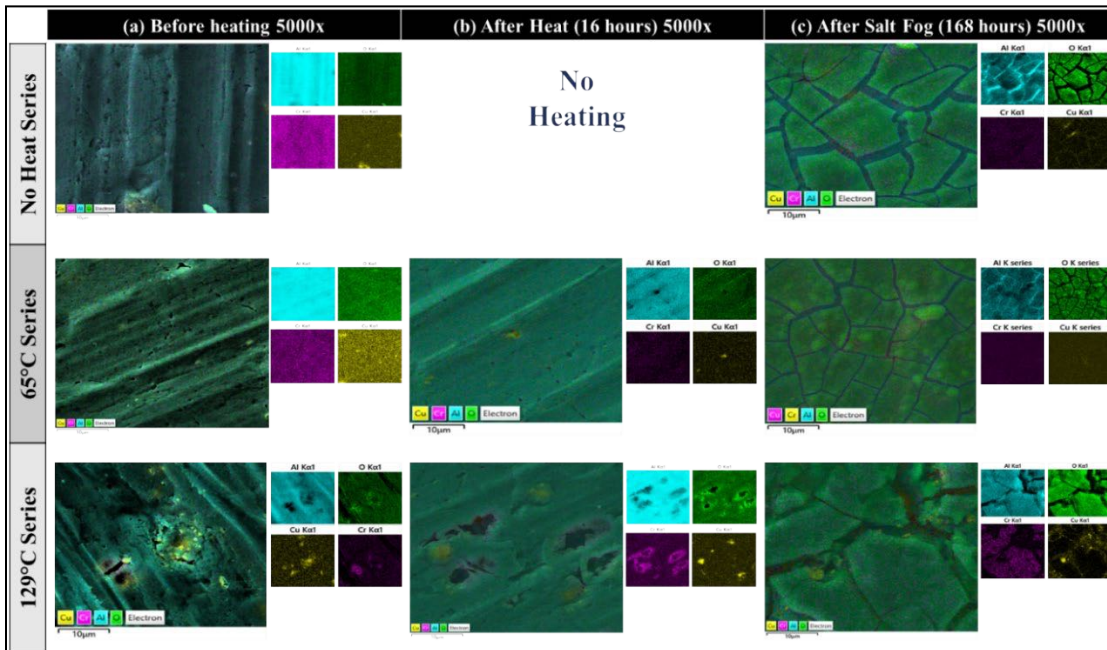
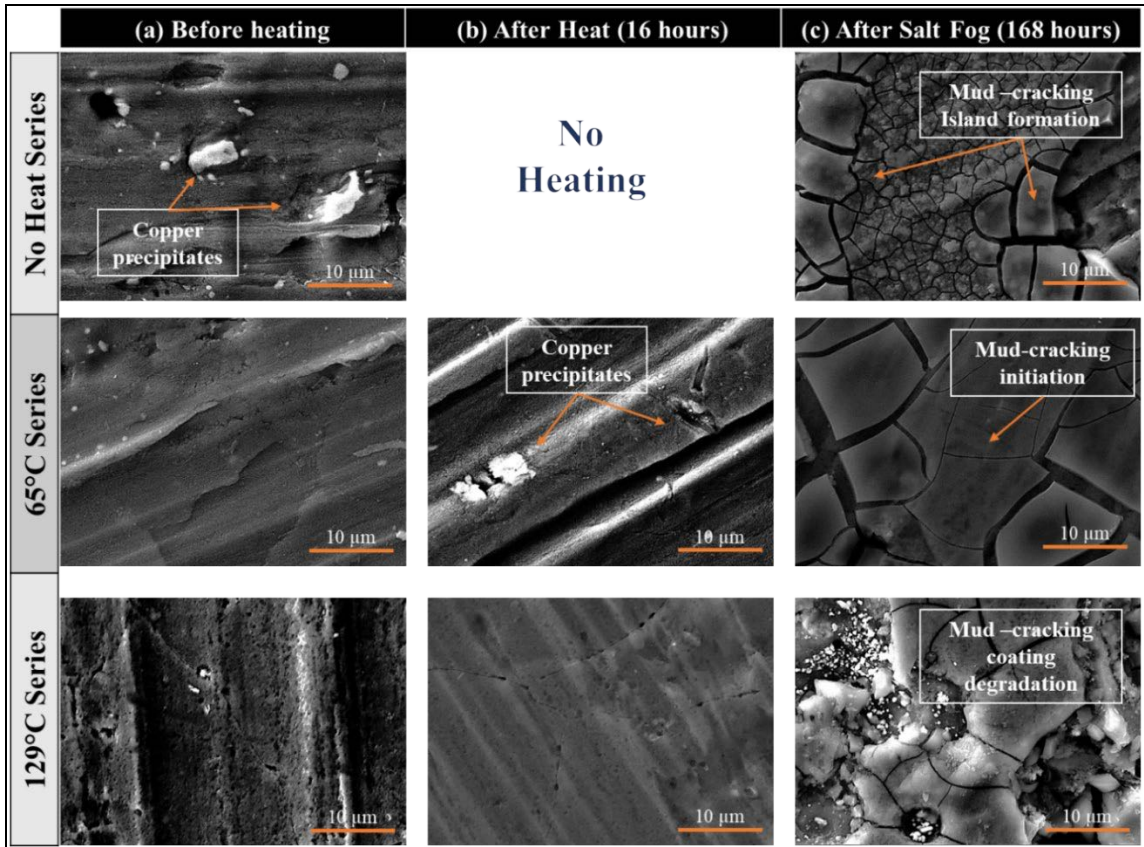Figure 60: EDS mapping of three months aged, CCC Al2219 surface (a) prior to heat treatment, (b) after prescribed heat treatment, and (c) after neutral salt fog.
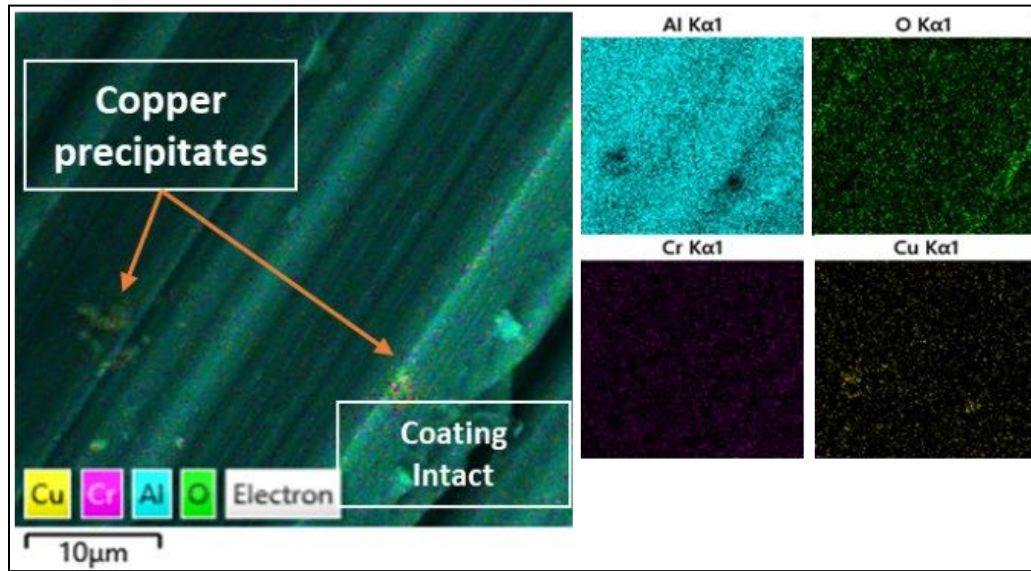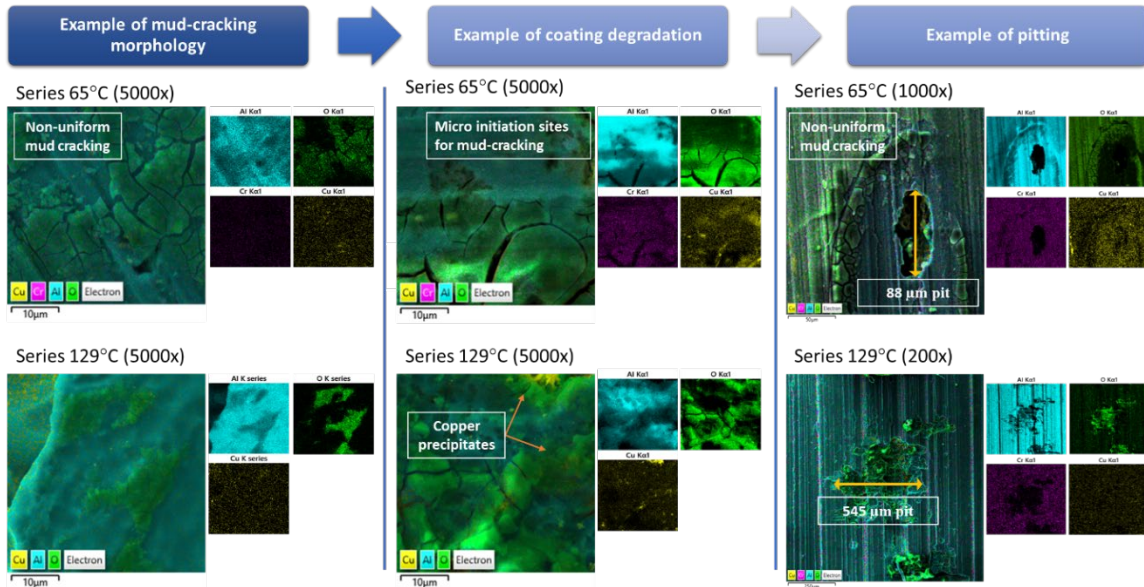
Figure 61: EDS mapping of the typical coating features found on the fresh CCC treated samples after 168 hours of salt fog exposure.
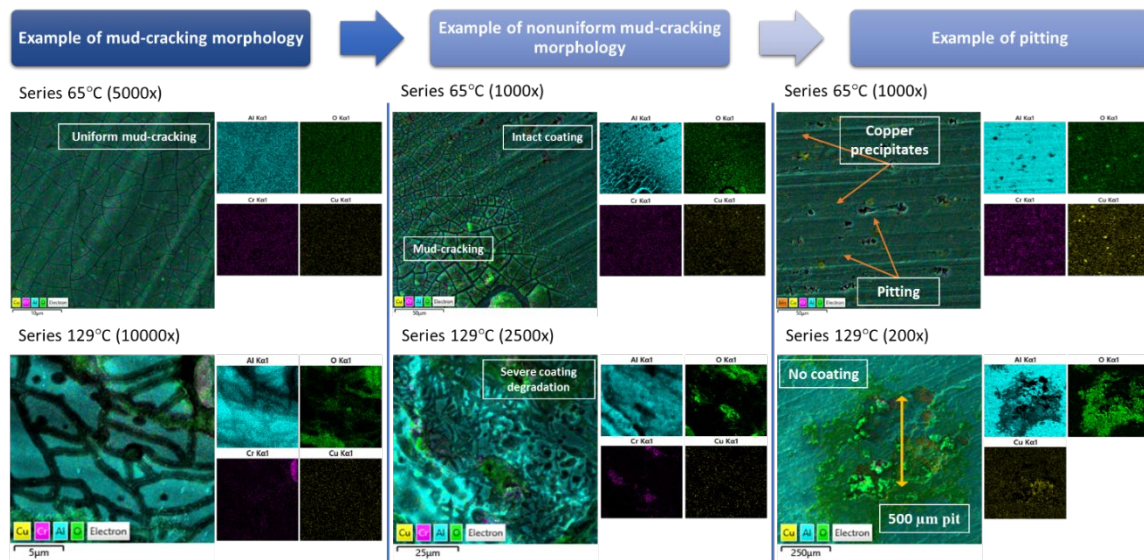
Figure 62: EDS mapping of the typical coating features found on the three months aged CCC treated samples after the prescribed heat treatment and 168 hours of salt fog exposure.

4.4.3 Profilometry characterization of pitting density and morphology

After salt fog exposure, Keyence VR-5000 Profilometer was used to measure the surface of all the CCC treated samples. The area measured was about 50mm x 50mm and the rough edges of the samples were not included in the analysis. The characteristics of the corrosion pitted aluminum samples were evaluated by density, size, depth, and shape were used to qualify the level of corrosion observed to make qualitative comparisons between the sample sets. The non-coated Al2219 sample was evaluated alongside the CCC treated samples as illustrated in Figure 63 of the pit density as determined by optical profilometer after 168 hours in Neutral Salt Fog 3.5% NaCl (followed by chemical cleaning of corrosion products). Figure 64 and Figure 65 are the 3D view and height variation in false color view which shows the overall shape, depth, and density of pitting across the surface of the samples for both the fresh and aging sample sets. The average values were reported for the fresh CCC and the three months aged series being evaluated by not heat treatment, heat treated to 65°C, and heat treated to 129°C. Additionally, the non-coated Al2219 was evaluated in the same manner for comparison.

The untreated Al2219 samples were processed in the neutral salt fog chamber for 168 hours (7 days) and was treated as the control for comparison of the CCC treated samples. After salt fog exposure, the untreated Al2219 samples had a thick white corrosion product across the surface. The samples were cleaned with nitric acid and then rinsed with deionized water. After drying, the samples were analyzed using the profilometer and is illustrated in Figure 66. The untreated samples had significant pitting with pit depth ranging from 8 μm to 123 μm. Pitting covered the entire coupon surface area at >800 pits per coupon. Many of the pits found were wide and deep had an average diameter of 1200 μm.

For the fresh CCC treated samples, the no-heat series had no pitting and no corrosion product build up on the surface. The samples heat treated to 65°C had minimal pitting, pit depth ranged from 23 μm to 110 μm. There was an average of less than 100 pits across the surface and an average diameter of about 800 μm. These pits were sparse, elongated, and shallow. The samples heat treated to 129°C had a pit depth ranged from 13μm to 80 μm and pitting was severe and very similar to the untreated Al2219 samples. Pitting covered the entire coupon surface area at >700 pits per coupon. Many of the pits found were wide and deep had an average diameter of 700 μm - 1200 μm. Using three-dimensional optical profilometry image, Figure 67 shows the variation in pitting density between the fresh samples.

The three months aged CCC treated samples were similar to the fresh samples. The no-heat series had no pitting and the samples heat treated to 65°C had minimal pitting. The 65°C heat treated samples had pit depth range from 10 μm to 70 μm and pitting with average diameter of 400 μm – 1100 μm. On average there were less than 100 pits across the surface. The samples heat treated to 129°C had a pit depth that ranged from and with average diameter of 900 μm – 1600 μm. The 129°C series was similar to the untreated Al2219 samples as the pitting was wide, deep, and dense across the surface. Figure 68 shows the variation in pitting density between the three months aged samples.
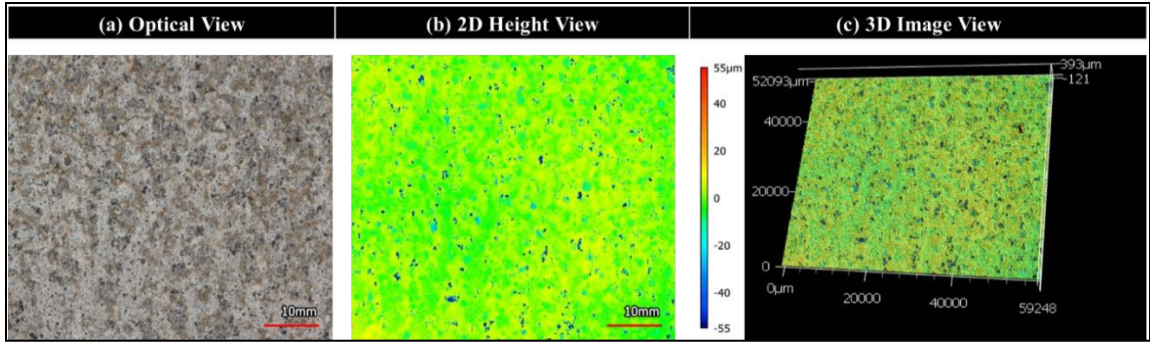
Figure 63: Non-coated Al2219 pit density as determined by optical profilometer after 168 hours in Neutral Salt Fog 3.5% NaCl (followed by chemical cleaning of corrosion products).
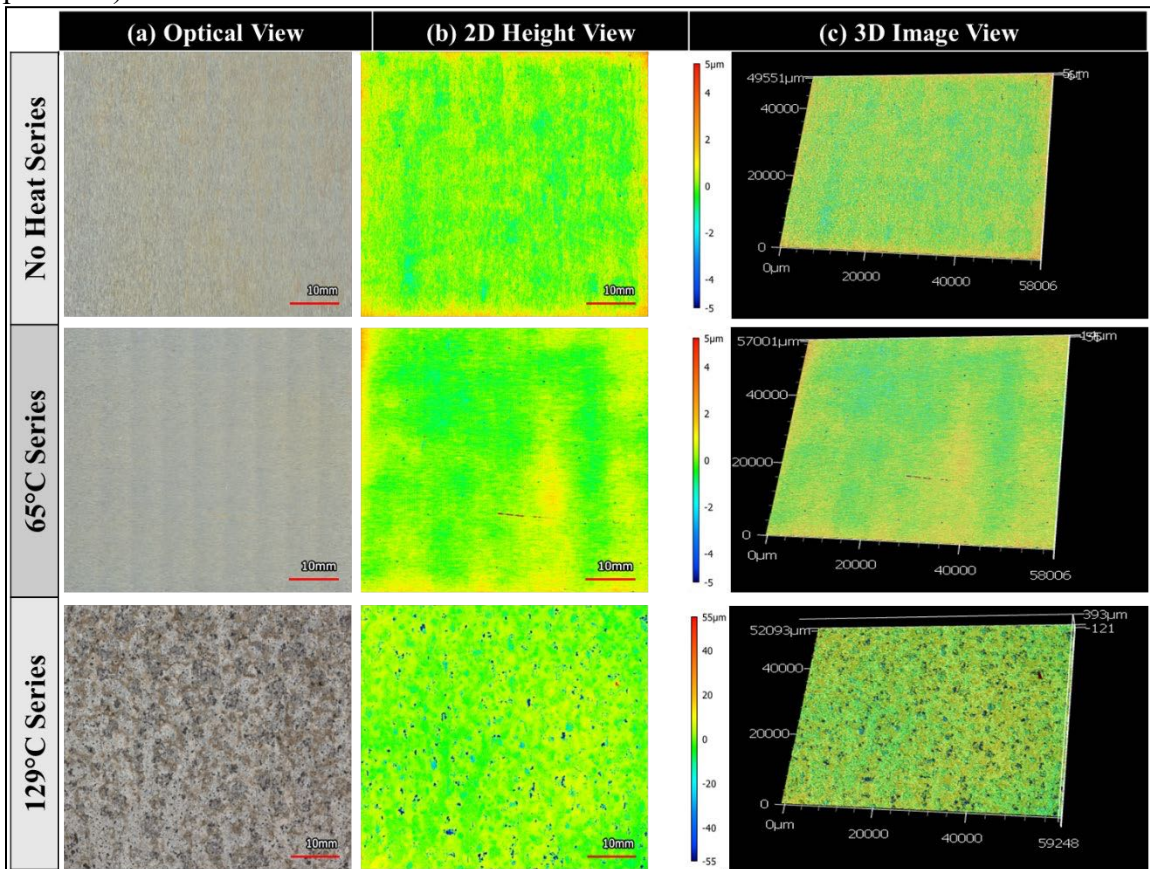
Figure 64: . Optical profilometry images of Fresh CCC treated Al2219 samples after 168 hours in Neutral Salt Fog 3.5% NaCl (followed by chemical cleaning of corrosion products).
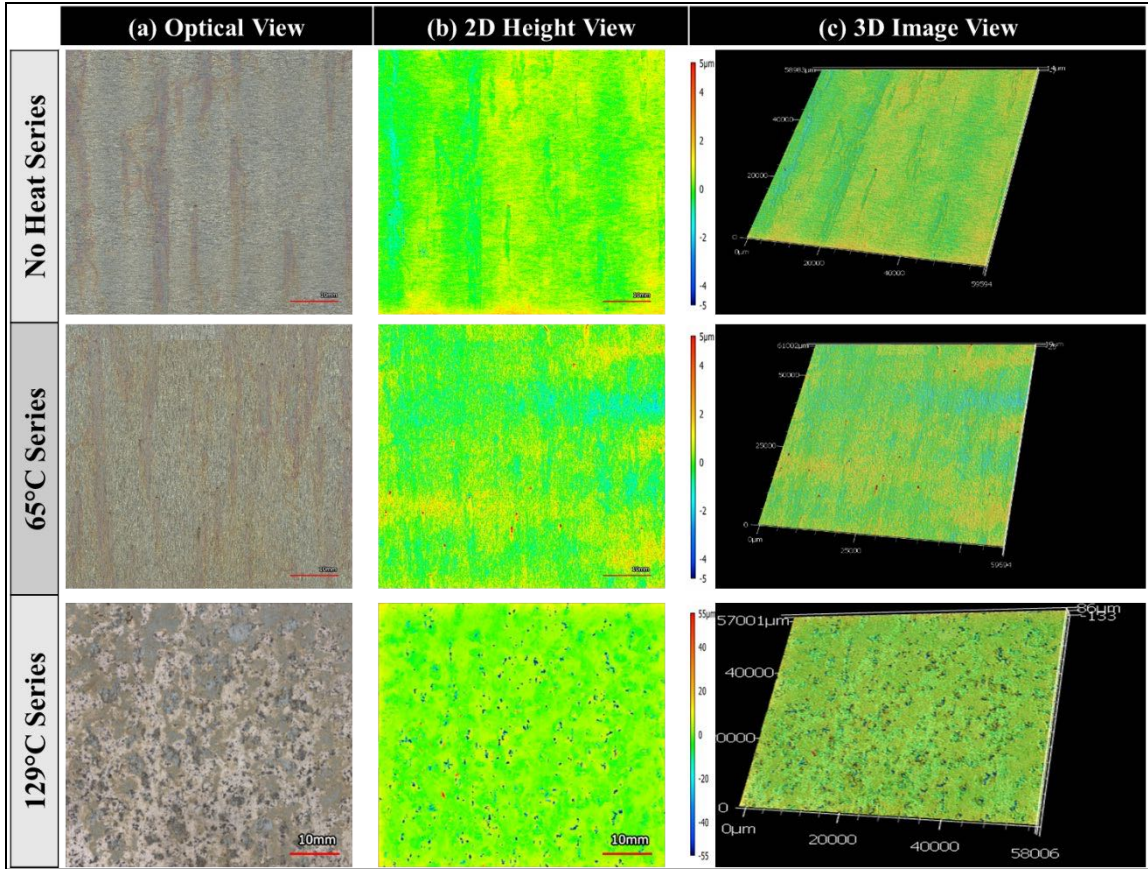
Figure 65: Optical profilometry images of 3 months aged CCC treated Al2219 samples after 168 hours in Neutral Salt Fog 3.5% NaCl (followed by chemical cleaning of corrosion products).

In addition to surface morphology to evaluate general localized pitting the sample series, 3D optical profilometry was used along with roughness profile to access the number, size, and depth of pits. Figure 66 and Figure 67 present the qualitative observations of the pits of fresh CCC treated samples and the three months aged CCC treated samples, respectively. The samples were characterized clearly by the gradient color scaled depths and clear differentiation in pit density and shape can be evaluated. The blue dotted line was used to display a typical example of pit depth found for each sample series. Additionally, the average pit count and average depth values were derived for the sample set based on heat

treatment and compared to the non-coated bare Al2219 panels (Figure 68). Despite the age of the samples, the pitting morphology is consistent by heat treatment. The higher temperate heat treatment had very dense pitting and had areas where some pits merged.
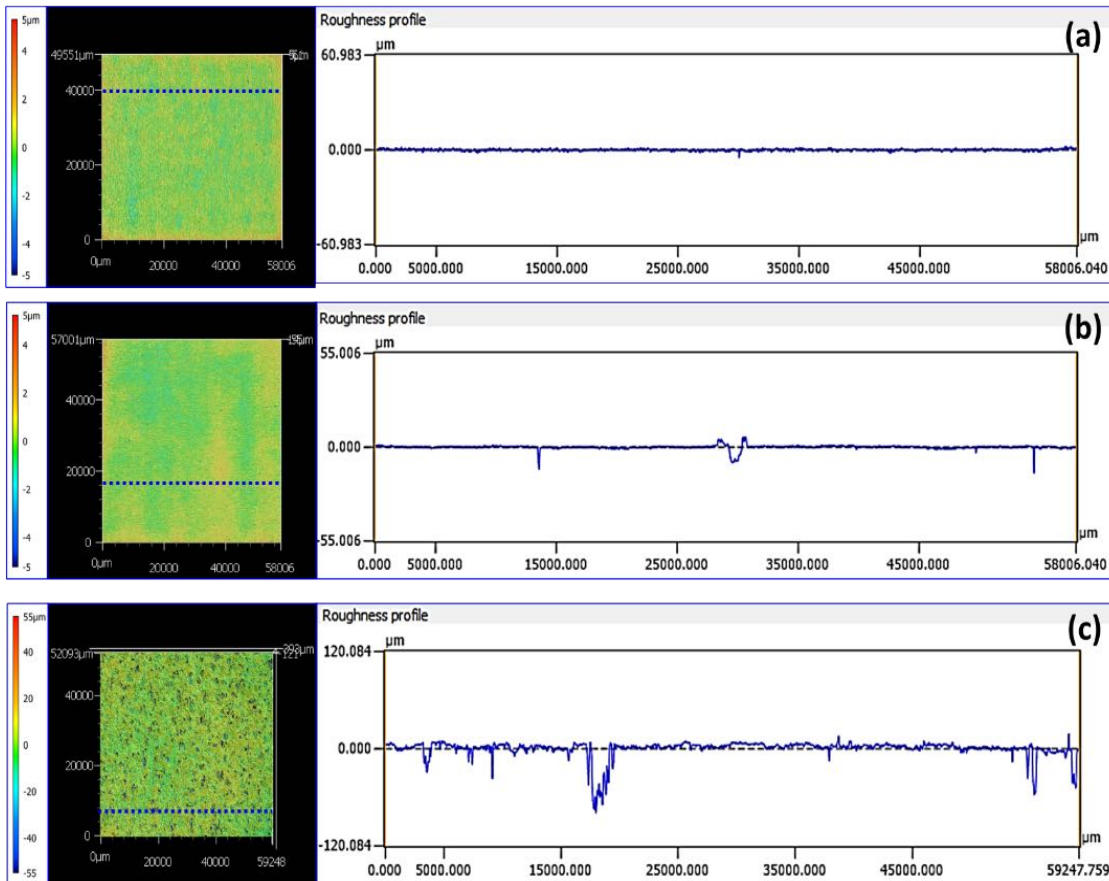
Figure 66: Three-dimensional optical profilometry images and line roughness profiles of pits for the fresh CCC treated Al2219 samples after 168 hours in Neutral Salt Fog 3.5% NaCl. The blue horizontal line highlights the line profiles crossing selected pits in (a) No-Heat series, (b) 65 °C series, and (c) 129°C series.
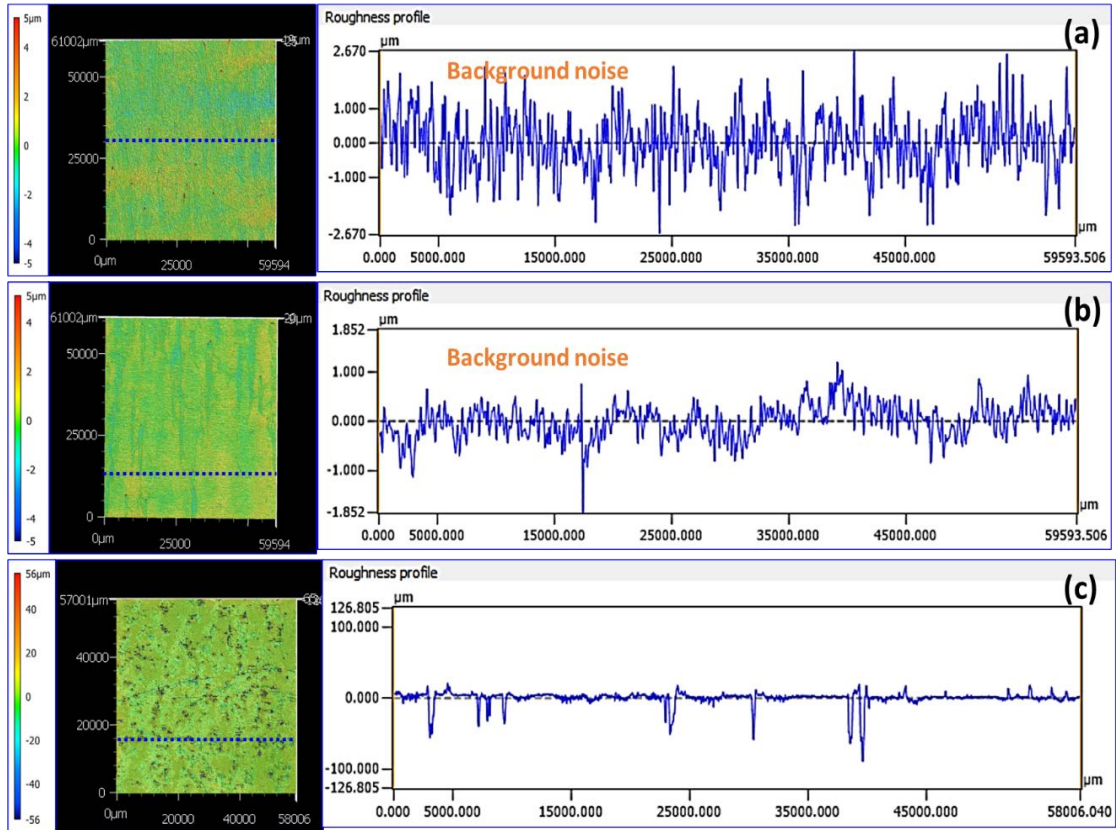
Figure 67: Three-dimensional optical profilometry images and line roughness profiles of pits for the 3 months aged CCC treated Al2219 samples after 168 hours in Neutral Salt Fog 3.5% NaCl. The blue horizontal line highlights the line profiles crossing selected pits in (a) No-Heat series, (b) 65 °C series, and (c) 129°C series.
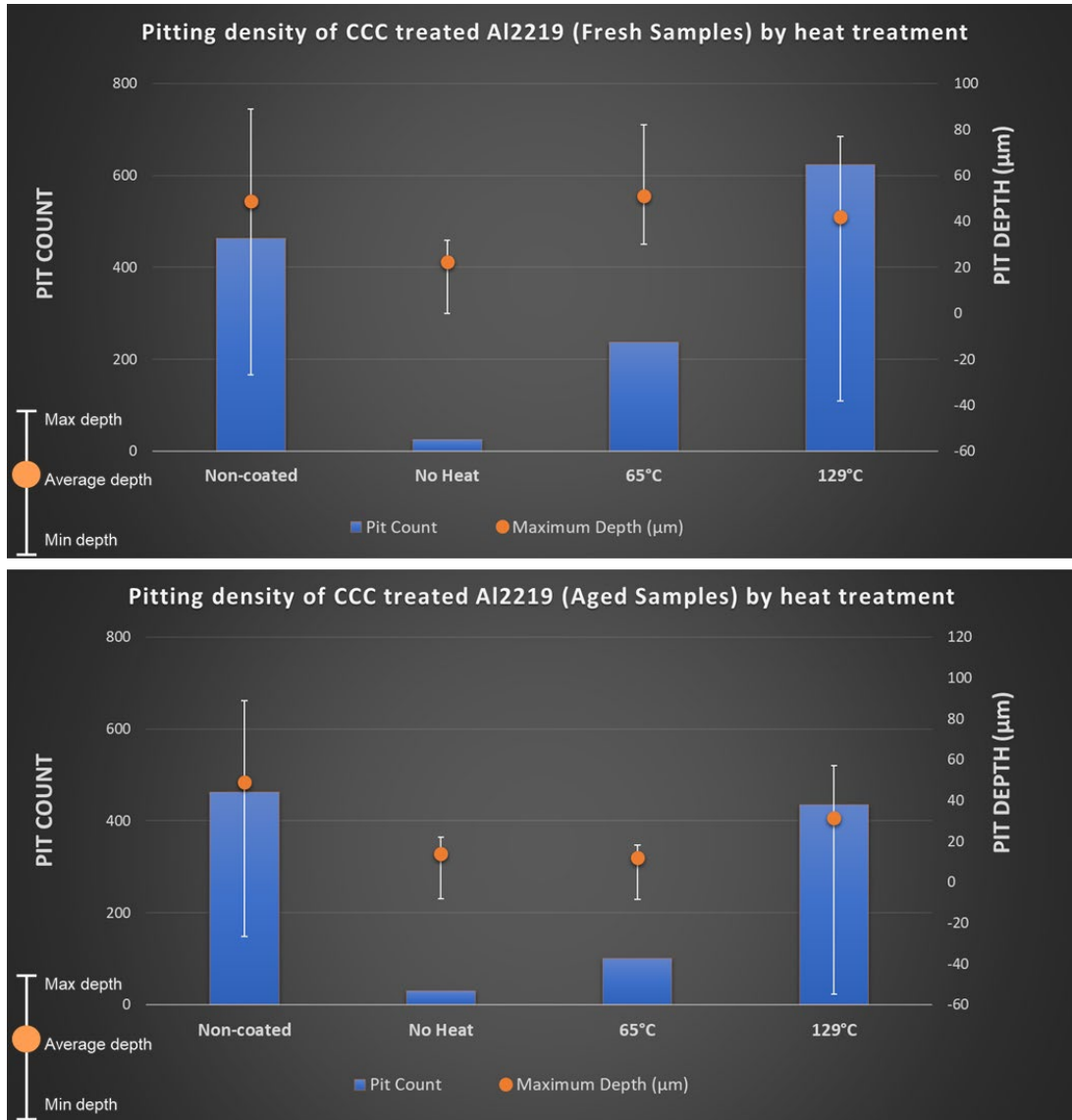
Figure 68: Pitting density evaluation of the (a) fresh and (b) aged CCC treated Al2219 samples after 168 hours in Neutral Salt Fog 3.5% NaCl (followed by chemical cleaning of corrosion products).

Summary of Corrosion Resistance Testing

Regardless of aging, after salt fog exposure of all samples, the corrosion attack was in the form of extended pits. The non-coated, bare Al2219 sample showed severe substrate degradation with pit diameters about 900 μm – 1600 μm observed on the surface. The

CCC treated samples with no-heat-treated samples, showed significant corrosion resistance compared to the non-coated samples. There was no visible corrosion observed on the surface and the coating remained intact. The 129°C heat treated samples were very similar in degradation, pit density, and diameter as the non-coated, bare Al2219 samples. The 65°C heat treated samples performed similarly to the no-heat treated samples. There was only a slight corrosion attack on the surface with minor shallow pitting.

CHAPTER 5

5.0   Discussion

Generally, for majority of corrosion complications, it is assumed that the major contributor is the difference in reaction potentials between two dissimilar substrates. But in fact, the most important reaction potentials exist between the interstitial and barrier layers intermingled all over the surface of a single substrate. These potential differences that occur on the surface of the metal result from local chemical or physical differences within or on the metal, such as variations in grain structure, micro-environments created by inclusions in the metal, grain boundaries, and scratches or other surface conditions. This is the main corrosion issue with alloyed Al2219 as it was seen that both the anodic and cathodic areas created by the alloyed intermetallics lie side by side. During corrosion process of Al2219, the surface is covered in positive and negative sites and based on the localized corrosion that occurs the anodes and cathodes of the substrate will interchange frequently.

For aerospace grade Al2219 substrate, defects are inevitable and their behavior during interactions with chromated conversion coating have yet to be fully understood (102,158,176,177).   One of the major defects is the formation and behavior with intermetallics in which filmed surfaces intersect the surface of the substrate. During surface preparation in the chromating process (etching, de-smutting etc.), the intermetallics have been shown to be removed from the surface and this in turn creates pits initiation points (176). The copper intermetallic in Al2219 play a critical role in the corrosion of aluminum when exposed to a marine, high chloride environment. The metallics create pockets of anodes or cathodes and form galvanic couples throughout the primary aluminum matrix

((28,178)).   The relationship between the copper intermetallics in Al2219 and the conversion coating have not been fully studied in literature. It is important to understand the fundamental relationship between the intermetallics within the Al2219 substrate in order to understand the how the CCC formation on the intermetallics will perform and influence the overall conversion coating performance.

Dehydration

On the basis of the results in the present study it is evident that the dehydration process is about the same with aging at ambient temperatures for three months as to heat treatment to 65°C. The aging and exposure at elevated temperatures effects the CCC structure and properties similarly. The samples 25°C CCC treated series with no-heat treatment showed no evidence of micro-mud-cracking after three months aging. However, the heat-treated 65°C and 129°C CCC treated series showed signs of micro-mud-cracking after three months of aging. These two-sample series also showed signs of mud-cracking features after heat treatment despite aging. Hughes noted that an increase in shrinkage cracking with aging and speculated that loss in oxygen reduction reaction inhibition and corrosion resistance was related to gradual immobilization of Cr6+. Loss in Cr6+ leaching eliminated healing of emerging shrinkage cracks and led to lower corrosion resistance (43,179,180). Overall, the oxygen loss was confirmed. As water is lost, the shrinkage across the coating thickness is different. The water loss in the outer layer is greater than inner layer, thus a tensile stress develops at the coating surface

CCC treated samples 25°C and 65°C

These two sets of samples performed about the same throughout surface characterization no matter the aging. Despite heat treatment to the 65°C series, pitting was nominal and visually resembled the 25°C series. Although, SEM/EDS showed micro-mud-cracking features in the 65°C series sample set. These features were randomly scattered across the sample and were not prominent enough to deem the sample coating discontinuous. Despite this micro feature, the 65°C sample performed almost as well as the 25°C series. Electrochemical analysis showed the corrosion rate to be about 0.05 mpy for the 25°C series and 0.36 mpy for the 65°C series. XPS showed no significant change in chromium concentration between fresh and aged samples.

CCC treated samples 129°C

Comparatively, the 129°C series performed poor despite aging. Aging was not so much a factor for this sample set as heat treatment. Visually, after heat treatment, this sample set lost the iridescent gold color that is attributed to chromated coatings. However, both XPS and SEM/EDS confirmed the presence of chromium on the surface. This series performance closely resembled that of the non-coated samples. After salt fog exposure, the sample series had a very thick alumina on the surface. There was no coating protection afforded the samples despite confirmation via XPS and EDS that the coating was intact. After salt fog exposure, there were large areas of coating degradation and sever mud-cracking features. It can be concluded that at 129°C the chromated conversion coating provides no protection in a high humidity, high salt concentration environment.

A comparative study utilizing SEM/EDS, EIS, XPS and profilometry to evaluate the surface characteristics of the application of chemical conversion coating on Al2219, CCC application as a function of elevated temperature exposure, and CCC degradation as a function of time were all evaluated. SEM/EDS confirmed micro mud-cracking initiation sites and XPS confirmed that the chromated conversion coating appears to give a layer composed of chromium in two different chemical states, Cr(II) in the form of chromium oxide, and Cr(VI) in the form of chromate. Evaluation of the freshly applied CCC with aged CCC application. Impedance decreased with increasing temperature which correlate with the decrease in coating resistance with increasing temperature. Higher heat treatment exhibits more defect sites that allows electrolyte to impinge the substrate which gives less corrosion protection.

Summary of Corrosion Testing:

Regardless of aging, after salt fog exposure of all samples, the corrosion attack was in the form of extended pits. The non-coated, bare Al2219 sample showed severe substrate degradation with pit diameters about 900 μm – 1600 μm observed on the surface. The CCC treated samples with no-heat-treated samples, showed significant corrosion resistance compared to the non-coated samples. There was no visible corrosion observed on the surface and the coating remained intact. The 129°C heat treated samples were very similar in degradation, pit density, and diameter as the non-coated, bare Al2219 samples. The 65°C heat treated samples performed similarly to the no-heat treated samples. There was only a slight corrosion attack on the surface with minor shallow pitting.

Table 10 and Table 11 provides a snapshot summary of the research objectives and how the results accomplished from this study. The summaries of the research objectives for this study were:

RO1.   How does the surface characteristics of chromated conversion coating on Al2219 change with elevated temperatures and storage time in ambient and corrosive environments?

- According to NASA-STD-6012, CCC treated Al2219 cannot be stored longer than 168hours. This research was able to show that the CCC treated Al2219 provided corrosion protection for up to three months even when exposed to elevated temperatures at 65°C.

RO2.   Will the processing temperatures for space flight hardware cause mud-cracking and/or coating degradation in chromated conversion coating on Al2219?

- The mud-cracking feature that is typical of CCC treated Al2219 was not observed in any of the samples that were stored up to 3 months and not heat treated. However, micro mud-cracking was observed after heat treatment in some of the 65 °C samples and was observed in all of the 129 °C samples.

RO3.   What is the maximum applied temperature and exposure time boundaries for

flight component boundaries that will lead to coating degradation in chromated

conversion coating of Al2219?

- Samples handled at room temperature and samples heat treated to 65°C provided

corrosion protection for up to 3 months even after salt fog exposure. However,

Fresh and Aged samples that were heat treated to 129 °C offered no corrosion

protection.

RO4.   What is the effectiveness of the chromated conversion coating of Al2219 in

mitigating corrosion when exposed to a corrosive environment?

- The fresh samples that were heat treated behaved similarly to the no heat

treatment samples. The same trend was seen with the aged samples. Heat

treatment after 3 months up to 65°C did not degrade the coating. However,

129°C for both fresh and age samples provided no corrosion protection of the

substrate

Table 10. Summary and Conclusion of research objectives 01 - 02.
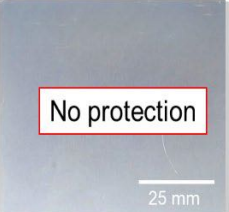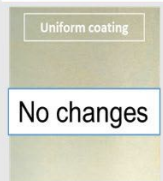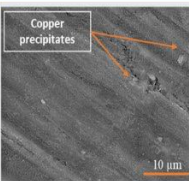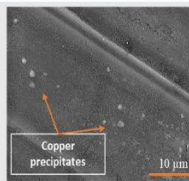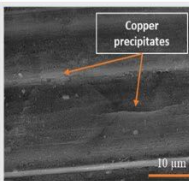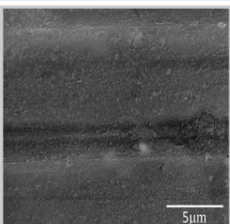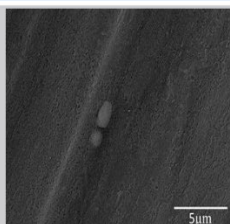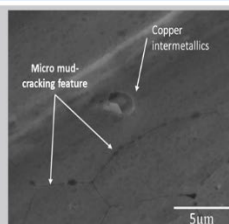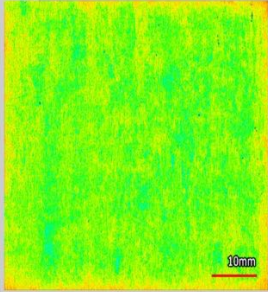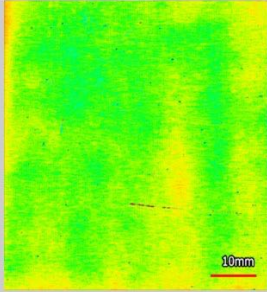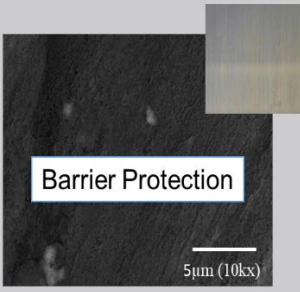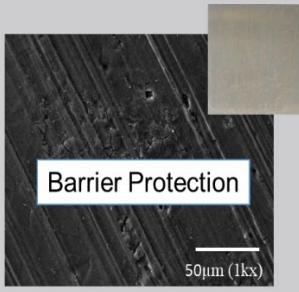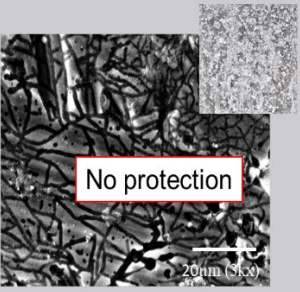
Research Objective	25°C CCC treated Series No heat treatment	65°C CCC treated Series	129°C CCC treated Series
RO1: elevated temperature	No changes	No changes	No protection
RO1: storage (aging)	Initial Sample — Uniform coating — No changes; Day 01 (5000x) — Copper precipitates; Day 30 (5000x) — Copper precipitates; Day 60 (5000x) — Copper precipitates		

Research Objective	25°C CCC treated Series No heat treatment	65°C CCC treated Series	129°C CCC treated Series
RO2: mud-cracking after heat treatment (all 10kx)			Micro mud-cracking feature; Copper intermetallics

Table 11. Summary and Conclusion of research objectives and results 03 - 04.

Research Objective	25°C CCC treated Series No heat treatment	65°C CCC treated Series	129°C CCC treated Series
RO3: max temperature that affords corrosion protection		No protection	No protection
Research Objective	25°C CCC treated Series No heat treatment	65°C CCC treated Series	129°C CCC treated Series
RO4: performance in corrosive environment	Barrier Protection 5μm (10kx)	Barrier Protection 50μm (1kx)	No protection 20nm (5kx)

CHAPTER 6

6.0 Conclusions and Future Work

This research evaluated chromate conversion coating formation and breakdown of intermetallic compounds of heterogeneous Al2219 alloy using flight hardware processing temperatures and storage times. The effect of both temperature and aging in an accelerated corrosive environment on corrosion behavior of the chromate conversion coating performance of Al2219 was characterized. The corrosion study conducted on the Al2219 alloy untreated and treated with CCC lead to the following conclusions:

- The microstructure of the alloys plays an important role in the corrosion resistance of Al2219 alloys. The corrosion behavior is affected by the composition, the dimensions, the homogeneity, and the density of second phase precipitates at the alloy surface. However, Corrosion testing showed that breakdown of the coating appeared to be initiated at copper precipitate sites, indicating that these particles are the weakest points in the coated surface.

- After CCC treatment, despite the cathodic nature of the Al_2Cu intermetallics, CCC appeared uniformed across the surface of the samples.

- Aging does affect CCC Al2219 substrate as micro-initiation sites of mud-cracking was found on the aged samples after heat treatment. However, these micro-initiation sites were not found in the fresh sample that were heat treated to 65°C.

- Elevated heat treatment at 129°C is unacceptable for processing environment for flight hardware

- Elevated heat treatment at 65°C was comparable to the no-heat treatment samples. At 65°C, coating degradation was nominal despite aging.

Future work

In consideration of the results from this research in evaluating CCC treated Al2219 for use at elevated temperatures and after aging, the future work that should be carried out include:

- The continued corrosion analysis of the CCC treated Al2219 samples up to 1-year storage in order to tune in the dehydration time of the CCC as a function of time. This would be greatly beneficial to flight hardware processing.
- Corrosion analysis and surface characterization of the CCC treated Al2219 once the mud-cracking feature becomes uniformed across the surface. In the current study, mud-cracking was not continuous on the surface and was not a major feature prior to salt fog exposure. This feature was found on the surface of the samples after salt fog exposure.
- Extended examination of the CCC treated Al2219 during actual processing of flight hardware, where coatings with high curing temperatures are applied to the CCC treated Al2219.
- Evaluate the degradation of the copper intermetallic locally as a function of heat treatment and corrosion resistance. A better understanding of the micro-environment would help determine the limits of the conversion coating.

References

1.   Nakai M, Eto T. New aspect of development of high strength aluminum alloys for aerospace applications. Materials Science and Engineering A. 2000 Jun 15;285(1–2):62–8.

2.   Committee AH. Properties and Selection: Nonferrous Alloys and Special-Purpose Materials. Properties and Selection: Nonferrous Alloys and Special-Purpose Materials. ASM International; 2018.

3.   NASA Kennedy Images. The crew module for NASA's Artemis II mission [Internet]. 2021 [cited 2021 Oct 2]. Available from: https://www.flickr.com/photos/nasakennedy/51368185845/in/album-72157644988382051/

4.   Ahmad Z. BASIC CONCEPTS IN CORROSION. Principles of Corrosion Engineering and Corrosion Control. 2006 Jan 1;9–56.

5.   Montgomery E. CEL Coatings - Atmospheric Site Data [Internet]. [cited 2019 Jul 1]. Available from: https://corrosion.ksc.nasa.gov/Coatings/AtmosphericSiteData

6.   Montgomery EL, Marina Calle L, Jerome Curran AC, Kolody MR. Timescale Correlation between Marine Atmospheric Exposure and Accelerated Corrosion Testing [Internet]. [cited 2019 Jul 1]. Available from: https://ntrs.nasa.gov/search.jsp?R=20110014389

7.   NASA-STD-6012 | NASA Technical Standards System (NTSS) [Internet]. [cited 2021 Sep 19]. Available from: https://standards.nasa.gov/standard/nasa/nasa-std-6012

8.   Zaludin MAF, Zahid Jamal ZA, Derman MN, Kasmuin MZ. Fabrication of calcium phosphate coating on pure magnesium substrate via simple chemical conversion coating: Surface properties and corrosion performance evaluations. Journal of Materials Research and Technology. 2019;8(1):981–7.

9.   Suzuki Y, Morishita A. Influence of corrosion inhibitor in chemical conversion coatings on corrosion performance in scratches in zinc-coated steels. ISIJ International. 2019;59(10):1878–85.

10.   MacKenzie DS. Heat treating aluminum for aerospace applications. Heat Treating Progress. 2005;5(4):36–43.

11.   Ferreira MGS, Zheludkevich ML, Tedim J, Yasakau KA. Self-healing nanocoatings for corrosion control. In: Corrosion Protection and Control Using Nanomaterials. Elsevier; 2012. p. 213–63.

12. Ferreira MGS, Zheludkevich ML, Tedim J. Advanced protective coatings for aeronautical applications. In: Nanocoatings and Ultra-Thin Films. Elsevier; 2011. p. 235–79.

13. Li L. Corrosion Protection Provided By Trivalent Chromium Process. Thesis. 2013;

14. Dobbins T. Aluminum Alloys 101 | The Aluminum Association [Internet]. [cited 2021 Jan 12]. Available from: https://www.aluminum.org/resources/industry-standards/aluminum-alloys-101

15. National Aeronautics and Space Administration. Super Lightweight External Tank [Internet]. 2003 [cited 2021 Jan 14]. p. 40150. Available from: https://www.nasa.gov/centers/marshall/pdf/100423main_shuttle_external_tank.pdf

16. AA ASD1M - Aluminum standards and data 2017 Metric SI | Engineering360 [Internet]. [cited 2021 Jun 29]. Available from: https://standards.globalspec.com/std/10264210/AA ASD1M

17. Corrosion: Understanding the Basics - ASM International [Internet]. [cited 2021 Jan 16]. Available from: https://www.asminternational.org/search/-/journal_content/56/10192/06691G/PUBLICATION

18. Cramer SD, Covino BS, Henry SD, Assistance E, Marquard E, Lampman H, et al. ASM Handbook Õ Volume 13B Corrosion: Materials Prepared under the direction of the ASM International Handbook Committee [Internet]. Vol. 13. 2005 [cited 2021 Jan 16]. Available from: www.asminternational.orgwww.asminternational.org

19. Huda Z, Taib NI, Zaharinie T. Characterization of 2024-T3: An aerospace aluminum alloy. Materials Chemistry and Physics. 2009;113(2–3).

20. Buchheit RG, Grant RP, Hlava PF, Mckenzie B, Zender GL. Local Dissolution Phenomena Associated with S Phase (Al2CuMg) Particles in Aluminum Alloy 2024-T3. Journal of The Electrochemical Society. 1997 Aug 1;144(8):2621–8.

21. Birbilis N, Buchheit RG. Electrochemical Characteristics of Intermetallic Phases in Aluminum Alloys. Journal of The Electrochemical Society. 2005;152(4):B140.

22. Staszczyk A, Sawicki J, Adamczyk-Cieslak B. A Study of Second-Phase Precipitates and Dispersoid Particles in 2024 Aluminum Alloy after Different Aging Treatments. Materials [Internet]. 2019 Dec 12 [cited 2021 Sep 17];12(24):4168. Available from: /pmc/articles/PMC6947497/

23. Li J, Dang J. A Summary of Corrosion Properties of Al-Rich Solid Solution and Secondary Phase Particles in Al Alloys. Metals 2017, Vol 7, Page 84 [Internet]. 2017 Mar 7 [cited 2021 Sep 17];7(3):84. Available from: www.mdpi.com/2075-4701/7/3/84/htm

24. Zobac O, Kroupa A, Zemanova A, Richter KW. Experimental Description of the Al-Cu Binary Phase Diagram. Metallurgical and Materials Transactions A 2019 50:8 [Internet]. 2019 May 21 [cited 2021 Sep 17];50(8):3805–15. Available from: https://link.springer.com/article/10.1007/s11661-019-05286-x

25. Porter DA, Easterling KE, Sherif MY. Phase transformations in metals and alloys, third edition. Phase Transformations in Metals and Alloys, Third Edition. 2009 Jan 1;1–521.

26. Pereira AM, Pimenta G, Dunn BD. ESA STM-276 Assessment of Chemical Conversion Coatings for the Protection of Aluminium Alloys A Comparison of Alodine 1200 with Chromium-Free Conversion Coatings. 2008.

27. Rooij AD. Bimetallic Compatible Couples. 1999;

28. Chen GS, Gao M, Wei RP. Microconstituent-Induced Pitting Corrosion in Aluminum Alloy 2024-T3. Corrosion (Houston). 1996;52(1):8–15.

29. Davis JR. Aluminum and Aluminum Alloys Introduction and Overview. 2001;

30. Treacy GM, Wilcox GD. Surface analytical study of the corrosion behaviour of chromate passivated Al 2014 A T-6 during salt fog exposure. Applied Surface Science. 2000;157(1):7–13.

31. Kumar K, Margerum DW. Kinetics and Mechanism of General-Acid-Assisted Oxidation of Bromide by Hypochlorite and Hypochlorous Acid. Inorganic Chemistry [Internet]. 1987 Aug 1 [cited 2020 Dec 3];26(16):2706–11. Available from: https://pubs.acs.org/doi/abs/10.1021/ic00263a030

32. Qu W, Song M, Yao J, Zhao H. Effect of temperature and heat treatment status on the ductile fracture toughness of 2219 aluminum alloy. In: Materials Science Forum. 2011.

33. Microconstituent-Induced Pitting Corrosion in Aluminum Alloy 2024-T3 | Corrosion | OnePetro [Internet]. [cited 2021 Sep 19]. Available from: https://onepetro.org/corrosion/article-abstract/113038/Microconstituent-Induced-Pitting-Corrosion-in

34. Corrosion of Aluminum and Aluminum Alloys - ASM International [Internet]. [cited 2021 Jul 4]. Available from: https://www.asminternational.org/technical-books/-/journal_content/56/10192/06787G/PUBLICATION

35. Hassannejad H, Moghaddasi M, Saebnoori E, Baboukani AR. Microstructure, deposition mechanism and corrosion behavior of nanostructured cerium oxide conversion coating modified with chitosan on AA2024 aluminum alloy. Journal of Alloys and Compounds. 2017 Nov 25;725:968–75.

36. The Surface Treatment and Finishing of Aluminum and Its Alloys, 6th Edition - ASM International [Internet]. [cited 2021 Jan 17]. Available from: https://www.asminternational.org/home/-/journal_content/56/10192/06945G/PUBLICATION

37. Jones DRH. Engineering Materials 1. [cited 2021 Sep 17]; Available from: www.books.elsevier.com

38. Liu Y, Skeldon P, Thompson GE, Habazaki H, Shimizu K. Chromate conversion coatings on aluminium-copper alloys. Corrosion Science. 2005 Feb 1;47(2):341–54.

39. Liu Y, Skeldon P, Thompson GE, Habazaki H, Shimizu K. Chromate conversion coatings on aluminium-copper alloys. Corrosion Science. 2005 Feb;47(2):341–54.

40. Ilevbare GO. Inhibition of pitting corrosion on aluminum alloy 2024-T3: Effect of soluble chromate additions vs chromate conversion coating. Corrosion. 2000;56(3):227–42.

41. Ilevbare GO, Schneider O, Kelly RG, Scully JR. In Situ Confocal Laser Scanning Microscopy of AA 2024-T3 Corrosion Metrology: I. Localized Corrosion of Particles. Journal of The Electrochemical Society [Internet]. 2004 Jun 25 [cited 2021 Sep 17];151(8):B453. Available from: https://iopscience.iop.org/article/10.1149/1.1764780

42. Boag A, Hughes AE, Glenn AM, Muster TH, McCulloch D. Corrosion of AA2024-T3 Part I: Localised corrosion of isolated IM particles. Corrosion Science. 2011 Jan 1;53(1):17–26.

43. Hughes AE. Conversion Coatings. In: Encyclopedia of Interfacial Chemistry: Surface Science and Electrochemistry. Elsevier; 2018. p. 108–14.

44. Kowal K, DeLuccia J, Josefowicz JY, Laird C, Farrington GC. In Situ Atomic Force Microscopy Observations of the Corrosion Behavior of Aluminum-Copper Alloys. Journal of The Electrochemical Society [Internet]. 1996 Aug 1 [cited 2021 Sep 17];143(8):2471. Available from: https://iopscience.iop.org/article/10.1149/1.1837033

45. Zhu Y, Sun K, Frankel GS. Intermetallic Phases in Aluminum Alloys and Their Roles in Localized Corrosion. Journal of The Electrochemical Society [Internet]. 2018 Aug 28 [cited 2021 Sep 17];165(11):C807. Available from: https://iopscience.iop.org/article/10.1149/2.0931811jes

46. Srinivasan R, Fasmin F. An Introduction to Electrochemical Impedance Spectroscopy. An Introduction to Electrochemical Impedance Spectroscopy [Internet]. 2021 Mar 8 [cited 2021 Jul 7]; Available from: https://www-taylorfrancis-com.ezproxy.fiu.edu/books/mono/10.1201/9781003127932/introduction-electrochemical-impedance-spectroscopy-ramanathan-srinivasan-fathima-fasmin

47. Srinivasa Rao K, Prasad Rao K. PITTING CORROSION OF HEAT-TREATABLE ALUMINIUM ALLOYS AND WELDS: A REVEIW. Trans Indian Inst Met [Internet]. 2004 Dec [cited 2021 Sep 17];57(6):593–610. Available from: http://www.igcar.gov.in/transiim/2004/vol57-6review.pdf

48. Rao GS, Rao VVS, Rao SRK. Mechanical and corrosion properties of friction stir welded joints of Al-Cu alloy 2219-T87. Materialpruefung/Materials Testing. 2015;57(9).

49. Kosari A, Tichelaar F, Visser P, Zandbergen H, Terryn H, Mol JMC. Dealloying-driven local corrosion by intermetallic constituent particles and dispersoids in aerospace aluminium alloys. Corrosion Science. 2020 Dec 1;177:108947.

50. Kosari A, Visser P, Tichelaar F, Eswara S, Audinot JN, Wirtz T, et al. Cross-sectional characterization of the conversion layer formed on AA2024-T3 by a lithium-leaching coating. Applied Surface Science [Internet]. 2020;512(February):145665. Available from: https://doi.org/10.1016/j.apsusc.2020.145665

51. MIL-DTL-5541F Chemical Conversion Coatings on Aluminum and Aluminum Alloys [Internet]. 2006 [cited 2021 Jan 16]. Available from: http://www.astm.org.

52. Xia L. Formation and Function of Chromate Conversion Coating on Aircraft Aluminum Alloy Probed by Vibrational Spectroscopy. 2000.

53. Campestrini P, Terryn H, Vereecken J, de Wit JHW. Chromate Conversion Coating on Aluminum Alloys. Journal of The Electrochemical Society. 2004;151(6):B370.

54. Zhang W, Hurley B, Buchheit RG. Characterization of Chromate Conversion Coating Formation and Breakdown Using Electrode Arrays. Journal of The Electrochemical Society [Internet]. 2002 Jun 12 [cited 2021 Jan 17];149(8):B357. Available from: https://iopscience.iop.org/article/10.1149/1.1485774

55. Balaraju JN. Assessment of chromate and chromate-free conversion coatings for the corrosion protection of aerospace aluminum alloy.

56. Gharbi O, Thomas S, Smith C, Birbilis N. Chromate replacement: what does the future hold? npj Materials Degradation [Internet]. 2018 Dec 12 [cited 2021 Jan 16];2(1):12. Available from: www.nature.com/npjmatdeg

57. Nordlien JH, Walmsley JC, Østerberg H, Nisancioglu K. Formation of a zirconium-titanium based conversion layer on AA 6060 aluminium. Surface and Coatings Technology. 2002 Apr 1;153(1):72–8.

58. Sato N. 1989 Whitney Award Lecture: Toward a More Fundamental Understanding of Corrosion Processes. Corrosion [Internet]. 1989 May 1 [cited 2021 Sep 19];45(5):354–68. Available from: http://meridian.allenpress.com/corrosion/article-pdf/45/5/354/1530050/1_3582030.pdf

59. SAKASHITA M, SATO N. Ion Selectivity of Precipitate Films Affecting Passivation and Corrosion of Metals. Corrosion [Internet]. 1979 Aug 1 [cited 2021 Sep 19];35(8):351–5. Available from: http://meridian.allenpress.com/corrosion/article-pdf/35/8/351/1526248/0010-9312-35_8_351.pdf

60. L Xia RM. Chemistry of a chromate conversion coating on aluminum alloy AA2024-T3 probed by vibrational spectroscopy. J Electrochem Soc. 1998 Sep 1;145(9):3083–9.

61. Yoganandan G, Pradeep Premkumar K, Balaraju JN. Evaluation of corrosion resistance and self-healing behavior of zirconium-cerium conversion coating developed on AA2024 alloy. Surface and Coatings Technology. 2015 May 25;270:249–58.

62. Guseva O, Derose JA, Schmutz P. Modelling the early stage time dependence of localised corrosion in aluminium alloys. Electrochimica Acta. 2013;88:821–31.

63. Gupta RK, Sukiman NL, Cavanaugh MK, Hinton BRW, Hutchinson CR, Birbilis N. Metastable pitting characteristics of aluminium alloys measured using current transients during potentiostatic polarisation. Electrochimica Acta. 2012 Apr 1;66:245–54.

64. Serdechnova M, Volovitch P, Brisset F, Ogle K. On the cathodic dissolution of Al and Al alloys. Electrochimica Acta. 2014 Apr 1;124:9–16.

65. Cragnolino G, Sridhar N. A REVIEW OF LOCALIZED CORROSION OF HIGH-LEVEL NUCLEAR WASTE Center for Nuclear Waste Regulatory Analyses. 1991;

66. Buchheit RG, Mamidipally SB, Schmutz P, Guan H. Active corrosion protection in Ce-modified hydrotalcite conversion coatings. Corrosion. 2002;58(1):3–14.

67. Kendig M, Jeanjaquet S, Addison R, Waldrop J. Role of hexavalent chromium in the inhibition of corrosion of aluminum alloys. Surface and Coatings Technology. 2001 May 22;140(1):58–66.

68. Inhibition of Pitting Corrosion on Aluminum Alloy 2024-T3: Effect of Soluble Chromate Additions vs Chromate Conversion Coating | Corrosion | OnePetro [Internet]. [cited 2021 Sep 19]. Available from: https://onepetro.org/corrosion/article-abstract/111595/Inhibition-of-Pitting-Corrosion-on-Aluminum-Alloy

69. Kendig MW, Davenport AJ, Isaacs HS. The mechanism of corrosion inhibition by chromate conversion coatings from x-ray absorption near edge spectroscopy (Xanes). Corrosion Science. 1993 Jan 1;34(1):41–9.

70. Chidambaram D, Halada GP, Clayton CR. Spectroscopic Elucidation of the Repassivation of Active Sites on Aluminum by Chromate Conversion Coating. Electrochemical and Solid-State Letters [Internet]. 2004 Jul 23 [cited 2021 Sep 19];7(9):B31. Available from: https://iopscience.iop.org/article/10.1149/1.1775972

71. Xia L, Akiyama E, Frankel G, McCreery R. Storage and Release of Soluble Hexavalent Chromium from Chromate Conversion Coatings Equilibrium Aspects of Cr VI Concentration. Journal of The Electrochemical Society [Internet]. 2000 Jul 1 [cited 2021 Sep 19];147(7):2556. Available from: https://iopscience.iop.org/article/10.1149/1.1393568

72. Ramsey JD, Xia L, Kendig MW, McCreery RL. Raman spectroscopic analysis of the speciation of dilute chromate solutions. Corrosion Science. 2001 Aug 1;43(8):1557–72.

73. Staroselsky A. Damage and cracking morphology. Advances in Fatigue, Fracture and Damage Assessment of Materials. 2005. 15–53.

74. Dehydration-Induced Loss of Corrosion Protection Properties in Chromate Conversion Coatings on Aluminum Alloy 2024-T3. 2003;

75. Yang Guo B, Frankel G, Rudy Buchheit Sheikh Akbar A. A Study of Trivalent Chrome Process Coatings on Aluminum Alloy 2024-T3.

76. Dong X, Wang P, Argekar S, Schaefer DW. Structure and composition of trivalent chromium process (TCP) films on Al alloy. Langmuir. 2010 Jul 6;26(13):10833–41.

77. Proença CS, Pereira AM, Cabral AM, Pigliaru L, Rohr T, Araújo MEM, et al. Trivalent chromium conversion coating on AA2024-T3 used in aeronautical and aerospace industry. Surface and Interface Analysis. 2019 Dec 1;51(12):1298–311.

78. Characterization of wear damage in coatings by optical profilometry | SpringerLink [Internet]. [cited 2021 Sep 19]. Available from: https://link.springer.com/article/10.1007/BF02645866

79. Dallaire S, Dufour M, Gauthier B. Characterization of wear damage in coatings by optical profilometry. Journal of Thermal Spray Technology 1993 2:4 [Internet]. 1993 [cited 2021 Sep 19];2(4):363–8. Available from: https://link.springer.com/article/10.1007/BF02645866

80. Instant 3D Measurement Over a Wide Area | Wide-Area 3D Measurement System VR-5000 | KEYENCE America [Internet]. [cited 2021 Sep 19]. Available from: https://www.keyence.com/ss/products/measure-sys/vr/

81. Qi J, Němcová A, Walton JR, Zhou X, Skeldon P, Thompson GE. Influence of pre- and post-treatments on formation of a trivalent chromium conversion coating on AA2024 alloy. Thin Solid Films. 2016 Oct 1;616:270–8.

82. Shi H, Han EH, Liu F, Kallip S. Protection of 2024-T3 aluminium alloy by corrosion resistant phytic acid conversion coating. Applied Surface Science. 2013;280.

83. Calabrese L, Bonaccorsi L, Caprì A, Proverbio E. Electrochemical behavior of hydrophobic silane–zeolite coatings for corrosion protection of aluminum substrate. Journal of Coatings Technology and Research. 2014 Oct 24;11(6):883–98.

84. Grilli R, Baker MA, Dunn B, Watts JF. Failure characteristics of adhesively bonded aluminium for spacecraft applications. In: Surface and Interface Analysis. 2008. p. 132–6.

85. Grilli R, Baker MA, Castle JE, Dunn B, Watts JF. CORROSION BEHAVIOUR OF A 2219 ALUMINIUM ALLOY TREATED WITH A CHROMATE CONVERSION COATING EXPOSED TO A 3.5 % NaCl SOLUTION.

86. MW Kendig RB. Corrosion inhibition of aluminum and aluminum alloys by soluble chromates, chromate coatings, and chromate-free coatings. Corrosion. 2003;59(5):379–400.

87. Hughes AE, Taylor RJ, Hinton BRW. Chromate conversion coatings on 2024 Al alloy. Surface and Interface Analysis [Internet]. 1997 Apr 1 [cited 2021 Jan 17];25(4):223–34. Available from: https://onlinelibrary.wiley.com/doi/full/10.1002/%28SICI%291096-9918%28199704%2925%3A4%3C223%3A%3AAID-SIA225%3E3.0.CO%3B2-D

88. Murase M, Watts JF. XPS study of coating delamination from non-rinse chromate treated steel. Journal of Materials Chemistry [Internet]. 1998 Jan 1 [cited 2021 Jul 4];8(4):1007–18. Available from: https://pubs.rsc.org/en/content/articlelanding/1998/jm/a708929e

89. Watts JF, Wolstenholme J. An Introduction to Surface Analysis by XPS and AES. United Kingdom: Wiley; 2019.

90. Murase M, Watts JF. XPS study of coating delamination from non-rinse chromate treated steel. Journal of Materials Chemistry [Internet]. 1998 Jan 1 [cited 2021 Jul 4];8(4):1007–18. Available from: https://pubs.rsc.org/en/content/articlehtml/1998/jm/a708929e

91. NMCF X-ray Instrumentation for Bulk (XRD, XRF, XCT) and Surface (XPS) Characterization | University of Virginia School of Engineering and Applied Science [Internet]. [cited 2021 Sep 19]. Available from: https://engineering.virginia.edu/news/2018/04/nmcf-x-ray-instrumentation-bulk-xrd-xrf-xct-and-surface-xps-characterization#accordion282110

92. Schematic representation of the XPS process. On the left, | Download Scientific Diagram [Internet]. [cited 2021 Sep 19]. Available from: https://www.researchgate.net/figure/Schematic-representation-of-the-XPS-process-On-the-left_fig1_339140872

93. Baer DR, Artyushkova K, Brundle CR, Castle JE, Engelhard MH, Gaskell KJ, et al. Practical Guides for X-Ray Photoelectron Spectroscopy (XPS): First Steps in planning, conducting and reporting XPS measurements. Journal of vacuum science & technology A, Vacuum, surfaces, and films : an official journal of the American Vacuum Society [Internet]. 2019 May [cited 2021 Jul 10];37(3):031401. Available from: /pmc/articles/PMC6774202/

94. Hüfner S. Introduction and Basic Principles. 2003;1–60.

95. Schematic representation of an XPS system. | Download Scientific Diagram [Internet]. [cited 2021 Sep 19]. Available from: https://www.researchgate.net/figure/Schematic-representation-of-an-XPS-system_fig1_309459231

96. Moulder JF, Stickle WF, Sobol PE', Bomben KD, Chastain J. Handbook of X-ray Photoelectron Spectroscopy AReference Book of Standard Spectra for Identification and Interpretation of XPS Data.

97. Skoog DA, Holler FJ, Crouch SR. Calibration of Instrumental Methods. Principles of Instrumental Analysis [Internet]. 2017 [cited 2021 Sep 19];15. Available from: https://books.google.com.sg/books?id=D13EDQAAQBAJ

98. Watts JF, Wolstenholme J. An Introduction to Surface Analysis by XPS and AES. An Introduction to Surface Analysis by XPS and AES [Internet]. 2003 Mar 25 [cited 2021 Sep 19]; Available from: https://onlinelibrary.wiley.com/doi/book/10.1002/0470867930

99. Campestrini P, van Westing EPM, de Wit JHW. Influence of surface preparation on performance of chromate conversion coatings on Alclad 2024 aluminium alloy - Part I: Nucleation and growth. Electrochimica Acta. 2001 May 1;46(16):2553–71.

100. Sun X, Li R, Wong KC, Mitchell KAR, Foster T. Surface effects in chromate conversion coatings on 2024-T3 aluminum alloy. Journal of Materials Science 2001 36:13 [Internet]. 2001 Jul 1 [cited 2021 Sep 17];36(13):3215–20. Available from: https://link.springer.com/article/10.1023/A:1017986319654

101. Lunder O, Walmsley JC, MacK P, Nisancioglu K. Formation and characterisation of a chromate conversion coating on AA6060 aluminium. Corrosion Science. 2005 Jul;47(7):1604–24.

102. Lunder O, Walmsley JC, MacK P, Nisancioglu K. Formation and characterisation of a chromate conversion coating on AA6060 aluminium. Corrosion Science. 2005 Jul 1;47(7):1604–24.

103. Mol JMC, Hughes AE, Hinton BRW, van der Zwaag S. A morphological study of filiform corrosive attack on chromated and alkaline-cleaned AA2024-T351 aluminium alloy. Corrosion Science. 2004 May;46(5):1201–24.

104. Meng Q, Frankel GS. Characterization of chromate conversion coating on AA7075-T6 aluminum alloy. Surface and Interface Analysis. 2004 Jan;36(1):30–42.

105. Grilli R, Baker MA, Castle JE, Dunn B, Watts JF. Corrosion behaviour of a 2219 aluminium alloy treated with a chromate conversion coating exposed to a 3.5% NaCl solution. Corrosion Science. 2011 Apr 1;53(4):1214–23.

106. Sarvghad-Moghaddam M, Parvizi R, Davoodi A, Haddad-Sabzevar M, Imani A. Establishing a correlation between interfacial microstructures and corrosion initiation sites in Al/Cu joints by SEM-EDS and AFM-SKPFM. Corrosion Science. 2014 Feb 1;79:148–58.

107. Castejón OJ. Sample Preparation Methods for Scanning Electron Microscopy. Scanning Electron Microscopy of Cerebellar Cortex. 2003;1–24.

108. Ul-Hamid A. Components of the SEM. A Beginners' Guide to Scanning Electron Microscopy. 2018;15–76.

109. TESCAN MAGNA - High-resolution and high-contrast imaging | TESCAN [Internet]. [cited 2021 Sep 19]. Available from: https://www.tescan.com/product/sem-for-materials-science-tescan-magna/

110. Kanani M, Danaee I, Maddahy MH. Microstructural characteristics and corrosion behavior of cerium oxide conversion coatings on AA6063. Materials and Corrosion [Internet]. 2014 Nov 1 [cited 2021 Sep 19];65(11):1073–9. Available from: https://onlinelibrary.wiley.com/doi/full/10.1002/maco.201307539

111. Ul-Hamid A. A Beginners' Guide to Scanning Electron Microscopy. A Beginners' Guide to Scanning Electron Microscopy. 2018;

112. Campestrini P, Goeminne G, Terryn H, Vereecken J, de Wit JHW. Chromate Conversion Coating on Aluminum Alloys. Journal of The Electrochemical Society. 2004;151(2):B59.

113. Schram T, de Laet J, Terryn H. Nondestructive Optical Characterization of Chemical Conversion Coatings on Aluminum. Journal of The Electrochemical Society. 1998;145(8).

114. Tran VN, Ooi A, Tada E, Nishikata A. EIS Characteristics of Galvanic Couple of Aluminum Alloy and High-strength Steel under Thin Solution Films. Journal of The Electrochemical Society [Internet]. 2020 Oct 5 [cited 2020 Nov 15];167(13):131507. Available from: https://iopscience.iop.org/article/10.1149/1945-7111/abbb44

115. Zhang W. FORMATION AND CORROSION INHIBITION MECHANISMS OF CHROMATE CONVERSION COATINGS ON ALUMINUM AND AA2024-T3.

116. Li XW, Zhang DT, Qiu C, Zhang W. Microstructure and mechanical properties of dissimilar pure copper/1350 aluminum alloy butt joints by friction stir welding. Transactions of Nonferrous Metals Society of China (English Edition). 2012;22(6):1298–306.

117. Munson CA, McFall-Boegeman SA, Swain GM. Cross comparison of TCP conversion coating performance on aluminum alloys during neutral salt-spray and thin-layer mist accelerated degradation testing. Electrochimica Acta. 2018 Aug 20;282:171–84.

118. Corrosion engineering [by] Mars G. Fontana [and] Norbert D. Greene. (Book, 1967) [WorldCat.org] [Internet]. [cited 2021 Sep 18]. Available from: https://www.worldcat.org/title/corrosion-engineering-by-mars-g-fontana-and-norbert-d-greene/oclc/859821020

119. Stern M, Geary AL. Electrochemical Polarization: I . A Theoretical Analysis of the Shape of Polarization Curves. Journal of The Electrochemical Society [Internet]. 1957 Jan 1 [cited 2021 Sep 18];104(1):56. Available from: https://iopscience.iop.org/article/10.1149/1.2428496

120. Stern M, Geary AL. Electrochemical Polarization: I . A Theoretical Analysis of the Shape of Polarization Curves. Journal of The Electrochemical Society [Internet]. 1957 Jan 1 [cited 2021 Sep 18];104(1):56. Available from: https://iopscience.iop.org/article/10.1149/1.2428496

121. Matysik S, Matysik FM, Schulze KD, Einicke WD. Impedance spectroscopic investigations of zeolite–polydimethylsiloxane electrodes. Electrochimica Acta. 2002 Dec 20;48(4):297–301.

122. RIBEIRO DV, SOUZA CAC, ABRANTES JCC. Use of Electrochemical Impedance Spectroscopy (EIS) to monitoring the corrosion of reinforced concrete. Revista IBRACON de Estruturas e Materiais [Internet]. 2015 Aug [cited 2021 Sep 16];8(4):529–46. Available from: http://www.scielo.br/j/riem/a/3FMqWgfrgzzRxVpRjzchvMD/?lang=en

123. Electrochemical Methods: Fundamentals and Applications, 2nd Edition | Sigma-Aldrich [Internet]. [cited 2020 Dec 7]. Available from: https://www.sigmaaldrich.com/catalog/product/aldrich/z511854?lang=en&region=US

124. Basics of EIS: Electrochemical Research-Impedance [Internet]. [cited 2021 Sep 19]. Available from: https://www.gamry.com/application-notes/EIS/basics-of-electrochemical-impedance-spectroscopy/

125. Choi W, Shin H-C, Kim JM, Choi J-Y, Yoon W-S. Modeling and Applications of Electrochemical Impedance Spectroscopy (EIS) for Lithium-ion Batteries. J Electrochem Sci Technol [Internet]. [cited 2021 Sep 19];2020(1):1–13. Available from: https://doi.org/10.33961/jecst.2019.00528

126. EIS Models - Gamry Echem Analyst-Model Editor [Internet]. [cited 2021 Sep 19]. Available from: https://www.gamry.com/application-notes/EIS/user-defined-components-for-eis-modeling/

127. Chen S, Zhang S, Ren X, Xu S, Yin L. Cerium-based chemical conversion coating on aluminum alloy to inhibits corrosion in chloride solution. International Journal of Electrochemical Science. 2015;10(11).

128. Qi K. The Protection Performance of Polypyrrole Coating Doped with Different Counter Anions for the Corrosion of NiTi Alloy. The Open Corrosion Journal. 2011 Mar 30;4(1):18–26.

129. ASTM D1141-98(2021) | Techstreet Enterprise [Internet]. [cited 2021 Sep 19]. Available from: https://subscriptions.techstreet.com/products/903709

130. ASTM D1193-06(2018) | Standard Specification for Reagent Water [Internet]. [cited 2021 Sep 19]. Available from: https://subscriptions.techstreet.com/products/780901

131. Saillard R, Viguier B, Odemer G, Pugliara A, Fori B, Blanc C. Influence of the microstructure on the corrosion behaviour of 2024 aluminium alloy coated with a trivalent chromium conversion layer. Corrosion Science. 2018 Sep 1;142:119–32.

132. Niu LQ, Li XY, Zhang L, Liang XB, Li M. Correlation between microstructure and mechanical properties of 2219-T8 aluminum alloy joints by VPTIG welding. Acta Metallurgica Sinica (English Letters). 2017;30(5).

133. ALECK B. Fiberglass- overwrapped 2219- T87 aluminum alloy low- pressure cryogenic tankage. Space Shuttle Materials. 3.

134. Tiryakioĝlu M, Shuey RT. Quench sensitivity of 2219-T87 aluminum alloy plate. Materials Science and Engineering A. 2010;527(18–19).

135. Wang C, Qu W, Yao J, Zhao H. Microstructures and mechanical properties of friction stir welded 2219-T87 aluminum alloy joints. Hanjie Xuebao/Transactions of the China Welding Institution. 2010 Oct;31(10).

136. Zhao J, Frankel G, McCreery RL. Corrosion Protection of Untreated AA-2024-T3 in Chloride Solution by a Chromate Conversion Coating Monitored with Raman Spectroscopy. Journal of The Electrochemical Society [Internet]. 1998 Jul 1 [cited 2021 Jan 17];145(7):2258–64. Available from: https://iopscience.iop.org/article/10.1149/1.1838630

137. Understanding the Aluminum Temper Designation System. 2000 [cited 2021 Jul 6]; Available from: www.asminternational.org

138. Shirvani K, Mastali S. Effect of Grain Refinement and Immersion Time on Morphology, Topography and Corrosion Resistance of CCC-Coated 7075 Al Alloy. Journal of The Electrochemical Society. 2011;159(2):C74–9.

139. Ketcham SJ, Brown SR. OHRMAT CONVERSION COATING OF ALUMINUM ALLOYS Department of the Navy. 1975;

140. GUO Y. A Study of Trivalent Chrome Process Coatings on Aluminum Alloy 2024-T3. 2011; Available from: https://etd.ohiolink.edu/ap:10:0:::10:P10_ACCESSION_NUM:osu1308166499

141. Grilli R. Conversion coatings for aluminium alloys : a surface investigation for corrosion. 2010;(March):220.

142. Ambrosio MRD. EFFECTS OF HEATING CHROMATE DEPARTMENT OF THE ARMY. 1966;

143. Al-Badour FA, Adesina AY, Ibrahim AB, Suleiman RK, Merah N, Sorour AA. Electrochemical investigation of the effect of process parameters on the corrosion behavior of aluminum-cladded pressure vessel steel using a friction stir diffusion cladding process. Metals. 2020;10(5).

144. Chromate Degradation Mechanisms.pdf.

145. Shirvani K, Mastali S. Effect of Grain Refinement and Immersion Time on Morphology, Topography and Corrosion Resistance of CCC-Coated 7075 Al Alloy. Journal of The Electrochemical Society. 2011;159(2):C74–9.

146. Meng Q. Effect of Cu content on corrosion behavior and chromate conversion coating protection of 7xxx series Al alloys. Vol. PV 2004-14, Proceedings - Electrochemical Society. 2005. p. 173–86.

147. Pereira AM, Pimenta G, Dunn BD. Assessment of chemical conversion coatings for the protection of aluminium alloys: A comparison of alodine 1200 with chromium-free conversion coatings. European Space Agency (Scientific and Technical Memoranda) ESA STM. 2008;(276):1–64.

148. Burnett A, Chen L, Liu K. Galvanic corrosion mechanism and suppressed solution on Al/Cu pads. Proceedings of the International Symposium on the Physical and Failure Analysis of Integrated Circuits, IPFA. 2015;2015-Augus(142):259–62.

149. Sharma VMJ, Kumar KS, Rao BN, Pathak SD. Effect of microstructure and strength on the fracture behavior of AA2219 alloy. Materials Science and Engineering A. 2009;502(1–2):45–53.

150. Walock M. Nanocomposite coatings based on quaternary metalnitrogen. University of Alabama at Birmingham. 2012;189.

151. Qi J, Němcová A, Walton JR, Zhou X, Skeldon P, Thompson GE. Influence of pre- and post-treatments on formation of a trivalent chromium conversion coating on AA2024 alloy. Thin Solid Films. 2016;616:270–8.

152. Gupta RK, Zhang R, Davies CHJ, Birbilis N. Theoretical study of the influence of microalloying on sensitization of AA5083 and moderation of sensitization of a model Al-Mg-Mn alloy via Sr additions. Corrosion. 2014;70(4):402–13.

153. Choudhary B, Paul D, Singh A, Gupta T. Removal of hexavalent chromium upon interaction with biochar under acidic conditions: mechanistic insights and application. Environmental Science and Pollution Research. 2017;24(20):16786–97.

154. Liu Y, Skeldon P, Thompson GE, Habazaki H, Shimizu K. Chromate conversion coatings on aluminium-copper alloys. Corrosion Science. 2005;47(2):341–54.

155. Centre T. The corrosion properties of Spacelab structural alloy. 1984;(May).

156. Goh CS, Chong WLE, Lee TK, Breach C. Corrosion study and intermetallics formation in gold and copper wire bonding in microelectronics packaging. Crystals. 2013;3(3):391–404.

157. Huggett DJ, Dewan MW, Wahab MA, Okeil A, Liao TW. Phased Array Ultrasonic Testing for Post-Weld and OnLine Detection of Friction Stir Welding Defects. Research in Nondestructive Evaluation. 2017;28(4).

158. Oki M. Microstructural and Compositional Characterisation of Chromate Pretreatment on Aluminium. ISRN Materials Science. 2013;2013:1–5.

159. Kaufman JG. Understanding the Aluminum Temper Designation System. Introduction to Aluminum Alloys and Tempers. 2000;39–76.

160. Liu Y, Zhang XM, Li HZ, Liu B, Gao H, Li HJ. Tensile properties of three kinds of aluminum alloys at low temperature. Jinshu Rechuli/Heat Treatment of Metals. 2007;32(1).

161. ASTM B449-93(2015) Standard Specification for Chromates on Aluminum [Internet]. [cited 2021 Sep 19]. Available from: https://subscriptions.techstreet.com/products/683211

162. Chromate Conversion Coatings | Aluminum Chromate Conversion [Internet]. [cited 2020 Nov 15]. Available from: https://www.arrowcryogenics.com/chemical-processing/chromate-conversion-coating

163. Hagans PL. Chromate Conversion Coatings Characteristics of a Chromate Conversion Coating. 1994; Available from: www.asminternational.org

164. Gallaccio A, Pearlstein F, D'ambrosio MR. 4P EFFECTS OF HEATING CHROMATE CONVERSION COATINGS 4 by APR DEPARTMENT OF THE ARMY FRANKFORD ARSENAL Philadelphia, Pa. 19137. 1966.

165. Technologies HS. Technical Process Bulletin. 2010;(0980):1–5.

166. Castle JE, Ke R, Watts JF. Additional in-depth information obtainable from the energy loss features of photoelectron peaks: the oxidation and reduction of an Fe/Cr alloy in oxygen at low partial pressures and ultra high vacuum. Corrosion Science. 1990;30(8–9):771–98.

167. Grilli R, Baker MA, Castle JE, Dunn B, Watts JF. Corrosion behaviour of a 2219 aluminium alloy treated with a chromate conversion coating exposed to a 3.5% NaCl solution. Corrosion Science. 2011 Apr 1;53(4):1214–23.

168. NIST XPS Database, Selected Element Search Result [Internet]. [cited 2021 Jul 12]. Available from: https://srdata.nist.gov/xps/EngElmSrchQuery.aspx?EType=PE&CSOpt=Retri_ex_dat&Elm=Cr

169. Desimoni E, Malitesta C, Zambonin PG, Rivière JC. An x-ray photoelectron spectroscopic study of some chromium–oxygen systems. Surface and Interface Analysis. 1988;13(2–3):173–9.

170. Biesinger MC, Payne BP, Hart BR, Grosvenor AP, McIntryre NS, Wm Lau L, et al. Quantitative chemical state XPS analysis of first row transition metals, oxides and hydroxides. Journal of Physics: Conference Series. 2008 Mar 27;100(Part 1).

171. Brooks AR, Clayton CR, Doss K, Lu YC. On the Role of Cr in the Passivity of Stainless Steel. Journal of The Electrochemical Society. 1986 Dec 1;133(12):2459–64.

172. Maurice V, Yang WP, Marcus P. XPS and STM Investigation of the Passive Film Formed on Cr(110) Single-Crystal Surfaces. Journal of The Electrochemical Society. 1994 Nov 1;141(11):3016–27.

173. Halada GP, Clayton CR. Photoreduction of Hexavalent Chromium during X-Ray Photoelectron Spectroscopy Analysis of Electrochemical and Thermal Films. Journal of The Electrochemical Society. 1991 Oct 1;138(10):2921–7.

174. Biesinger MC, Payne BP, Grosvenor AP, Lau LWM, Gerson AR, Smart RSC. Resolving surface chemical states in XPS analysis of first row transition metals, oxides and hydroxides: Cr, Mn, Fe, Co and Ni. Applied Surface Science. 2011 Jan 15;257(7):2717–30.

175. Biesinger MC, Payne BP, Lau LWM, Gerson A, Smart RSC. X-ray photoelectron spectroscopic chemical state Quantification of mixed nickel metal, oxide and hydroxide systems. Surface and Interface Analysis. 2009 Apr;41(4):324–32.

176. Dabalà M, Brunelli K, Napolitani E, Magrini M. Cerium-based chemical conversion coating on AZ63 magnesium alloy. Surface & Coatings Technology [Internet]. 2003 Jul 29 [cited 2021 Sep 19];2–3(172):227–32. Available from: https://www.infona.pl//resource/bwmeta1.element.elsevier-cdea21b3-4583-382d-8736-1e70d57ca698

177. Oki M, Charles E. Chromate conversion coating on Al-0.2 wt.% Fe alloy. Materials Letters [Internet]. 2009;63(23):1990–1. Available from: http://dx.doi.org/10.1016/j.matlet.2009.06.033

178. Li X, Chen S, Yuan T, Jiang X, Han Y. Improving the properties of friction stir welded 2219-T87 aluminum alloy with GTA offset preheating. Journal of Manufacturing Processes. 2020;51.

179. Chromate Conversion Coatings on 2024 Al Alloy - Hughes - 1997 - Surface and Interface Analysis - Wiley Online Library [Internet]. [cited 2021 Sep 19]. Available from: https://analyticalsciencejournals.onlinelibrary.wiley.com/doi/abs/10.1002/(SICI)1096-9918(199704)25:4%3C223::AID-SIA225%3E3.0.CO;2-D

180. Juffs L, Hughes AE, Furman S, Paterson PJK. The use of macroscopic modelling of intermetallic phases in aluminium alloys in the study of ferricyanide accelerated chromate conversion coatings. Corrosion Science. 2002;44(8):1755–81.

VITA

MICHELLE STEPHANE PIERRE

2015-2020	Masters in Materials Science and Engineering Florida International University Department of Materials Science & Engineering Miami, Florida
2007-2012	Bachelor of Science in Chemistry (BS), Cum Laude Kennesaw State University Kennesaw, Georgia
2015-2015	LSAMP Bridge to Doctorate
2015-2018	NSF Graduate Research Fellowship
2018-2019	Florida Education Fund McKnight Doctoral Dissertation Fellow
2020-2021	NASA Kennedy Space Center Graduate Doctoral Dissertation Fellow
2015-present	Doctorate Candidate Florida International University Department of Materials Science & Engineering Miami, Florida

PUBLICATIONS AND PRESENTATIONS

E. Montgomery, M. Pierre, NASA KSC EGS Innovation, "Exposure and Evaluation of Corrosion Resistant Alloys at the Kennedy Space Center" Awarded 2020.

E. Montgomery, M. Pierre, NASA KSC EGS Innovation, "More Efficient Methods to Remove Prepare and Repair Coatings for GSE Structures" Awarded 2020.

E. Montgomery, M. Pierre, NASA KSC EGS Innovation, "Expanded Materials Options for High Strength Alloys on Ground Support Structures using COTS Coatings" Awarded 2019.

M. Pierre, S. Roychoudhury, Y. Umasankar, P. Manickam, N. Munroe, and S. Bhansali, "Textile Fiber Electrode to Monitor Uric Acid for Assessing Wound Chronicity" ECS Trans. 2017 volume 80, issue 10, 1277-1286.

S. Madhu, P. Manickam, M. Pierre, S. Bhansali, P. Nagamony and V. Chinnuswamy, "Nanostructured SnO_2 integrated conductive fabrics as binder-free electrode for neurotransmitter detection," Sensors and Actuators A: Physical, vol. 269, pp. 401-411, 2018.

P. Manickam, M. Pierre, R. Dev Jayant, M. Nair and S. Bhansali, "Future of Nanogels for Sensing Applications," in Nanogels for Biomedical Applications, The Royal Society of Chemistry, 2018, pp. 261-282.

Charting an Alternate Pathway to Reaction Orders and Rate Laws in Introductory Chemistry Courses. J. Chem. Educ. 2014, 91, 66-73.

232nd Electrochemical Society Meeting, National Harbor, MD "Textile Fiber Electrode to Monitor Uric Acid for Assessing Wound Chronicity" M. Pierre, S. Roychoudhury, Y. Umasankar, P. Manickam, N. Munroe, and S. Bhansali

ASSIST Conference, FIU, Miami, FL "Nanocomposite Textile Electrodes for Detecting Bio-analytes on a Wearable Platform" M. Pierre and S. Roychoudhury

ASSIST Conference, FIU, Miami, FL "Protective polymer coatings for cortisol immunoelectrochemical sensor" M. Pierre and T. Vokata.